Development of bioisostere-conjugated fluorescent probes for live-cell intracellular protein imaging

上川, 拓也

Doctoral thesis

Development of bioisostere-conjugated fluorescent probes for live-cell intracellular protein imaging

Takuya Kamikawa

Department of Chemistry

Graduate School of Science

Kyushu University

Table of contents

Chapter 1. General Introduction

1.1 introduction

1.1.1 Fluorescence protein imaging in living systems

Fluorescence imaging is a useful technique to visualize various biological events and environments in live cells and organisms through microscopic observation. This technique has the advantage of non-invasive monitoring with high spatial and temporal resolution.[1] Thus, fluorescence imaging has been performed for monitoring various environments[2-10] and the dynamics of biomolecules[11-22] and organelle analyses[23-31] in live cells.

Various proteins are known to exhibit diverse dynamics such as localization changes and degradations. In addition, various physiological functions, which are regulated by protein dynamics changes that have a key role in protein functions, are required to further elucidate. Therefore, the development of fluorescence protein imaging technique that enable spatial and temporal analysis of protein localization and function with real-time montoring in live cells is valuable for biological and pharmaceutical research area.[32-40]

1.1.2 Fluorescent protein labeling techniques using chemical reagents

Chemistry-based fluorescent labeling reagents, which are generally composed of fluorescent dyes and reactive moieties, have been applied for a wide range of medicinal chemistry and biological research areas.[41a] In the development of the reagents, the reactive moieties that react with nucleophilic natural amino acids have been employed. As a classical moiety, NHS (*N*-hydroxysuccinimide), an active ester, reacts with the amino group of lysine residues in aqueous solution. In addition, the thiol group of cysteine residues reacts with a Michael acceptor such as maleimide[41b] and α-halocarbonyl compounds (iodo, bromo, and chloro) to form a thioether, resulting in the alkylation of cysteine residues. Indeed, commercially available reagents such as 5-TAMRA (5-carboxytetramethylrhodamine) NHS and fluorescein-5-maleimide, which conjugate these reactants to fluorescent dyes, are widely used for fluorescent labeling of proteins in vitro systems. These electrophilic labeling techniques have also been extended to the preparation of antibody-drug conjugates (ADCs)[41c] and the bottom-up study of post-translational modification of proteins.[41d] However, their application in live cells is limited due to undesired side reactions with various endogenous nucleophiles.

In recent years, ligand-directed chemistry for protein labeling has also been developed.[42] This method allows for fluorescent labeling of the surface of protein of

interests (POIs) by using fluorescent probes with cleavable electrophiles in a traceless manner. Therefore, compared to methods that label the active site of POIs, the impact on the original functions of POIs is minimized. However, this method has the limitation that it can only be applied to label POIs that have known binding molecules or possess binding pockets.

1.1.3 Protein imaging technique using fluorescent proteins

As a biologically compatible approach, protein imaging using fluorescent proteins (FPs) has been actually used for the visualization of various POIs in live cells and in vivo systems.[43a-e] Using this method, it is possible to track the dynamics of POIs by fusing FPs to POIs and expressing them (POI-FPs) in live cells. However, there are certain properties that need to be considered when using FPs for live cell imaging. First, due to the large molecular size of FPs (approximately 27 kDa), fusion of FPs to POIs may affect the inherent behavior of the POI.[44] Second, a maturation reaction involving three amino acids (e.g., TYG for EGFP) in FPs is required to form the chromophore moiety from nascent FPs.[45] FPs with long maturation times limit the accuracy of temporal measurements for monitoring rapid processes such as gene expression dynamics (reporter gene assays) in live cells.

Third, various FPs, such as GFP F64L/S65T,[46a] EGFP,[46b] and pHluorin,[46c] exhibit a decrease in fluorescent intensity with lowering pH.[46d] This property is advantageous for developing pH biosensors. However, these FPs are challenging to use for protein imaging in acidic intracellular organelles because it is difficult to clearly distinguish whether changes in fluorescence signal intensity are due to the pH environment or protein amounts. Fourth, FPs generally do not show superior photophysical properties (photostability and brightness) compared to synthetic fluorescent dyes. In addition, most FPs are not suitable for pulse-chase type experiments because the fluorescence signals of FPs lack temporal information such as the time point of protein expression. Although FPs that work as

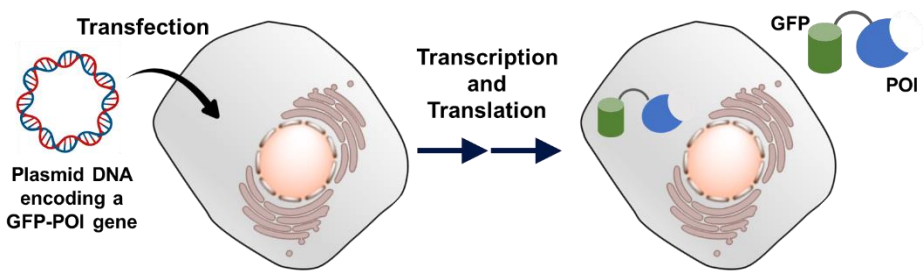

Figure 1-1. Schematic illustration of live-cell protein imaging using GFPs.

photo-induced “switchers” (photoconversion, photoactivation, photoswitching, and bleach-chase) can be applied for pulse-chase experiments,[47-49] these approaches are not generally convenient due to the requirement of a light irradiation unit. Therefore, an alternative technique that would overcome the limitations of imaging techniques using FPs is essential for live-cell protein imaging: namely, the development of imaging techniques that enable pulse-chase imaging are desirable.

1.1.4 Protein imaging technique using protein tags and synthetic fluorescent probes

A protein imaging technique using synthetic fluorescent probes that specifically react with protein tags (e.g., HaloTag,[50,51] SNAP-tag,[52] CLIP-tag,[53] TMP-tag,[54] FAST-tag,[55] BL-tag,[56] and PYP-tag[57]) is a useful approach for live-cell protein imaging. In this technique, synthetic fluorescent probes composed of fluorescent dyes and protein tag ligands are designed and synthesized. The protein tag is genetically encoded to fuse with POIs, and the fusion proteins can be expressed in live cells. Then, POIs can be observed by specifically labeling them with the probes in POI-expressing live cells. These methods have advantages in the availability of various fluorophores as protein-labeling probes and the ability to control the labeling time points. The latter advantage is suitable for pulse-chase labeling with this technique.[58,59] In addition, fluorogenic probes, which do not exhibit fluorescence in the free state but exhibit an increase of fluorescent intensity upon binding to POIs, have the advantage of being suitable for real-time imaging, because fluorogenic probes can rapidly image POIs with a high signal-to-background ratio without washing procedures. As non-fluorescent labeling reagents, functional molecules (e.g., biotin derivatives, click reagents, photocatalysts, and photo crosslinking reagents) can be conjugated with POIs using these labeling methods.[60]

PYP-tag system, a protein labeling technique using a photoactive yellow protein (PYP) as a protein tag, has been developed by author’s group. PYP-tag is a water-soluble protein derived from *Halorhodospira halophila* (a purple sulfur bacterium) with a molecular size of 14 kDa, which is smaller compared to fluorescent proteins (FPs).[61]

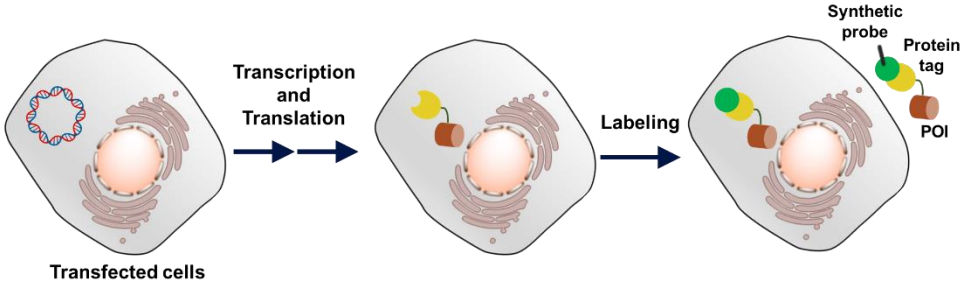

Figure 1-2. Schematic illustration of live-cell protein imaging using protein tag system.

Cys69 in PYP-tag specifically forms a covalent bond with synthetic molecule ligands such as *p*-coumaroyl thioester and coumarin thioester derivatives through transthioesterification. Compared to these ligands, an unnatural PYP-tag ligand, PCAF (PYP ligand with chloroacetamide and trifluoromethyl), has been reported to show high labeling efficiency and a rapid labeling reaction.[62] In addition to improving the performance of PYP-tag ligand, various PYP mutants have been created to improve the performance of PYP-tag. In particular, Gao et al. reported PYP mutant PYPNQN to improve the labeling kinetics of PYP-tag labeling probes bearing anionic groups.[63] In PYPNQN, three negative surface residues in PYPWT are replaced with neutral amino acids bearing amides in the side chain (namely D71N, E74Q, and D97N mutations). To date, this technique makes it possible to specifically visualize proteins of interest expressed in the cell membrane, cytosol, and nucleus within live cells. A significant advantage of this tag-based technique is the ability to introduce synthetic dyes with excellent photoproperties into proteins, compared to imaging techniques using FPs. In addition, the molecular size of PYP-tag is smaller (14 kDa) than that of the other protein tags (HaloTag: 33 kDa, SNAP-tag and CLIP-tag: 20 kDa, TMP-tag: 18 kDa, BL-tag: 27 kDa), and the impact on the perturbation of POIs such as their cellular localization would be less when fused with PYP-tag compared to the other protein tag.

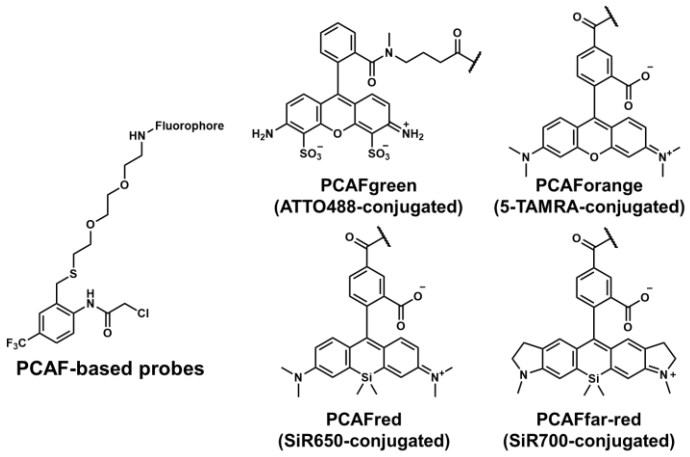

Figure 1-3. Previously reported PCAF-based probes.

1.1.5 Limitation of synthetic fluorescent probes with cationic dye scaffolds

Synthetic fluorescent probes with cationic dye scaffolds that show excellent photophysical properties and water solubility have been widely employed to develop mitochondria-targeting fluorescent probes in the bioimaging area.[1,23,64-69] For example, synthetic probes based on cationic scaffolds such as triphenylphosphonium, cyanine dye and rhodamine dye derivatives can stain mitochondria in live cells. Although these dyes, which exhibit high brightness, photostability, and water solubility, are useful tools for mitochondria imaging, their cellular toxicity remains problematic, particularly for long-term cell imaging.[23] In addition, the mitochondrial accumulation of cationic probes decreases the signal-to-background ratio for imaging non-mitochondrial proteins in live cells because accumulated probes in mitochondria caused serious artifacts due to non-specific fluorescent signals.

As discussed in the section of **1.1.4**, protein-labeled probes that exhibit high signal-to-background ratios are desirable for protein imaging. Therefore, it is essential to solve the mitochondrial accumulation for the development of protein labeling probes with cationic dyes that can be applied for non-mitochondrial protein imaging.

1.2 Outline of this research

In this thesis, membrane permeable protein-labeling probes that enable to visualize intracellular proteins without the organelle accumulation caused by the cationic nature of the dye scaffolds were successfully developed by introducing a hydrophobic bioisostere as an accumulation suppression group.

In Chapter 2, the synthesis, in vitro assays, and live-cell imaging experiments of novel protein-labeling probes are described. The author designed bioisostere-conjugated PYP-tag labeling probes bearing Rhodamine B derivatives (named RB) as a cationic dye scaffold, named **PCAF-RBis** (bioisostere-conjugated zwitterionic probes containing RB and PCAF ligand). To evaluate the effect of introducing the bioisostere on cellular behavior, a cationic RB-based probe without the bioisostere (**PCAF-RB**) was also synthesized. In addition, to develop a fluorogenic probe, Styrylpyridinium derivetives (named SP), which had been limited in its application in intracellular protein imaging, as a cationic dye scaffold were selected. Although a cationic SP-based probe (**PCAF-SP**) and a sulfonate-conjugated SP-based probe (**PCAF-SP-s**) were previously synthesized in author's group, these probes could not be applied for non-mitochondrial intracellular protein imaging. In this study, bioisostere-conjugated SP-based probe (**PCAF-SPis**) were developed. **PCAF-RBis** and **PCAF-SPis** could be used as membrane-permeable probes to visualize intracellular proteins without non-specific illumination, whereas **PCAF-RB** and **PCAF-SP** (cationic probes) showed non-specific illumination due to accumulation in the organelles. In particular, the SP-based probe images were obtained without a cell-washing step, indicating that **PCAF-SPis** works as a fluorogenic probe for the visualization of intracellular proteins.

In Chapter 3, the application of **PCAF-RBis** (an intracellular-protein-labeling probe) and **PCAF-SP-s** (a membrane-localized-protein-selectively-labeling probe) to live-cell glucose transporter 4 (GLUT4) imaging are described. The visualization of intracellular GLUT4 using **PCAF-RBis** without off-target labeling have been demonstrated by live-cell imaging and localization analyses using immunostaining. Membrane-localized GLUT4 can be specifically imaged without off-target labeling by live-cell imaging using **PCAF-SP-s** and localization analyses using both **PCAF-SP-s** labeling and immunostaining. Then, **PCAF-RBis** and **PCAF-SP-s** were applied to visualize multiple localizations of GLUT4.

In Chapter 4, the synthesis, fluorescence analyses, and live-cell imaging experiments of tetrazole-conjugated HaloTag labeling probes are described. The molecular design of tetrazole-conjugated probes was extended to the development of a HaloTag labeling

probe. The bioisostere-conjugated HaloTag labeling probe, **HTL-RBis**, composed of chloroalkane as a HaloTag ligand (HTL) and RB and a tetrazole, was synthesized. To evaluate the effect of introducing the bioisostere on cellular behavior, the cationic HaloTag labeling probe, **HTL-RB**, was also synthesized. As a result of live cell imaging, **HTL-RB** showed non-specific accumulation in the cytoplasm. In contrast, the fluorescent signal in the cytoplasm of the **HTL-RBis**-labeled cells was significantly reduced and the fluorescent signal in the corresponding to the localization of the HaloTag was observed.

In Chapter 5, the conclusions of this thesis and the future perspectives of a novel design strategy using a bioisostere for the development of zwitterionic molecular probes are described.

1.3 Reference

1. Lavis, L. D.; Raines, R. T. Bright Ideas for Chemical Biology. *ACS Chem. Biol.* **2008**, *3* (3), 142–155.
2. Maeda, H.; Kowada, T.; Kikuta, J.; Furuya, M.; Shirazaki, M.; Mizukami, S.; Ishii, M.; Kikuchi, K. Real-Time Intravital Imaging of pH Variation Associated with Osteoclast Activity. *Nat. Chem. Biol.* **2016**, *12* (8), 579–585.
3. Hashimoto, R.; Minoshima, M.; Kikuta, J.; Yari, S.; Bull, S. D.; Ishii, M.; Kikuchi, K. An Acid-Activatable Fluorescence Probe for Imaging Osteocytic Bone Resorption Activity in Deep Bone Cavities. *Angew. Chem. Int. Ed.* **2020**, *59* (47), 20996–21000.
4. Minoshima, M.; Umeno, T.; Kadooka, K.; Roux, M.; Yamada, N.; Kikuchi, K. Development of a Versatile Protein Labeling Tool for Live-Cell Imaging Using Fluorescent β-Lactamase Inhibitors. *Angew. Chem. Int. Ed.* **2023**, *62* (18), e202301704.
5. Takahashi, S.; Kagami, Y.; Hanaoka, K.; Terai, T.; Komatsu, T.; Ueno, T.; Uchiyama, M.; Koyama-Honda, I.; Mizushima, N.; Taguchi, T.; Arai, H.; Nagano, T.; Urano, Y. Development of a Series of Practical Fluorescent Chemical Tools To Measure pH Values in Living Samples. *J. Am. Chem. Soc.* **2018**, *140* (18), 5925–5933.
6. Shaner, N. C.; Steinbach, P. A.; Tsien, R. Y. A Guide to Choosing Fluorescent Proteins. *Nat. Methods* **2005**, *2* (12), 905–909.
7. Qin, X.; Yang, X.; Du, L.; Li, M. Polarity-Based Fluorescence Probes: Properties and Applications. *RSC Med. Chem.* **2021**, *12* (11), 1826–1838.
8. Danylchuk, D. I.; Jouard, P.-H.; Klymchenko, A. S. Targeted Solvatochromic Fluorescent Probes for Imaging Lipid Order in Organelles under Oxidative and Mechanical Stress. *J. Am. Chem. Soc.* **2021**, *143* (2), 912–924.
9. (a) Adachi, J.; Oda, H.; Fukushima, T.; Lestari, B.; Kimura, H.; Sugai, H.; Shiraki, K.; Hamaguchi, R.; Sato, K.; Kinbara, K. Dense and Acidic Organelle-Targeted Visualization in Living Cells: Application of Viscosity-Responsive Fluorescence Utilizing Restricted Access to Minimum Energy Conical Intersection. *Anal. Chem.* **2023**, *95* (12), 5196–5204. (b) Wang, L.; Xiao, Y.; Tian, W.; Deng, L. Activatable Rotor for Quantifying Lysosomal Viscosity in Living Cells. *J. Am. Chem. Soc.* **2013**, *135* (8), 2903–2906. (c) Wu, W.; Zhao, L.; Zhang, Y.; Wei, J.; Han, J.; Zhang, Y.; Zhao, Z. Golgi-Targeting Viscosity Probe for the Diagnosis of Alzheimer's Disease. *Sci Rep* **2024**, *14* (1), 1336. (d) Chen, W.; Gao, C.; Liu, X.; Liu, F.; Wang, F.; Tang, L.-J.; Jiang, J.-H. Engineering Organelle-Specific Molecular Viscosimeters Using

Aggregation-Induced Emission Luminogens for Live Cell Imaging. *Anal. Chem.* **2018**, *90* (15), 8736–8741.

10. Chuma, S.; Kiyosue, K.; Akiyama, T.; Kinoshita, M.; Shimazaki, Y.; Uchiyama, S.; Sotoma, S.; Okabe, K.; Harada, Y. Implication of Thermal Signaling in Neuronal Differentiation Revealed by Manipulation and Measurement of Intracellular Temperature. *Nat. Commun* **2024**, *15* (1), 3473.
11. Hirano, T.; Kikuchi, K.; Urano, Y.; Nagano, T. Improvement and Biological Applications of Fluorescent Probes for Zinc, ZnAFs. *J. Am. Chem. Soc.* **2002**, *124* (23), 6555–6562.
12. Hirayama, T.; Inden, M.; Tsuboi, H.; Niwa, M.; Uchida, Y.; Naka, Y.; Hozumi, I.; Nagasawa, H. A Golgi-Targeting Fluorescent Probe for Labile Fe (II) to Reveal an Abnormal Cellular Iron Distribution Induced by Dysfunction of VPS35. *Chem. Sci.* **2019**, *10* (5), 1514–1521.
13. Miyawaki, A.; Llopis, J.; Heim, R.; McCaffery, J. M.; Adams, J. A.; Ikura, M.; Tsien, R. Y. Fluorescent Indicators for Ca2+based on Green Fluorescent Proteins and Calmodulin. *Nature* **1997**, *388* (6645), 882–887.
14. Tour, O.; Adams, S. R.; Kerr, R. A.; Meijer, R. M.; Sejnowski, T. J.; Tsien, R. W.; Tsien, R. Y. Calcium Green FlAsH as a Genetically Targeted Small-Molecule Calcium Indicator. *Nat. Chem. Biol.* **2007**, *3* (7), 423–431.
15. Nakai, J.; Ohkura, M.; Imoto, K. A High Signal-to-Noise Ca2+ Probe Composed of a Single Green Fluorescent Protein. *Nat. Biotechnol* **2001**, *19* (2), 137–141.
16. Suzuki, J.; Kanemaru, K.; Ishii, K.; Ohkura, M.; Okubo, Y.; Iino, M. Imaging Intraorganellar Ca2+ at Subcellular Resolution Using CEPIA. *Nat. Commun* **2014**, *5* (1), 4153.
17. Wang, L.; Yuan, L.; Zeng, X.; Peng, J.; Ni, Y.; Er, J. C.; Xu, W.; Agrawalla, B. K.; Su, D.; Kim, B.; Chang, Y.-T. A Multisite-Binding Switchable Fluorescent Probe for Monitoring Mitochondrial ATP Level Fluctuation in Live Cells. *Angew. Chem. Int. Ed.***2016**, *55* (5), 1773–1776.
18. Nasu, Y.; Aggarwal, A.; Le, G. N. T.; Vo, C. T.; Kambe, Y.; Wang, X.; Beinlich, F. R. M.; Lee, A. B.; Ram, T. R.; Wang, F.; Gorzo, K. A.; Kamijo, Y.; Boisvert, M.; Nishinami, S.; Kawamura, G.; Ozawa, T.; Toda, H.; Gordon, G. R.; Ge, S.; Hirase, H.; Nedergaard, M.; Paquet, M.-E.; Drobizhev, M.; Podgorski, K.; Campbell, R. E. Lactate Biosensors for Spectrally and Spatially Multiplexed Fluorescence Imaging. *Nat. Commun* **2023**, *14* (1), 6598.

19. Yoshimura, H.; Inaguma, A.; Yamada, T.; Ozawa, T. Fluorescent Probes for Imaging Endogenous β-Actin mRNA in Living Cells Using Fluorescent Protein-Tagged Pumilio. *ACS Chem. Biol.* **2012**, *7* (6), 999–1005.
20. Ozawa, T.; Natori, Y.; Sato, M.; Umezawa, Y. Imaging Dynamics of Endogenous Mitochondrial RNA in Single Living Cells. *Nat. Methods* **2007**, *4* (5), 413–419.
21. Yamada, T.; Yoshimura, H.; Shimada, R.; Hattori, M.; Eguchi, M.; Fujiwara, T. K.; Kusumi, A.; Ozawa, T. Spatiotemporal Analysis with a Genetically Encoded Fluorescent RNA Probe Reveals TERRA Function around Telomeres. *Sci. Rep.* **2016**, *6* (1), 38910.
22. Simon, B.; Sandhu, M.; Myhr, K. L. Live FISH: Imaging mRNA in Living Neurons. *Journal of Neuroscience Research* **2010**, *88* (1), 55–63.
23. Xu, W.; Zeng, Z.; Jiang, J.-H.; Chang, Y.-T.; Yuan, L. Discerning the Chemistry in Individual Organelles with Small-Molecule Fluorescent Probes. *Angew. Chem. Int. Ed.* **2016**, *55* (44), 13658–13699.
24. Uno, K.; Sugimoto, N.; Sato, Y. N-Aryl Pyrido Cyanine Derivatives Are Nuclear and Organelle DNA Markers for Two-Photon and Super-Resolution Imaging. *Nat. Commun* **2021**, *12* (1), 2650.
25. Lukinavičius, G.; Blaukopf, C.; Pershagen, E.; Schena, A.; Reymond, L.; Derivery, E.; Gonzalez-Gaitan, M.; D'Este, E.; Hell, S. W.; Wolfram Gerlich, D.; Johnsson, K. SiR–Hoechst Is a Far-Red DNA Stain for Live-Cell Nanoscopy. *Nat. Commun* **2015**, *6* (1), 8497.
26. Wu, Z.; Tang, X. Visualizing Fluoride Ion in Mitochondria and Lysosome of Living Cells and in Living Mice with Positively Charged Ratiometric Probes. *Anal. Chem.* **2015**, *87* (17), 8613–8617.
27. Fujisawa, A.; Tamura, T.; Yasueda, Y.; Kuwata, K.; Hamachi, I. Chemical Profiling of the Endoplasmic Reticulum Proteome Using Designer Labeling Reagents. *J. Am. Chem. Soc.* **2018**, *140* (49), 17060–17070.
28. Hirayama, T.; Okuda, K.; Nagasawa, H. A Highly Selective Turn-on Fluorescent Probe for Iron(II) to Visualize Labile Iron in Living Cells. *Chem. Sci.* **2013**, *4* (3), 1250–1256.
29. Sawada, S.; Yoshikawa, M.; Tsutsui, K.; Miyazaki, T.; Kano, K.; Mishiro-Sato, E.; Tsukiji, S. Palmitoylation-Dependent Small-Molecule Fluorescent Probes for Live-Cell Golgi Imaging. *ACS Chem. Biol.* **2023**, *18* (5), 1047–1053.
30. Lukinavičius, G.; Reymond, L.; D'Este, E.; Masharina, A.; Göttfert, F.; Ta, H.; Güther, A.; Fournier, M.; Rizzo, S.; Waldmann, H.; Blaukopf, C.; Sommer, C.;

Gerlich, D. W.; Arndt, H.-D.; Hell, S. W.; Johnsson, K. Fluorogenic Probes for Live-Cell Imaging of the Cytoskeleton. *Nat. Methods* **2014**, *11* (7), 731–733.

31. Danylchuk, D. I.; Moon, S.; Xu, K.; Klymchenko, A. S. Switchable Solvatochromic Probes for Live-Cell Super-Resolution Imaging of Plasma Membrane Organization. *Angew. Chem. Int. Ed.* **2019**, *58* (42), 14920–14924.
32. Yamaguchi, T.; Asanuma, M.; Nakanishi, S.; Saito, Y.; Okazaki, M.; Dodo, K.; Sodeoka, M. Turn-ON Fluorescent Affinity Labeling Using a Small Bifunctional O-Nitrobenzoxadiazole Unit. *Chem. Sci.* **2014**, *5* (3), 1021–1029.
33. Fang, H.; Peng, B.; Ong, S. Y.; Wu, Q.; Li, L.; Yao, S. Q. Recent Advances in Activity-Based Probes (ABPs) and Affinity-Based Probes (AfBPs) for Profiling of Enzymes. *Chem. Sci.* **2021**, *12* (24), 8288–8310.
34. Yamaura, K.; Kiyonaka, S.; Numata, T.; Inoue, R.; Hamachi, I. Discovery of Allosteric Modulators for GABAA Receptors by Ligand-Directed Chemistry. *Nat Chem Biol* **2016**, *12* (10), 822–830.
35. Fujishima, S.; Yasui, R.; Miki, T.; Ojida, A.; Hamachi, I. Ligand-Directed Acyl Imidazole Chemistry for Labeling of Membrane-Bound Proteins on Live Cells. *J. Am. Chem. Soc.* **2012**, *134* (9), 3961–3964.
36. Kawano, M.; Murakawa, S.; Higashiguchi, K.; Matsuda, K.; Tamura, T.; Hamachi, I. Lysine-Reactive N-Acyl-N-Aryl Sulfonamide Warheads: Improved Reaction Properties and Application in the Covalent Inhibition of an Ibrutinib-Resistant BTK Mutant. *J. Am. Chem. Soc.* **2023**, *145* (48), 26202–26212.
37. Martineau, M.; Somasundaram, A.; Grimm, J. B.; Gruber, T. D.; Choquet, D.; Taraska, J. W.; Lavis, L. D.; Perrais, D. Semisynthetic Fluorescent pH Sensors for Imaging Exocytosis and Endocytosis. *Nat. Commun* **2017**, *8* (1), 1412.
38. Deo, C.; Abdelfattah, A. S.; Bhargava, H. K.; Berro, A. J.; Falco, N.; Farrants, H.; Moeyaert, B.; Chupanova, M.; Lavis, L. D.; Schreiter, E. R. The HaloTag as a General Scaffold for Far-Red Tunable Chemigenetic Indicators. *Nat. Chem. Biol.* **2021**, *17* (6), 718–723.
39. Zhu, W.; Takeuchi, S.; Imai, S.; Terada, T.; Ueda, T.; Nasu, Y.; Terai, T.; Campbell, R. E. Chemigenetic Indicators Based on Synthetic Chelators and Green Fluorescent Protein. *Nat. Chem. Biol.***2023**, *19* (1), 38–44.
40. Hori, Y.; Otomura, N.; Nishida, A.; Nishiura, M.; Umeno, M.; Suetake, I.; Kikuchi, K. Synthetic-Molecule/Protein Hybrid Probe with Fluorogenic Switch for Live-Cell Imaging of DNA Methylation. *J. Am. Chem. Soc.* **2018**, *140* (5), 1686–1690.
41. (a) Sakamoto, S.; Hamachi, I. Recent Progress in Chemical Modification of Proteins. *ANAL. SCI.* **2019**, *35* (1), 5–27. (b) Moore, J. E.; Ward, W. H. Cross-Linking of

Bovine Plasma Albumin and Wool Keratin. *J. Am. Chem. Soc.* **1956**, *78* (11), 2414–2418. (c) Liu, K.; Li, M.; Li, Y.; Li, Y.; Chen, Z.; Tang, Y.; Yang, M.; Deng, G.; Liu, H. A Review of the Clinical Efficacy of FDA-Approved Antibody–drug Conjugates in Human Cancers. *Mol Cancer* **2024**, *23* (1), 62.

42. Sakamoto, S.; Hamachi, I. Ligand-Directed Chemistry for Protein Labeling for Affinity-Based Protein Analysis. *Israel Journal of Chemistry* **2023**, *63* (3–4), e202200077.
43. (a) Ormö, M.; Cubitt, A. B.; Kallio, K.; Gross, L. A.; Tsien, R. Y.; Remington, S. J. Crystal Structure of the *Aequorea Victoria* Green Fluorescent Protein. *Science* **1996**, *273* (5280), 1392–1395. (b) Chalfie, M,; Tu, Y., Euskirchen, G.,; Ward, W. W.,; Prasherf, C. D., Green Fluorescent Protein as a Marker for Gene Expression. *Science* **1994**, *263* (5148), 802–805. (c) Adams, S. R.; Campbell, R. E.; Gross, L. A.; Martin, B. R.; Walkup, G. K.; Yao, Y.; Llopis, J.; Tsien, R. Y. New Biarsenical Ligands and Tetracysteine Motifs for Protein Labeling in Vitro and in Vivo: Synthesis and Biological Applications. *J. Am. Chem. Soc.* **2002**, *124* (21), 6063–6076. (d) Ando, R.; Shimozono, S.; Ago, H.; Takagi, M.; Sugiyama, M.; Kurokawa, H.; Hirano, M.; Niino, Y.; Ueno, G.; Ishidate, F.; Fujiwara, T.; Okada, Y.; Yamamoto, M.; Miyawaki, A. StayGold Variants for Molecular Fusion and Membrane-Targeting Applications. *Nat. Methods* **2024**, *21* (4), 648–656. (e) Ando, R.; Shimozono, S.; Ago, H.; Takagi, M.; Sugiyama, M.; Kurokawa, H.; Hirano, M.; Niino, Y.; Ueno, G.; Ishidate, F.; Fujiwara, T.; Okada, Y.; Yamamoto, M.; Miyawaki, A. StayGold Variants for Molecular Fusion and Membrane-Targeting Applications. *Nat. Methods* **2024**, *21* (4), 648–656.
44. Shaner, N. C.; Steinbach, P. A.; Tsien, R. Y. A Guide to Choosing Fluorescent Proteins. *Nat. Methods* **2005**, *2* (12), 905–909.
45. Balleza, E.; Kim, J. M.; Cluzel, P. Systematic Characterization of Maturation Time of Fluorescent Proteins in Living Cells. *Nat. Methods* **2018**, *15* (1), 47–51.
46. (a) Kneen, M.; Farinas, J.; Li, Y.; Verkman, A. S. Green Fluorescent Protein as a Noninvasive Intracellular pH Indicator. *Biophysical Journal* **1998**, *74* (3), 1591–1599. (b) Minoshima, M.; Umeno, T.; Kadooka, K.; Roux, M.; Yamada, N.; Kikuchi, K. Development of a Versatile Protein Labeling Tool for Live-Cell Imaging Using Fluorescent β-Lactamase Inhibitors. *Angew. Chem. Int. Ed.* **2023**, *62* (18), e202301704. (c) Miesenböck, G.; De Angelis, D. A.; Rothman, J. E. Visualizing Secretion and Synaptic Transmission with pH-Sensitive Green Fluorescent Proteins. *Nature* **1998**, *394* (6689), 192–195. (d) Crivat, G.; Taraska, J. W. Imaging Proteins inside Cells with Fluorescent Tags. *Trends in Biotechnology* **2012**, *30*, 8–16.

47. Fuchs, J.; Böhme, S.; Oswald, F.; Hedde, P. N.; Krause, M.; Wiedenmann, J.; Nienhaus, G. U. A Photoactivatable Marker Protein for Pulse-Chase Imaging with Superresolution. *Nat. Methods* **2010**, *7* (8), 627–630.
48. Lukyanov, K. A.; Chudakov, D. M.; Lukyanov, S.; Verkhusha, V. V. Photoactivatable Fluorescent Proteins. *Nat. Rev. Mol. Cell Biol.* **2005**, *6* (11), 885–890.
49. Knop, M.; Edgar, B. A. Tracking Protein Turnover and Degradation by Microscopy: Photo-Switchable versus Time-Encoded Fluorescent Proteins. *Open Biol.* **2014**, *4* (4), 140002.
50. Los, G. V.; Encell, L. P.; McDougall, M. G.; Hartzell, D. D.; Karassina, N.; Zimprich, C.; Wood, M. G.; Learish, R.; Ohana, R. F.; Urh, M.; Simpson, D.; Mendez, J.; Zimmerman, K.; Otto, P.; Vidugiris, G.; Zhu, J.; Darzins, A.; Klaubert, D. H.; Bulleit, R. F.; Wood, K. V. HaloTag: A Novel Protein Labeling Technology for Cell Imaging and Protein Analysis. *ACS Chem. Biol.* **2008**, *3* (6), 373–382.
51. Kompa, J.; Bruins, J.; Glogger, M.; Wilhelm, J.; Frei, M. S.; Tarnawski, M.; D'Este, E.; Heilemann, M.; Hiblot, J.; Johnsson, K. Exchangeable HaloTag Ligands for Super-Resolution Fluorescence Microscopy. *J. Am. Chem. Soc.* **2023**, *145* (5), 3075–3083.
52. Keppler, A.; Gendreizig, S.; Gronemeyer, T.; Pick, H.; Vogel, H.; Johnsson, K. A General Method for the Covalent Labeling of Fusion Proteins with Small Molecules in Vivo. *Nat Biotechnol* **2003**, *21* (1), 86–89.
53. Gautier, A.; Juillerat, A.; Heinis, C.; Corrêa, I. R.; Kindermann, M.; Beaufils, F.; Johnsson, K. An Engineered Protein Tag for Multiprotein Labeling in Living Cells. *Chemistry & Biology* **2008**, *15* (2), 128–136.
54. Jing, C.; Cornish, V. W. A Fluorogenic TMP-Tag for High Signal-to-Background Intracellular Live Cell Imaging. *ACS Chem. Biol.* **2013**, *8* (8), 1704–1712.
55. Gautier, A. Fluorescence-Activating and Absorption-Shifting Tags for Advanced Imaging and Biosensing. *Acc. Chem. Res.* **2022**, *55* (21), 3125–3135.
56. Mizukami, S.; Watanabe, S.; Hori, Y.; Kikuchi, K. Covalent Protein Labeling Based on Noncatalytic β-Lactamase and a Designed FRET Substrate. *J. Am. Chem. Soc.* **2009**, *131* (14), 5016–5017.
57. Hori, Y.; Kikuchi, K. Protein Labeling with Fluorogenic Probes for No-Wash Live-Cell Imaging of Proteins. *Current Opinion in Chemical Biology* **2013**, *17* (4), 644–650.

58. Yoshimura, A.; Mizukami, S.; Hori, Y.; Watanabe, S.; Kikuchi, K. Cell-Surface Protein Labeling with Luminescent Nanoparticles through Biotinylation by Using Mutant β-Lactamase-Tag Technology. *ChemBioChem* **2011**, *12* (7), 1031–1034.
59. Mizukami, S.; Watanabe, S.; Akimoto, Y.; Kikuchi, K. No-Wash Protein Labeling with Designed Fluorogenic Probes and Application to Real-Time Pulse-Chase Analysis. *J. Am. Chem. Soc.* **2012**, *134* (3), 1623–1629.
60. Wilhelm, J.; Kühn, S.; Tarnawski, M.; Gotthard, G.; Tünnermann, J.; Tänzer, T.; Karpenko, J.; Mertes, N.; Xue, L.; Uhrig, U.; Reinstein, J.; Hiblot, J.; Johnsson, K. Kinetic and Structural Characterization of the Self-Labeling Protein Tags HaloTag7, SNAP-Tag, and CLIP-Tag. *Biochemistry* **2021**, *60* (33), 2560–2575.
61. Kroon, A. R.; Hoff, W. D.; Fennema, HermanP. M.; Gijzen, J.; Koomen, G.-J.; Verhoeven, J. W.; Crielaard, W.; Hellingwerf, K. J. Spectral Tuning, Fluorescence, and Photoactivity in Hybrids of Photoactive Yellow Protein, Reconstituted with Native or Modified Chromophores. *J. Biol. Chem.* **1996**, *271* (50), 31949–31956.
62. Nishiura, M.; Hori, Y.; Umeno, M.; Kikuchi, K. Visualization of Multiple Localizations of GLUT4 by Fluorescent Probes of PYP-Tag with Designed Unnatural Warhead. *Chem. Sci.* **2023**, *14* (22), 5925–5935.
63. Gao, J.; Hori, Y.; Nishiura, M.; Bordy, M.; Hasserodt, J.; Kikuchi, K. Engineered Protein-Tag for Rapid Live-Cell Fluorogenic Visualization of Proteins by Anionic Probes. *Chem. Lett.* **2020**, *49* (3), 232–235.
64. Dempsey, G. T.; Vaughan, J. C.; Chen, K. H.; Bates, M.; Zhuang, X. Evaluation of Fluorophores for Optimal Performance in Localization-Based Super-Resolution Imaging. *Nat. Methods* **2011**, *8* (12), 1027–1036.
65. Heilemann, M.; van de Linde, S.; Mukherjee, A.; Sauer, M. Super-Resolution Imaging with Small Organic Fluorophores. *Angew. Chem. Int. Ed.* **2009**, *48* (37), 6903–6908.
66. Wang, L.; Du, W.; Hu, Z.; Uvdal, K.; Li, L.; Huang, W. Hybrid Rhodamine Fluorophores in the Visible/NIR Region for Biological Imaging. *Angew. Chem. Int. Ed.* **2019**, *58* (40), 14026–14043.
67. Clark, S. A.; Singh, V.; Vega Mendoza, D.; Margolin, W.; Kool, E. T. Light-Up "Channel Dyes" for Haloalkane-Based Protein Labeling in Vitro and in Bacterial Cells. *Bioconjugate Chem.* **2016**, *27* (12), 2839–2843.
68. Miró-Vinyals, C.; Stein, A.; Fischer, S.; Ward, T. R.; Deliz Liang, A. HaloTag Engineering for Enhanced Fluorogenicity and Kinetics with a Styrylpyridium Dye. *ChemBioChem* **2021**, *22* (24), 3398–3401.

69. Yang, Q.; Wang, S.; Li, D.; Yuan, J.; Xu, J.; Shao, S. A Mitochondria-Targeting Nitroreductase Fluorescent Probe with Large Stokes Shift and Long-Wavelength Emission for Imaging Hypoxic Status in Tumor Cells. *Analytica Chimica Acta* **2020**, *1103*, 202–211.

Chapter 2. Bioisostere-conjugated fluorescent probes for live-cell protein imaging without non-specific organelle accumulation

2.1 Introduction

Cationic fluorescent dyes that show excellent photoproperties (e.g., high fluorescence quantum yield and photobleaching resistance) and water solubility are highly useful sources for developing fluorescent probes.[1-8] Various fluorescent probes based on cationic dyes (e.g., rhodamine, cyanine, and pyridinium dye scaffolds) can be applied for bioimaging studies (Figure 2-1). Additionally, some biocompatible cationic probe precursors are commercially available at reasonable prices (e.g., rhodamine B, rhodamine 19, and rhodamine 640), and probes based on these derivatives can be prepared by concise conjugation steps.[9] Cationic dyes can be easily taken up by mitochondria owing to the high negative potential of the inner membrane. This accumulation property of cationic dyes enables the development of various mitochondria-targeting probes while causing serious artifacts in live-cell non-mitochondrial protein imaging owing to non-specific fluorescent signals from the mitochondria. This behavior limits the application of cationic fluorescent probes using protein tag systems (Figure 2-2).

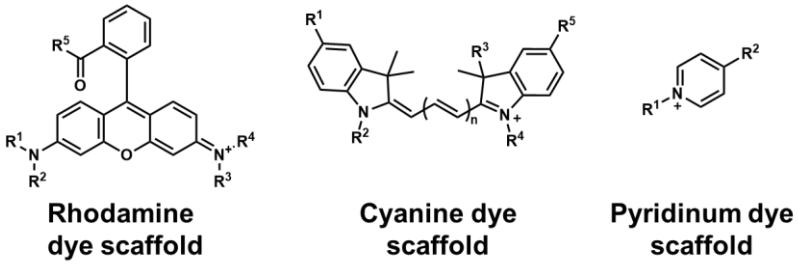

Figure 2-1. Biocompatible cationic dye scaffolds showing mitochondria accumulation.

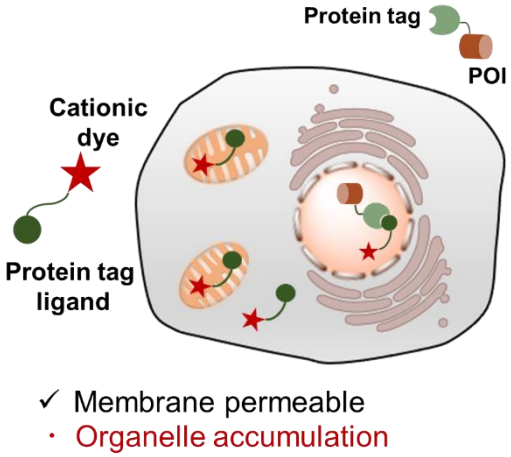

Figure 2-2. Schematic illustration of previously reported strategy for intracellular protein imaging using various cationic scaffolds and protein tag labeling system. Cationic probes for protein imaging are cell permeable but show organelle accumulation.

Introducing anionic groups such as carboxyl and sulfonyl groups into cationic probes, an approach that brings the net charge of the cationic probes to zero (namely zwitterionic probes), is anticipated to suppress undesired mitochondrial accumulation. Additionally, zwitterionic fluorescent probes also have the advantage of bioavailability due to their good water solubility. Sulfonated zwitterionic probes using cationic dye scaffolds (e.g., cyanine or pyridinium dye scaffolds) are useful in biological samples and in vivo systems.[10-13] However, the approach of introducing anionic groups, such as carboxylate, sulfonate, and phosphonate groups, into the probes significantly reduces or loses the membrane permeability of the probes. Commercially available probes such as ATTO and sulfonated cyanine dyes are known to lose membrane permeability.[14-22] In terms of protein labeling probes, several sulfonated zwitterionic probes have been developed for visualizing POIs tagged with protein tags, which are localized on the cell surface. In the case of HaloTag systems, various sulfonated HaloTag labeling probes (CA-sulfo549, CA-sulfo646, Halo rhodamine-4, and Halo SiR-5) have been reported to be used in imaging experiments to visualize cell surface-localized POIs.[14,15] In particular, Halo rhodamine-4 and Halo SiR-5 exhibited good fluorogenicity, allowing for membrane protein imaging without the need for the washing steps to remove excess free probes. In other systems, BG-Sulfo549, SBG-TMR, DRBG-488, and SNAP rhodamine-3 are sulfonated

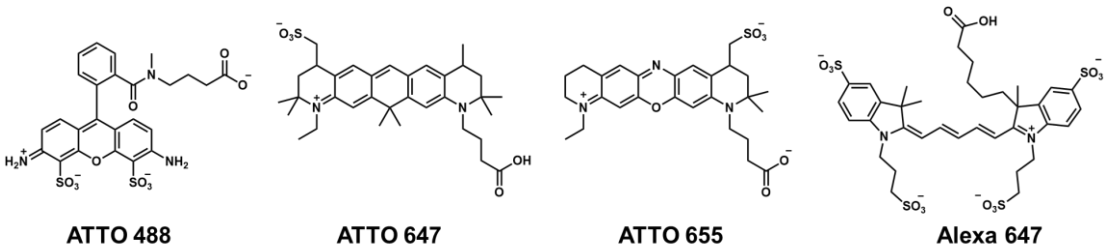

Figure 2-3. Commercially available sulfonated dyes.

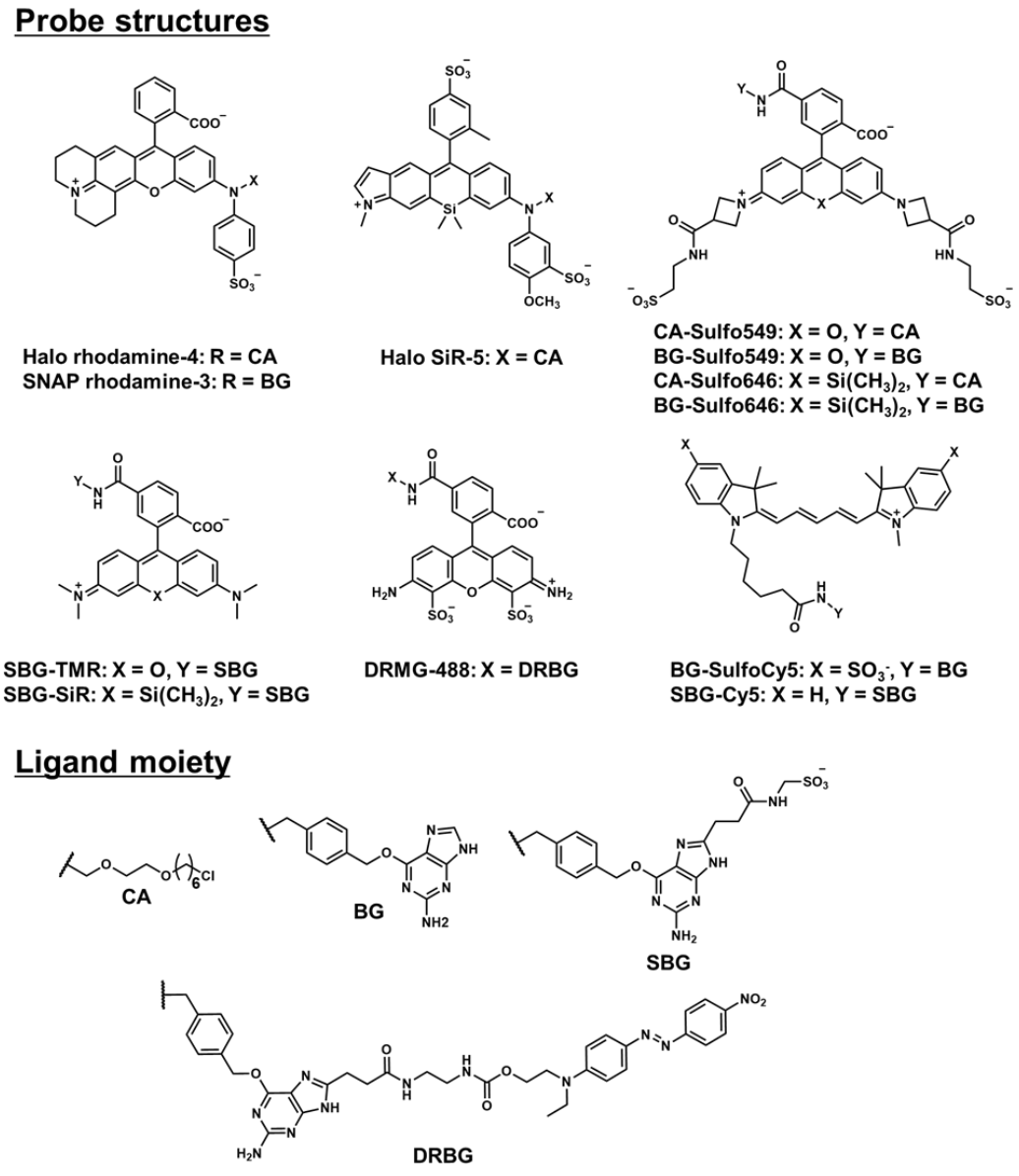

Figure 2-4. Sulfonate-conjugated protein-tag labeling probes.

zwitterionic probes and can visualize cell surface-localized POIs.[14-17] In PYP-tag systems, Cy3DNB2, Cy5DNB2, ATDNB2, and PCAFgreen have sulfonated fluorescent dye scaffolds, specifically sulfo-cyanine3, sulfo-cyanine5, ATTO 655, and ATTO 488, respectively.[18-20] These are cell membrane-impermeant probes that can selectively label cell surface-localized POIs tagged with PYP-tag, while they do not label intracellular POIs. Although these sulfonated probes are useful tools for live-cell protein imaging, they cannot be applied for live-cell intracellular protein imaging.

To maintain permeability, there have been reports of developing membrane-permeable cationic pro-probes (e.g., Rhod-2 acetoxymethyl (AM) and RhodZin-3 AM) with AM esters as precursors of carboxylic acids.[23,24] These pro-probes penetrate the cell membrane, and the AM ester is hydrolyzed by endogenous esterases in live cells to form carboxylic acids.[23-28] However, Rhod-2 AM and RhodZin-3 AM still exhibit mitochondrial accumulation owing to their cationic and highly lipophilic fluorescent scaffolds.[23-25]

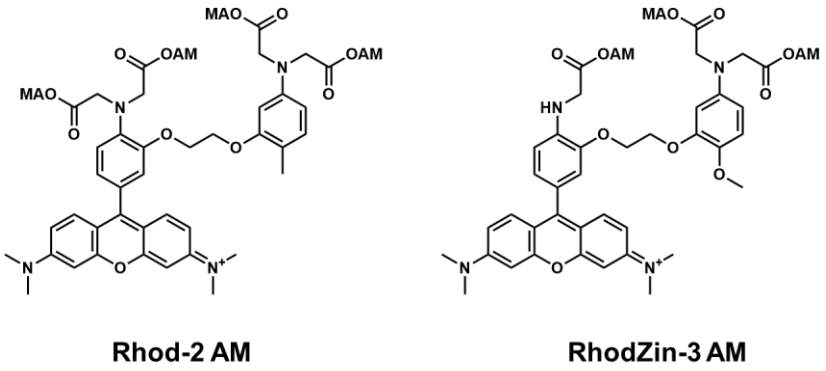

Figure 2-5. Cationic pro-probes with precursors of the anionic group.

A few zwitterionic membrane-permeable probes without dye scaffold modifications, namely rhodamine dye scaffolds conjugated with sulfonate through an alkyl chain, termed OregonFluor (ORFluor), enable the visualization of intracellular proteins.[29] Although these probes do not show undesired accumulation in organelles, this method has several limitations. First, these probes are "always-on probes" that show fluorescence in both free and bound states, resulting in background signals from excess free probes. Therefore, multiple time-consuming washing steps are required to reduce these background signals in live-cell protein imaging. In contrast, fluorogenic probes, also known as OFF–ON type probes, exhibit increased fluorescent intensity upon binding to their targets, known as

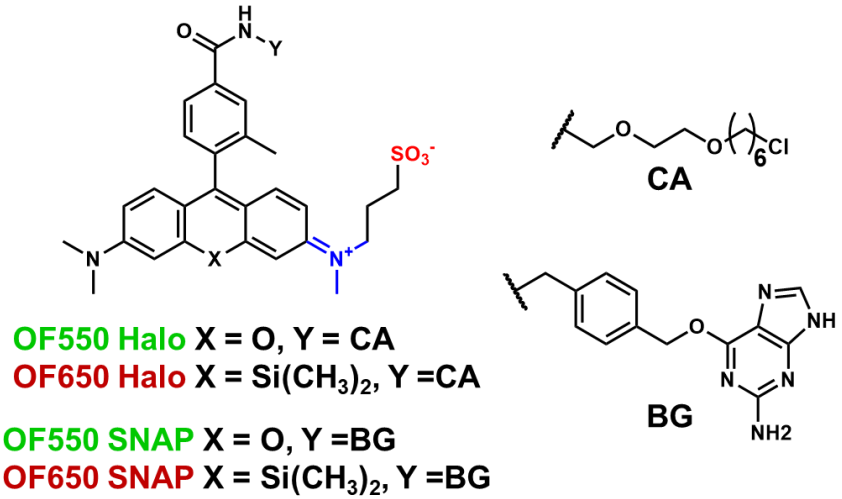

Figure 2-6. Membrane-permeable sulfonate-conjugated probes.

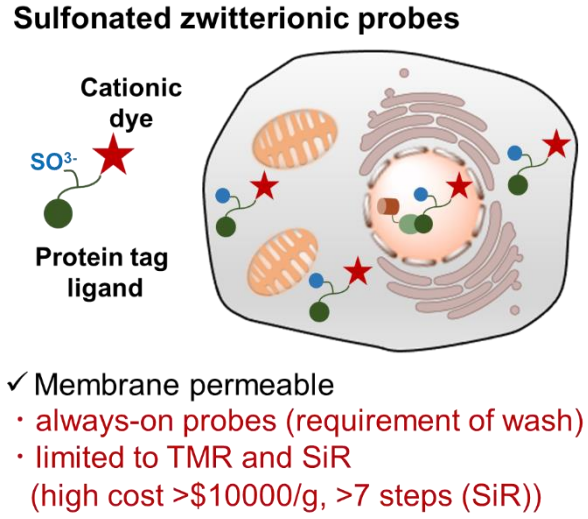

Figure 2-7. Schematic illustration of previously reported strategy for intracellular protein imaging using various cationic scaffolds and protein tag labeling system. Limited numbers of membrane-permeable sulfonated zwitterionic probes do not show undesired organelle accumulations but this approach is limited to OregonFluor (ORFluor) based-probes that are always-on probes based on TMR and SiR.

fluorogenicity.[30-34] In live-cell imaging using fluorogenic probes, washing steps are not required owing to the low background of free probes. Thus, fluorogenicity is desirable for real-time imaging of POIs in live cells (Figure 2-8). Second, membrane-permeable protein labeling probes with sulfonate groups have been limited to reports on tetramethylrhodamine (TMR) and siliconrhodamine (SiR).[35] Although these scaffolds

show favorable optical properties, the synthesis of novel probes using these derivatives suffers from their extremely high cost (typically >$10,000/g).[9] The synthesis of SiR scaffolds requires more than seven steps from commercial sources. Thus, a novel design strategy is required to advance the development of fluorogenic protein-labeling probes with cationic dye scaffolds that are synthetically accessible, membrane permeable, and diffusible without nonspecific accumulation in the mitochondria.

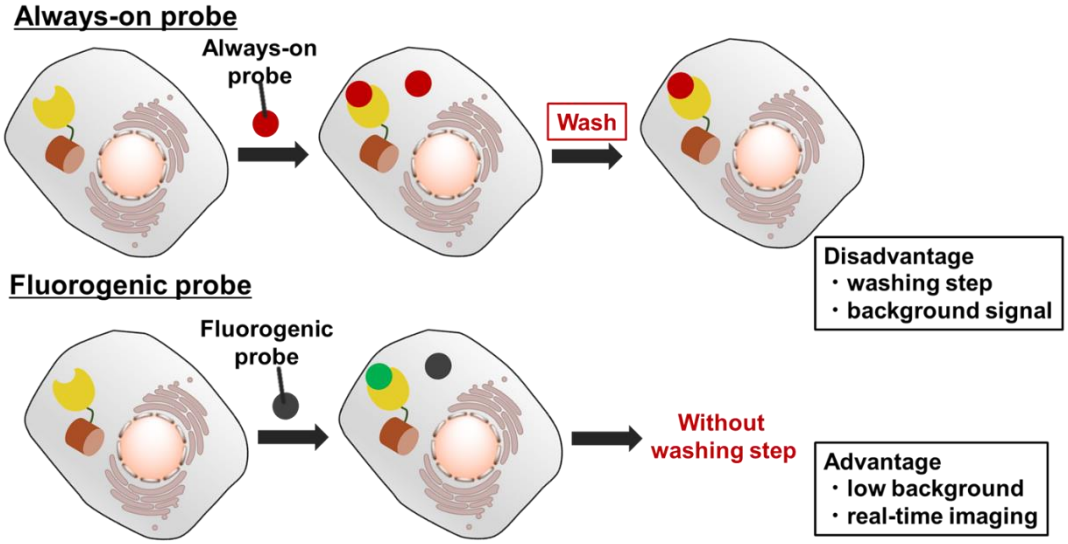

Figure 2-8. Advantages of fluorogenic probe in fluorescence imaging.

In this study, probes with these properties were developed using a design strategy to overcome the above-mentioned limitations. The author considered that the significant decrease in membrane permeability was caused by introducing hydrophilic anionic groups, such as carboxylic or sulfonate groups. Based on this idea, anionic groups with higher hydrophobicity would be preferable for protein labeling probes with cationic dye

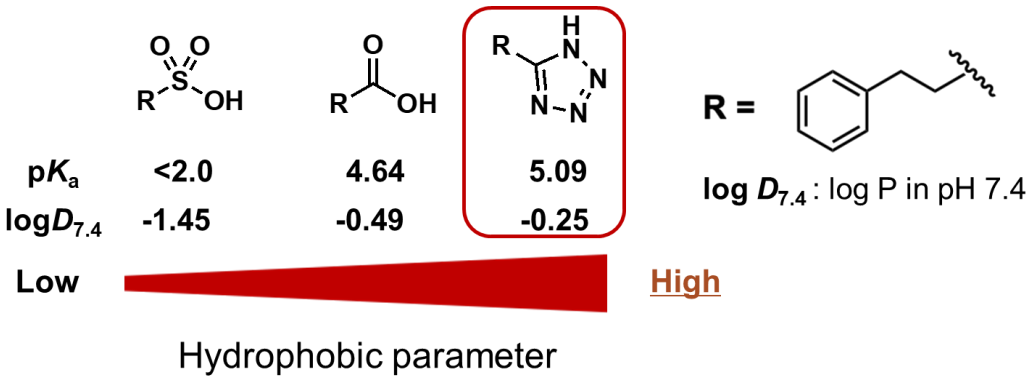

Figure 2-9. Chemical properties on bioisosteres of carboxylic acid.

scaffolds. Thus, bioisosteres of carboxylic acids was focused as a pool of anionic groups to select the introducing group.

In 1951, Friedman proposed the definition of "bioisostere" by expanding the definition of "isostere." Bioisosteres are groups of compounds with chemical and physical similarities, and similar or antagonistic biological properties. Furthermore, the concept of bioisosterism, which was extended by Thornber in 1979, considers various parameters of the groups such as molecular size and shape, electronic distribution, hydrophobicity and hydrophilicity, metabolism, and H-bonding patterns.[36] In recent years, bioisosteres have been widely employed in medicinal chemistry, where bioisosteric replacements are conducted in bioactive compounds. Bioisosteric replacements enable the tuning of chemical and physical properties by mimicking functional groups. This approach has also been employed in structure–activity relationship studies to increase biological activity, selectivity, and biocompatibility. In particular, hydrophobic bioisosteres as mimics of anionic groups can be applied to improve membrane permeability in several bioactive compounds.[37] Hydrophobic bioisosteres of carboxylic acids can be applied to improve membrane permeability in several bioactive compounds.[38] However, a design strategy using hydrophobic mimics to improve membrane permeability in fluorescent probes remains to be reported.[39] The author believes that the strategy using hydrophobic mimics of anionic groups holds promise for developing intracellular protein labeling probes. Based on this discussion, a tetrazole ring, a bioisostere of carboxylic acid, was selected as a hydrophobic mimic to provide sufficient hydrophobicity.

In this chapter, protein labeling probes containing cationic dye scaffolds, rhodamine B tertiary amides and styryl pyridinium derivatives, was successfully developed for live-cell intracellular protein imaging without undesired mitochondrial accumulation by conjugating a tetrazole (Figure 2-10). All the tetrazole-conjugated probes were easily synthesized through concise conjugation using a tetrazole-bearing amino acid derivative without modifying the dye scaffolds. In particular, tetrazole-conjugated SP-based probes exhibit excellent fluorogenicity (94-fold) upon binding to protein tags in vitro and enable non-wash imaging of intracellular proteins in live cells. Additionally, a tetrazole-bearing amino acid derivative can be synthesized in one step from a commercial source. In the preparation of RB and SP, these derivatives (pre-conjugation) can be prepared in three steps from commercial sources, and these sources are available at a reasonable price (<**$**2/g).[6,9] The author expects that this probe design will not only provide a versatile strategy for intracellular protein imaging using protein-tag systems but also open up new possibilities in membrane-permeable molecular probes.

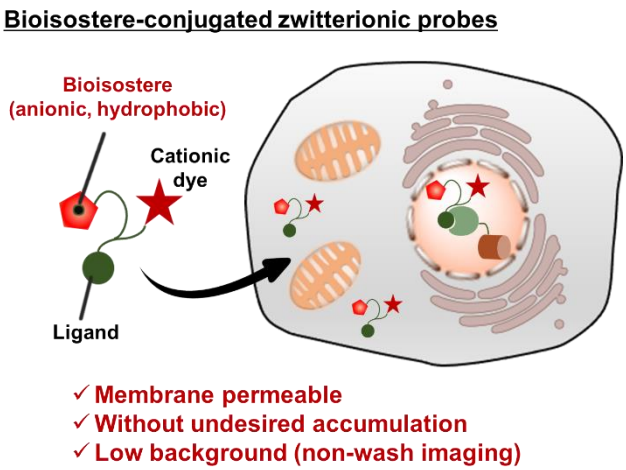

Figure 2-10. Schematic illustration of probe design strategy for intracellular protein imaging using various cationic scaffolds and protein tag labeling system. Zwitterionic probes with tetrazole as an organelle accumulation suppression group show cell permeability and low background. POI denotes protein of interest.

2.2. Result and discussion

2.2.1 Molecular design of membrane-permeable PYP-tag labeling probes

To examine the effect of tetrazole introduction on the intracellular behavior of the probes in both free and bound states, the author considered that the design of an always-on probe based on a cationic dye scaffold, which emits fluorescence under physiological conditions, is required. RB exhibits strong fluorescence under physiological conditions and is widely used in fluorescence imaging studies owing to its sufficient water solubility.[9] The author designed two RB-based probes, **PCAF-RB** and **PCAF-RBis**, using either a PEG5 linker or a tetrazole-conjugated PEG linker to connect RB (the fluorophore) with the PCAF ligand (Figure 2-11.). **PCAF-RB** is a cationic probe (net charge: +1) owing to the nature of RB, while **PCAF-RBis** is a zwitterionic probe (net charge: 0 under physiological conditions) achieved by introducing a tetrazole into the probe.

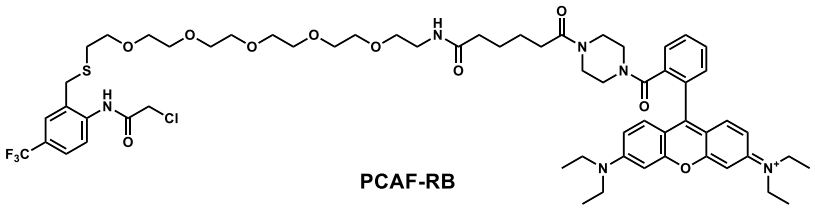

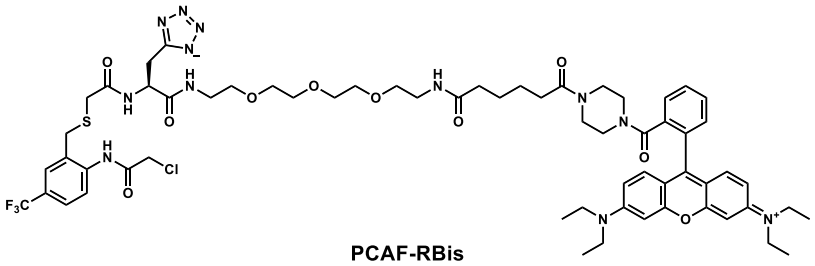

Figure 2-11. PCAF-RB and **PCAF-RBis**.

Next, bioisostere-conjugated fluorogenic probes were designed to enable non-wash imaging of intracellular proteins without undesired accumulation. SP is a cationic dye scaffold with bioavailability that emits weak fluorescence under physiological conditions owing to the twisted intramolecular charge transfer (TICT) process.[40-43] TICT is an electron transfer process, which occurs upon photoexcitation in molecules that are generally composed of electron donor and acceptor moieties linked by covalent bonds involving twisted single bonds. In SP, twisting of rotatable bonds between the diethyl amino group (donor) and the quaternized pyridine (acceptor) occurs in the TICT state of SP. After the formation of the TICT state, SP mainly processes non-radiative decay,

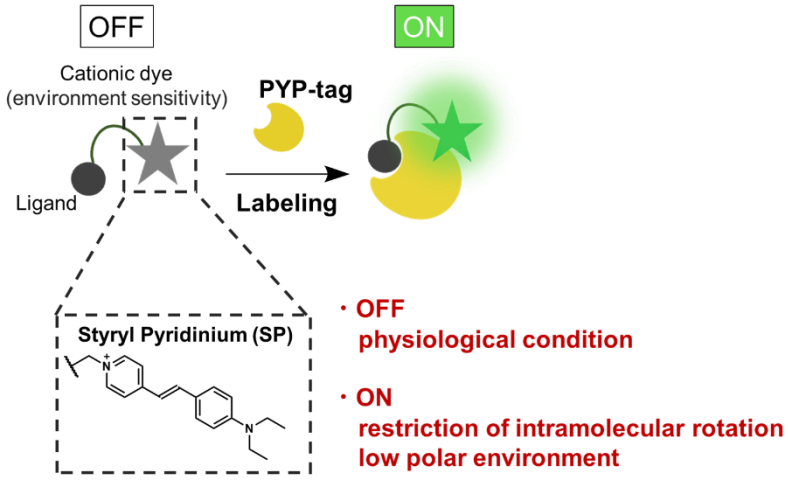

Figure 2-12. Schematic illustration of OFF-ON mechanism in SP-based fluorogenic probe.

resulting in suppressed fluorescence emission. In contrast, SP emits strong fluorescence in a low-polar environment or by the restriction of intramolecular rotation in the rotatable bonds of SP. In terms of SP application in protein tag labeling probes, the HaloTag labeling probe F1 is composed of SP directly connected to a HaloTag ligand moiety and has been reported to show a 27-fold increase in fluorescent intensity upon binding to HaloTag protein.[6] However, the use of F1 in live-cell imaging results in several problems, such as mitochondrial accumulation caused by the net charge of the probe and the need for a washing process.

Focusing on its properties, SP as a cationic dye scaffold was employed to develop a fluorogenic probe. The author's group previously developed SP-based probes, **PCAF-SP** and **PCAF-SP-s**, using either a PEG5 linker or a sulfonate-conjugated PEG linker to connect SP with PCAF. **PCAF-SP** is a membrane-permeable cationic probe that exhibits fluorogenicity in vitro. However, **PCAF-SP** shows undesired accumulation in the cytoplasmic region, which limits its application in intracellular protein imaging to mitochondria-localized protein imaging. **PCAF-SP-s** is a sulfonate-conjugated zwitterionic probe that exhibits significantly poor membrane permeability owing to the introduction of the sulfonate group. Although **PCAF-SP-s** is a useful tool for labeling PYP-tag proteins localized on the cell surface, it cannot be applied for intracellular protein imaging in live cells.

To solve these problems, the author considered that a new probe design based on tetrazole could be applied for the development of a membrane-permeable SP-based probe without undesired accumulation. Specifically, the replacement of the sulfonate group with

a tetrazole in **PCAF-SP-s** effectively increased the probe's membrane permeability. Following this discussion, the author designed the tetrazole-conjugated SP-based probe **PCAF-SPis** using a tetrazole-conjugated PEG linker to connect SP with PCAF.

Then, the clog *P* (calculated log *P*) of zwitterionic probes (tetrazole-, carboxylate-, or sulfonate-conjugated probes) was calculated to estimate the effect of anionic group introduction on the membrane permeability of these probes because the log P value generally correlates with membrane permeability. As shown in Table 2-1, the clog P values of tetrazole-conjugated probes are higher than those of carboxylate- or sulfonate-conjugated probes, which is consistent with the clog P correlation of bioisosteres of carboxylic acids. The results suggest that tetrazole-conjugated probes would show higher membrane permeability than carboxylate- or sulfonate-conjugated probes.

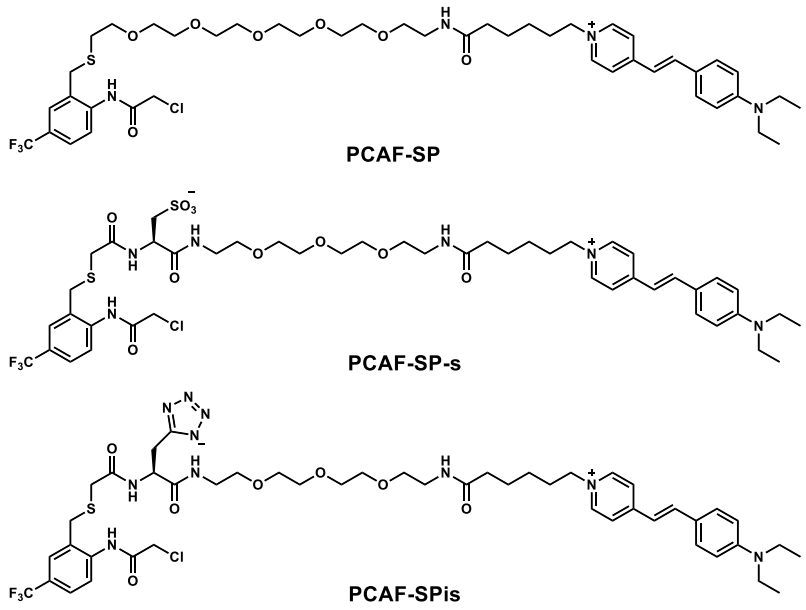

Figure 2-13. PCAF-SP, **PCAF-SP-s** and **PCAF-SPis**.

Table 2-1. clog *P* of zwitterionic PYP-tag labeling probes.

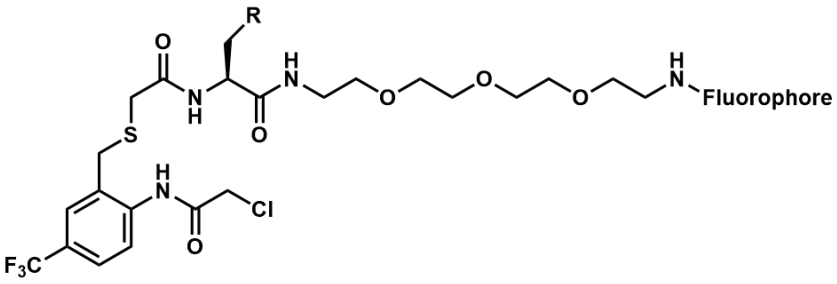

Probe	R =	Fluorophore	clog*P*
PCAF-RBis	tetrazole	RB	2.12
PCAF-RB-c	COO^-	RB	-1.04
PCAF-RB-s	SO_3^-	RB	-2.47
PCAF-SPis	tetrazole	SP	0.97
PCAF-SP-c	COO^-	SP	-2.19
PCAF-SP-s	SO_3^-	SP	-3.62

2.2.2 Synthesis of probes

First of all, PEG5 linker and tetrazole-conjugated linker moieties were synthesized for the preparation of cationic and tetrazole-conjugated probes, respectively. The PEG5 linker moiety with azido and thiol groups (**5**) was synthesized from hexaethylene glycol as a starting material through functional group transformations.

As shown in Scheme 2-1., a Fmoc-protected tetrazole-bearing amino acid derivative (**6**) was synthesized in one step, and conjugated PEG linker moiety with a tetrazole-bearing amino acid that is synthetically accessible, then **7** was obtained through the conjugation of **6** and amine using hexafluorophosphate benzotriazole tetramethyl uronium (HBTU) as a coupling reagent.

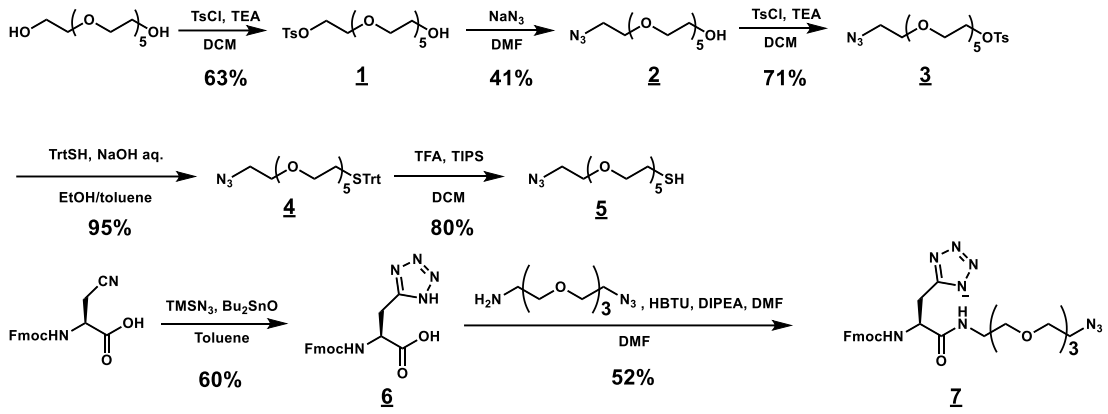

Scheme 2-1. Synthesis of PEG5 linker and tetrazole-conjugated linker moieties.

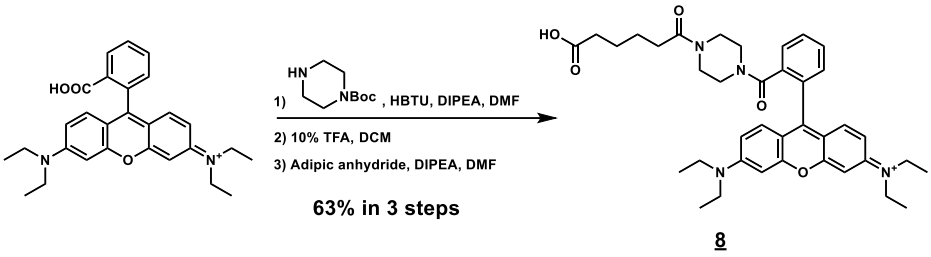

Scheme 2-2. Synthesis of RB carboxylic acid derivative in one-pod synthesis.

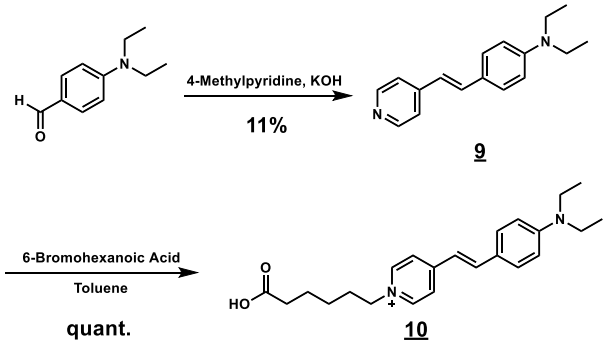

Scheme 2-3. Synthesis of SP carboxylic acid derivative.

The RB derivative (**8**) was successfully synthesized from a commercially available and reasonably priced source, rhodamine B, in one step following Scheme 2-2. In addition, the SP derivative (**9**) was easily prepared from a commercial source, 4-dimethylaminobenzaldehyde, in two steps following Scheme 2-3.

Following the synthetic route of PCAF-based probes in previous work, **11** was synthesized by the conjugation of the ligand moiety and **5** via thioether bonding. After reducing the azido group to an amino group using the Staudinger reaction, **PCAF-RB** was successfully synthesized in three steps, as shown in Scheme 2-4. In terms of the reaction conditions in the final step, reaction condition screening was conducted for acylating the PCAF precursor using **PCAF-Me** as a model compound, indicating that the condition of Entry 4 affords the objective compound in high yield (Table 2-2).

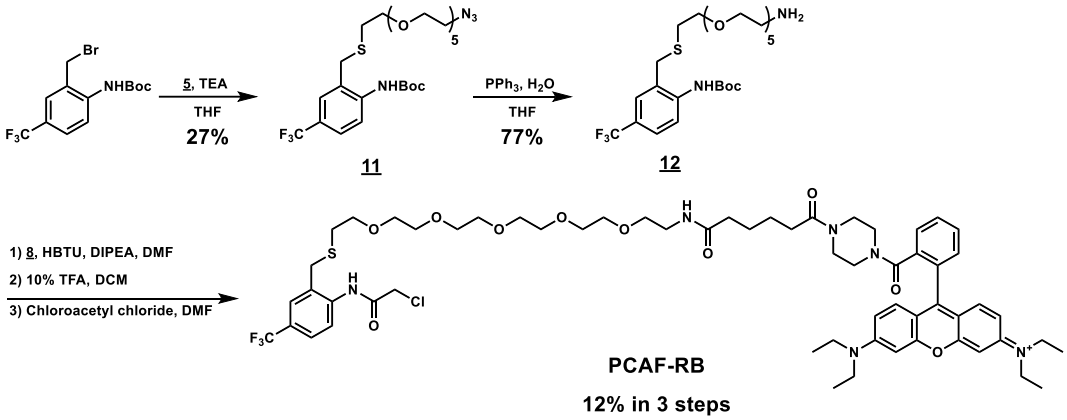

Scheme 2-4. Synthesis of **PCAF-RB**.

Table 2-2. Reaction condition screening of the **PCAF-Me** synthesis

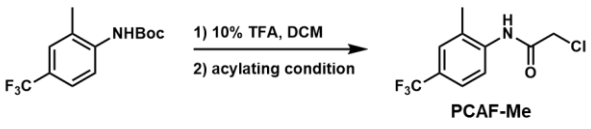

Entry	COOH or electrophile	Coupling reagent	Other conditons	Results
1	*N*-Succinimidyl chloroacetate (2.0 eq.)	-	sat. $NaHCO_3$ aq., 1,4-dioxane	N.D.[a)]
2	Chloroacetic acid (1.5 eq.)	COMU (1.5 eq.)	DIPEA (1.5 eq.), DMF[b)]	N.D.[a)]
3	Chloroacetic acid (2.0 eq.)	T3P (4.0 eq.), HOBt (4.0 eq.)	DIPEA (1.5 eq.), DMF[b)]	29% yield
4	**Chloroacetyl chloride (1.5 eq.)**	**-**	**DMF[b)]**	**88% yield**

a) Product peaks of ^{1}H-NMR were not obtained. b) Super dehydrated solvent

Compound **14** was synthesized by conjugating the ligand precursor (**13**) with the tetrazole-conjugated linker moiety (**7**). Compound **15** was obtained by reducing the azido group to an amino group using the Staudinger reaction, and then **PCAF-RBis** and **PCAF-SPis** were successfully synthesized in three steps.

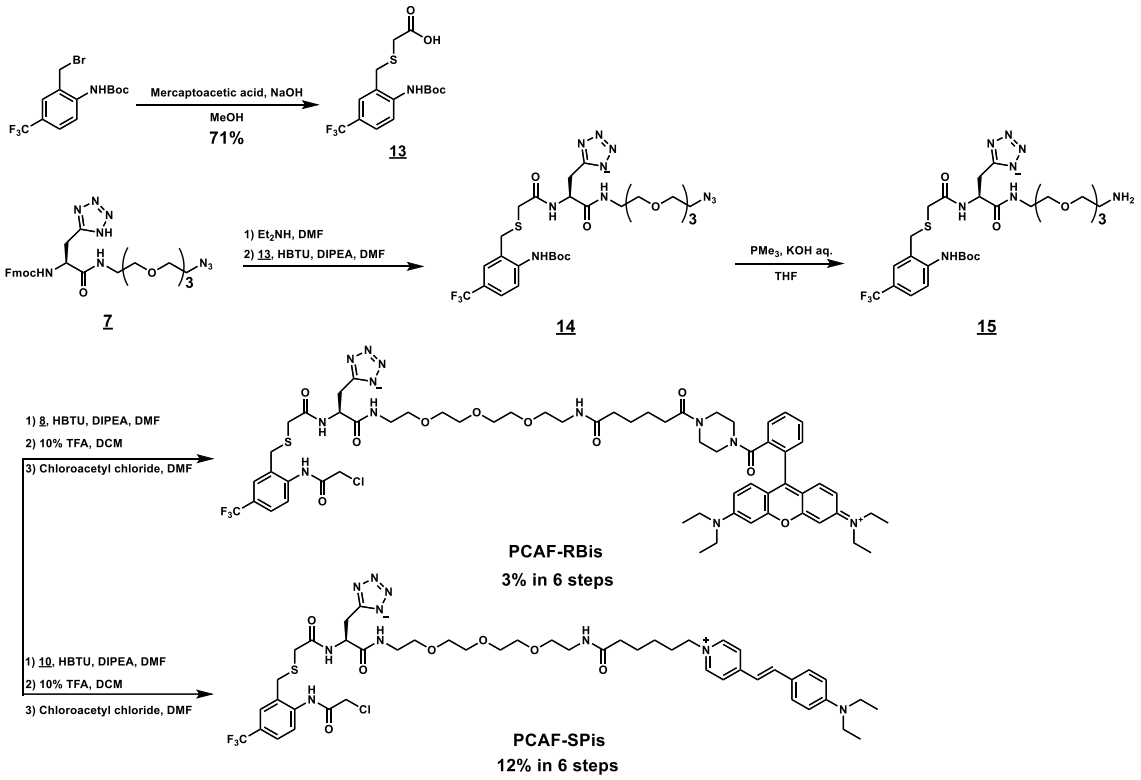

Scheme 2-5. Synthesis of **PCAF-RBis** and **PCAF-SPis**.

2.2.3 In vitro labeling reaction and photophysical properties of probes

Sodium dodecyl sulfate-polyacrylamide gel electrophoresis (SDS-PAGE) analysis was conducted to confirm the proceeding of the labeling reaction between the probes and PYP-tag. Following the labeling reaction, heating for denaturation, and electrophoresis, both Coomassie Brilliant Blue (CBB) staining for protein detection and in-gel fluorescence detection were performed. Fluorescence and CBB bands were observed at the corresponding position of PYP-tag with the addition of the probes. In the absence of the probes, the CBB band was observed at the corresponding position of PYP-tag, while the fluorescence band was not detected. These results indicated that the probes labeled PYP-tag under physiological conditions. As a further consideration for SDS-PAGE analysis using denatured samples, these results supported that the probes formed a covalent bond with PYP-tag. (Figure 2-14).

The photophysical properties of the probes were evaluated under physiological conditions. In both free and bound states, **PCAF-RBis** and **PCAF-SPis** showed higher extinction coefficients (ε) than **PCAF-RB** and **PCAF-SP**, respectively, under physiological conditions (Table 2-3, Figure 2-15 and 2-16). In addition, to reveal the brightness of the probes, the quantum yields of each probe were determined using fluorescence analysis. In terms of the RB-based probes, **PCAF-RBis** and **PCAF-RB** emitted fluorescence in both their free and bound states, indicating that RB-based probes are “always-on” fluorescence probes (Table 2-3, Figure 2-15).

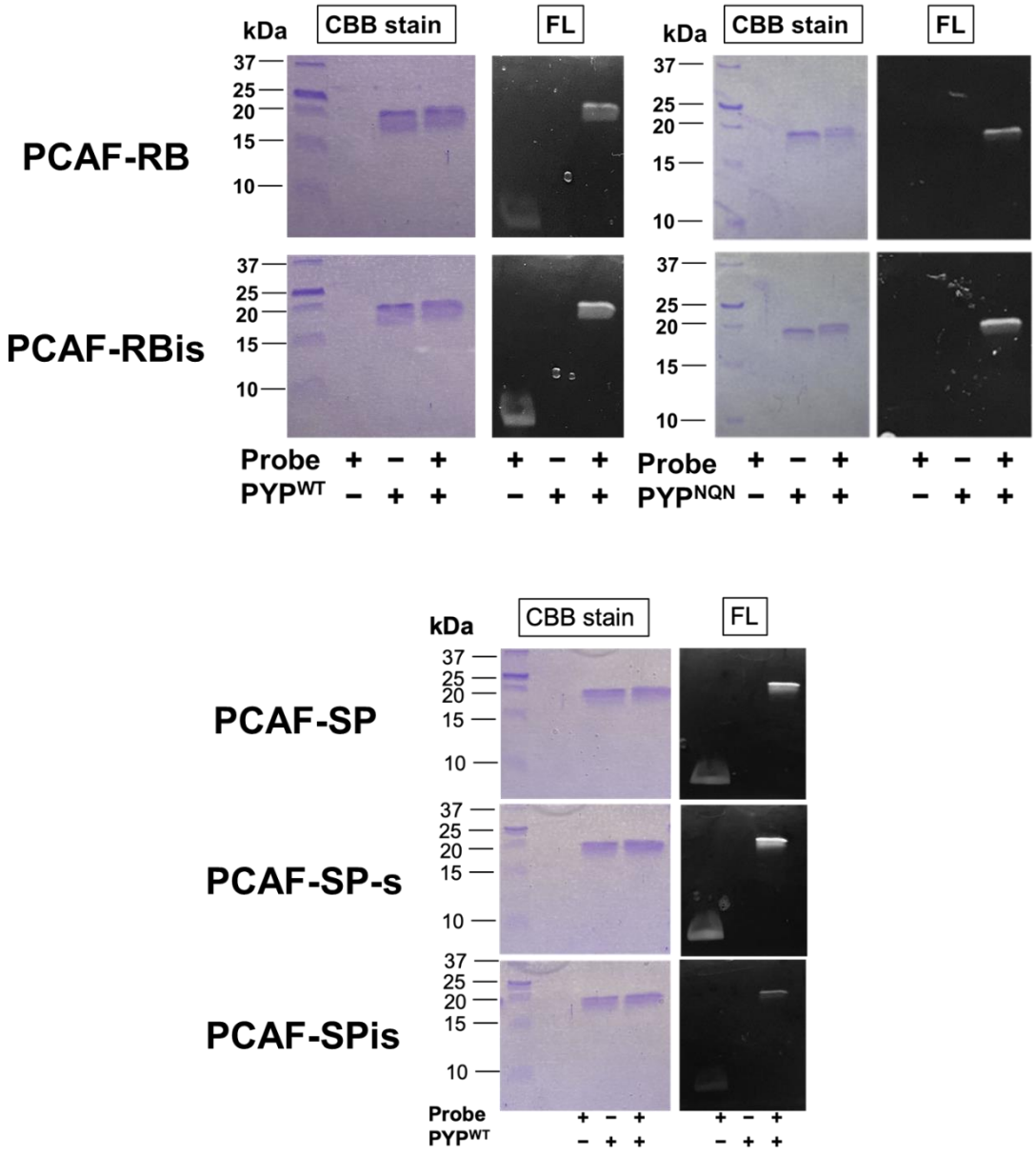

Figure 2-14. The result of CBB staining and fluorescence images of the SDS-PAGE analysis. PYP^{WT} (2.0 μM) and PYP^{NQN} (2.0 μM) incubated with **PCAF-RB** (1.0 μM) or **PCAF-RBis** (1.0 μM) for 30 min. PYP^{WT} (2.0 μM) and PYP^{NQN} (2.0 μM) incubated with **PCAF-SP** (1.0 μM), **PCAF-SPis** (1.0 μM), or **PCAF-SP-s** (1.0 μM) for 20 min. The SDS analysis images were obtained with the excitation at 470 nm. CBB and FL denote coomassie brilliant blue staining and fluorescence images, respectively. Experiments were performed twice with similar results The SDS analysis images were obtained with the excitation at 470 nm. CBB and FL denote coomassie brilliant blue staining and fluorescence images, respectively. Experiments were performed twice with similar results.

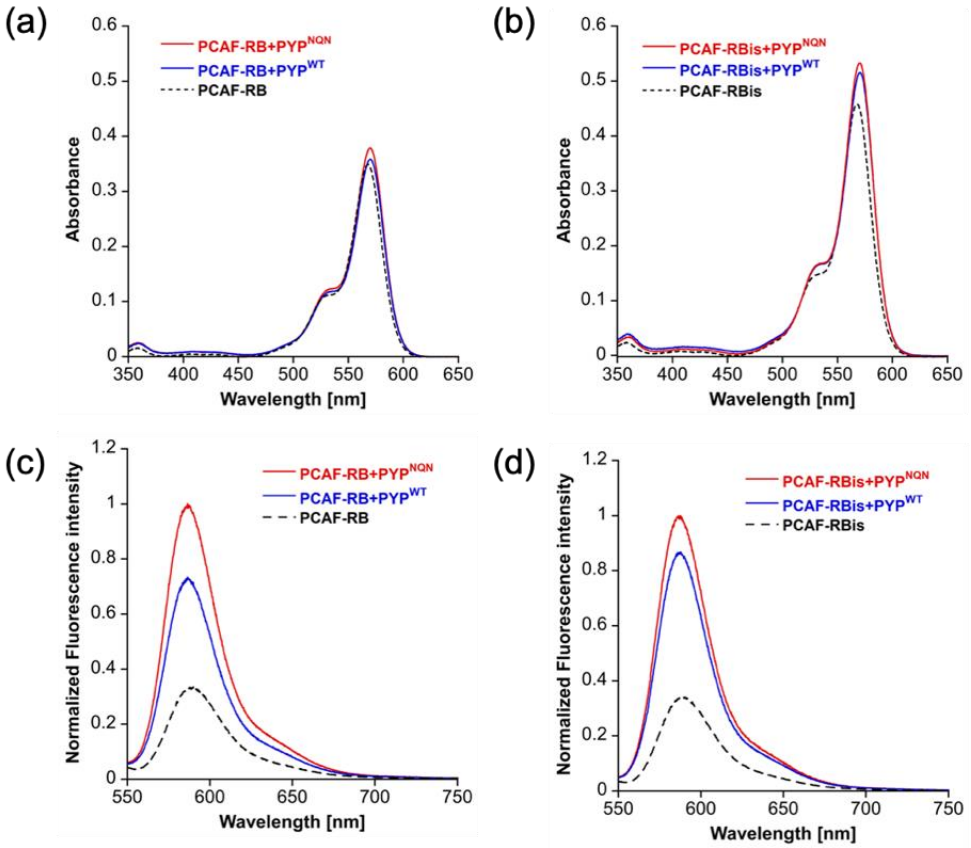

Figure 2-15. (a and b) Absorption spectra of 5.0 μM (a) **PCAF-RB** and (b) **PCAF-RBis** in the absence and presence of 10.0 μM PYP^{WT} or PYP^{NQN} in a solution of 20 mM HEPES, 150 mM NaCl, and 0.1% DMSO buffered to pH 7.4 at 37 °C. (c and d) Normalized fluorescence spectra of 0.5 μM (c) **PCAF-RB** or (d) **PCAF-RBis** in the absence and presence of 1.0 μM PYP^{WT} or PYP^{NQN} in a solution of 20 mM HEPES, 150 mM NaCl, and 0.1% DMSO buffered to pH 7.4 at 37 °C. The spectra were obtained with an excitation of 535 nm.

In addition, these RB-based probes exhibited an increase in their quantum yields upon binding to PYP^{WT} and PYP^{NQN} (Table 2-3, **PCAF-RBis**: 0.29 → 0.61 (PYP^{WT}), 0.70 (PYP^{NQN}); **PCAF-RB**: 0.28 → 0.54 (PYP^{WT}), 0.59 (PYP^{NQN})). Consequently, fluorescence analysis was conducted to evaluate the brightness (extinction coefficients (ε) × fluorescence quantum yields (Φ)) of **PCAF-SPis** and re-evaluate that of **PCAF-SP** and **PCAF-SP-s**. Therefore, all the SP-based probes in free states showed almost no fluorescence under physiological conditions. In contrast, the fluorescence intensity of the probes significantly increased upon binding to PYP^{WT}. In addition, SP-based probes showed an increase in their quantum yield upon binding to PYP^{WT} (Table 2-3, **PCAF-**

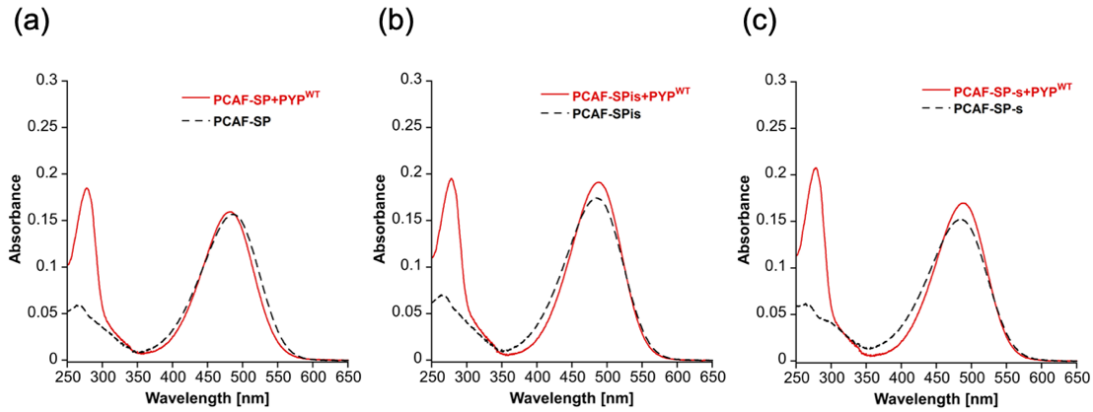

Figure 2-16. (a-c) Absorption spectra of 5.0 μM (a) **PCAF-SP**, (b) **PCAF-SPis**, and (c) **PCAF-SP-s** in the absence and presence of 10.0 μM PYP^{WT} in an aqueous solution of 20 mM HEPES, 150 mM NaCl, and 0.1% DMSO buffered to pH 7.4 at 37 °C.

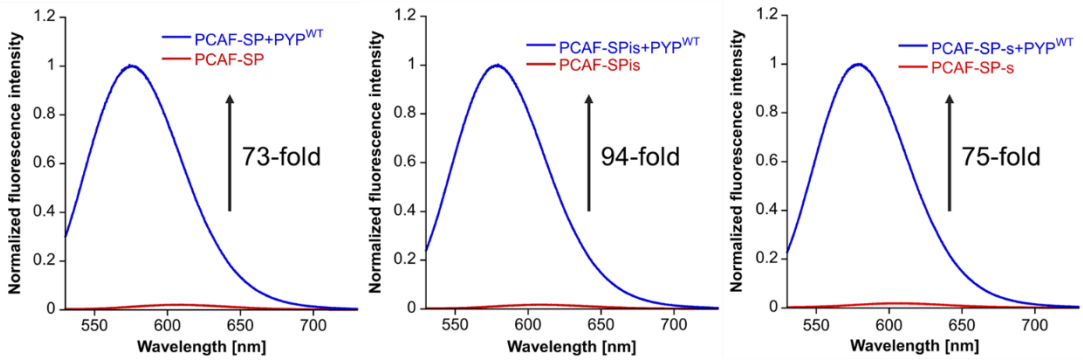

Figure 2-17. Normalized fluorescence spectra of PYP-tag labeling probes (**PCAF-SP**, **PCAF-SPis**, and **PCAF-SP-s**) reacted with/without PYP^{WT}. **PCAF-SP**, **PCAF-SPis**, and **PCAF-SP-s** (5.0 μM) were incubated with/without PYP^{WT} (6.0 μM) for 30 min in the solution of 20 mM HEPES, 150 mM NaCl, and 0.1% DMSO buffered to pH 7.4 at 37°C. All spectra were obtained with the excitation at 484 nm.

SPis: 0.01 → 0.28; **PCAF-SP**: 0.01 → 0.27; **PCA**F-**SP-s**: 0.01 → 0.29). These results indicated that the fluorogenic responses of SP-based probes were observed upon binding to PYP-tag. Then, fluorescence analysis was conducted using SP-based probes and PYP^{NQN}. The brightness of PYP^{NQN} labeled with **PCAF-SP-s** was similar to that of PYP^{WT} labeled with the probe. In contrast, compared with PYP^{WT}, the brightness of PYP^{NQN} labeled with **PCAF-SPis** or **PCAF-SP** was slightly decreased (PCAF-SPis: 1.1×10^4 → 0.87×10^4, PCAF-SP: 0.84×10^4 → 0.75×10^4). These results suggest that

the NQN mutation and the anionic groups of the probes affected the interaction modes between the protein surface and PYP-tag.

Next, fluorescence analysis was performed in triplicate to determine the second-order rate constant (k_2), resulting in k_2 values on the order of 10^3 $M^{-1}s^{-1}$. These results are consistent with the k_2 values of PCAF-based probes reported in a previous study. In terms of the effect of the net charge in RB-based probes, the reaction rate of **PCAF-RBis** with PYP^{WT} was lower than that of **PCAF-RB** with PYP^{WT} (k^2 = 6.3 × 10^3 to 3.4 × 10^3 $M^{-1}s^{-1}$). In addition to fluorescence analysis using PYP^{WT}, PYP^{NQN} was employed to search for combinations of the probes and PYP-tag that exhibit higher *k*2 values and brightness. PYP^{NQN} rapidly binds to PYP-tag labeling probes with anionic groups, compared with PYP^{WT}. As a result, the labeling reaction of **PCAF-RB** with PYP^{NQN} proceeded with a k_2 value similar to that of **PCAF-RB** with PYP^{WT} (PYP^{WT}: 6.3 × 10^3 $M^{-1}s^{-1}$, PYP^{NQN}: 5.7 × 10^3 $M^{-1}s^{-1}$). In contrast, the labeling reaction of **PCAF-RBis** with PYP^{NQN} exhibited a higher k_2 value than that of **PCAF-RBis** with PYP^{WT} (PYP^{WT}: 3.4 × 10^3 $M^{-1}s^{-1}$, PYP^{NQN}: 5.7 × 10^3 $M^{-1}s^{-1}$).

Labeling experiments were conducted to analyze the rate constant of SP-based probes. Focusing on the effect of introducing anionic groups into SP-based probes, the labeling reaction of **PCAF-SPis** with PYP^{WT} exhibited a moderate acceleration compared with **PCAF-SP** with PYP^{WT} (k_2 = 5.9 × 10^3 to 9.1 × 10^3 $M^{-1}s^{-1}$), while **PCAF-SP-s** exhibited a similar reaction rate (k_2 = 5.9 × 10^3 for **PCAF-SP** to 4.4 × 10^3 $M^{-1}s^{-1}$ for **PCAF-SP-s**). Then, the rate constants of the probes with PYP^{WT} and PYP^{NQN} were determined. Focusing on the dye scaffold of the probes, the labeling reaction of **PCAF-RBis** with PYP^{NQN} exhibited a higher k_2 value than that of **PCAF-RBis** with PYP^{WT} (**PCAF-RBis**: k_2 = 3.4 × 10^3 $M^{-1}s^{-1}$ to 7.0 × 10^3 $M^{-1}s^{-1}$), whereas the k_2 value of **PCAF-SPis** with PYP^{NQN} decreased (**PCAF-SPis**: k_2 = 9.1 × 10^3 $M^{-1}s^{-1}$ to 4.1 × 10^3 $M^{-1}s^{-1}$). In terms of the effect of anionic groups in SP-based probes, the rate constant of **PCAF-SPis** and **PCAF-SP** with PYP^{NQN} showed decreased or increased reaction rates compared with the corresponding probes with PYP^{WT} (**PCAF-SPis**: k_2 = 9.1 × 10^3 $M^{-1}s^{-1}$ to 4.1 × 10^3 $M^{-1}s^{-1}$, **PCAF-SP**: k_2 = 5.9 × 10^3 $M^{-1}s^{-1}$ to 21 × 10^3 $M^{-1}s^{-1}$). In addition, the reaction of **PCAF-SP-s** with PYP^{NQN} proceeded with a k_2 value similar to that of **PCAF-SP-s** with PYP^{WT} (**PCAF-SP-s**: k_2 = 4.4 × 10^3 $M^{-1}s^{-1}$ to 3.8 × 10^3 $M^{-1}s^{-1}$). These results indicated that the anionic groups and surface amino acids of PYP-tag affected the labeling kinetics of SP-containing probes in a different manner compared with RB-based probes. Based on the above observations, the interaction mode of SP-containing probes with the protein seems to be different from that of RB-based probes. It is possible that the mutations might lead to an alteration of the protein surface structure that affects the interaction with the anionic

group or the fluorophore moiety of SP-containing probes and the labeling rate, in addition to electrostatic interaction between the protein and the probe.

Table 2-3. Photophysical properties and labeling kinetics

Probe	ε[a] [10^4 M^{-1} cm^{-1}]	Φ_{fl}	Brightness [10^4 M^{-1} cm^1]	k_2[b] [10^3 M^{-1} s^{-1}]
PCAF-RBis	9.2	0.29	2.7	-
PCAF-RBis+PYP^{WT}	10[c]	0.61[c]	6.1	3.4 (±0.5)
PCAF-RBis+PYP^{NQN}	11[c]	0.70[c]	7.7	7.0 (±0.7)
PCAF-RB	7.0	0.28	2.0	-
PCAF-RB+PYP^{WT}	7.2[c]	0.54[c]	3.9	6.3 (±0.7)
PCAF-RB+PYP^{NQN}	7.6[c]	0.69[c]	5.2	5.7 (±0.9)
PCAF-SPis	3.5	0.01	0.035	-
PCAF-SPis+PYP^{WT}	3.8[c]	0.28[c]	1.1	9.1 (±0.9)
PCAF-SPis+PYP^{NQN}	3.0[c]	0.29[c]	0.87	4.1 (±0.4)
PCAF-SP-s	3.1	0.01	0.031	-
PCAF-SP-s+PYP^{WT}	3.4[c]	0.29[c]	0.99	4.4 (±0.2)
PCAF-SP-s+PYP^{NQN}	3.4[c]	0.30[c]	1.0	3.8 (±0.2)
PCAF-SP	3.1	0.01	0.031	-
PCAF-SP+PYP^{WT}	3.1[c]	0.27[c]	0.84	5.9 (±0.4)
PCAF-SP+PYP^{NQN}	3.0[c]	0.25[c]	0.75	21 (±1.0)

All the experiments were conducted in the solution of 20 mM HEPES, 150 mM, and 0.1% containing DMSO buffered to pH 7.4 at 37 ℃.
[a] ε is extinction coefficient at λ_{abs}.
[b] All data were obtained in triplicate experiments.
[c] Data obtained after labeling reactions of PYP-tag proteins with probes were complete.

2.2.4 Live-cell imaging using RB-based probes

To investigate the intracellular distribution and membrane permeability of the RB-based probes (**PCAF-RBis** and **PCAF-RB**), live-cell imaging experiments were conducted using them. Considering that RB-based probes with PYP^{NQN} exhibited high brightness in vitro, PYP^{NQN} was used as a fusion tag. Furthermore, nuclear localization signal (NLS)-fused PYP^{NQN} (PYP^{NQN}-NLS) was employed to express PYP-tag in the nucleus. When cells expressing PYP^{NQN}-NLS are incubated with the probes, fluorescence signals should be observed in the nucleus. Thus, it is possible to identify whether the signals in cytoplasmic regions are off-target signals. Based on this consideration, the author considered that live cells expressing PYP^{NQN}-NLS are preferred systems for evaluating the labeling ability and cytoplasmic accumulation levels of the probes from fluorescence signals.

HEK293T cells were transfected with a plasmid (pcDNA3.1(+)–PYP^{NQN}-NLS or empty vector) using Lipofectamine 3000 reagent according to the procedures described in the experimental section. After incubation of transfected cells with **PCAF-RBis** for 30 min, the cells were washed to remove free probes, and fluorescence images were then obtained under a microscope. Therefore, fluorescence signals were detected only from the nucleus of the cell expressing PYP^{NQN}-NLS, while fluorescence signals in the

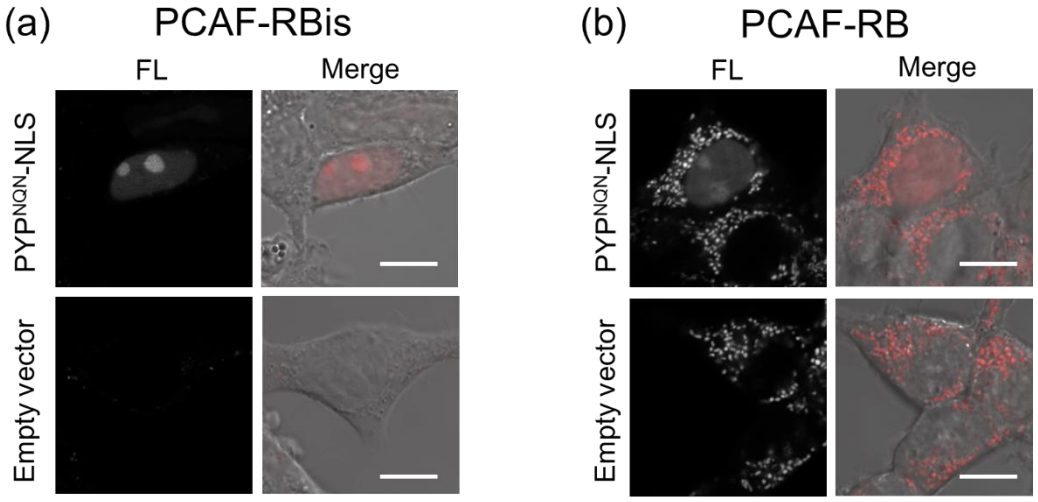

Figure 2-18. Fluorescence and phase contrast-merged images of HEK293T cells expressing HA-PYP^{NQN}-NLS or mock cells (transfected with empty vector) stained with (a) **PCAF-RBis** (5.0 μM) and (b) **PCAF-RB** (5.0 μM). The images were measured at 566–685 nm emission with the excitation at 561 nm. Experiments were performed twice, giving similar results. Scale bars, 10 μm. FL denotes fluorescence image.

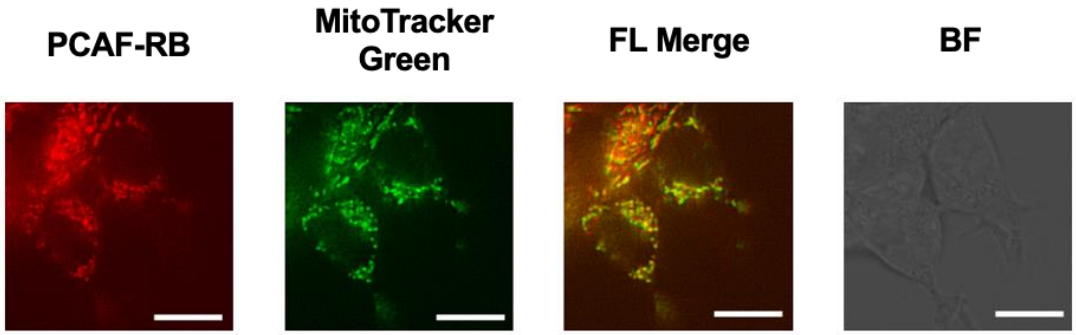

Figure 2-19. Localization analysis of **PCAF-RB** (100 nM) in HEK293T cells with MitoTracker Green (100 nM). The images were measured at 560/40 (green) and 630/75 (red) nm emission with the excitation at 470/40 and 525/50 nm, respectively. FL and BF denote the fluorescence image and bright field image, respectively. FL Merge indicates the FL Red image merged with the FL green image. Scale bars, 10 μm.

cytoplasmic region were not detected. Compared with PYP^{NQN}-NLS expressing cells, fluorescence signals were not observed in mock cells (transfected with an empty vector) with the addition of **PCAF-RBis** under identical conditions. These images demonstrated that **PCAF-RBis** can successfully visualize live-cell intracellular proteins without non-specific signals. Nuclei-localized protein imaging using PCAF-RB was then performed. As a result, fluorescence signals were observed not only in the nucleus but also in the cytoplasm. These signals in the cytoplasmic region were not consistent with PYP-tag localization (Figure 2-18), indicating that **PCAF-RB** showed non-specific accumulation in the cytoplasm. Furthermore, dual-color imaging using **PCAF-RB** and MitoTracker Green FM was performed for the localization analysis, resulting in good agreement with the fluorescence signals derived from both probes. The result indicated that **PCAF-RB** accumulated in the mitochondria (Figure 2-19). These results demonstrated that undesirable mitochondrial accumulation was suppressed by the introduction of tetrazole into the probe.

2.2.5 Live-cell imaging using SP-based probes

Live-cell imaging experiments using **PCAF-SP** and **PCAF-SP-s** were previously performed by the author's group. **PCAF-SP** can be applied to visualize mitochondria-localized PYP, while the probe could not be used for non-mitochondrial protein imaging owing to non-specific illuminations. These results are consistent with the intracellular behavior of cationic probes in live-cell protein imaging. In contrast, **PCAF-SP-s** can be applied for membrane-localized protein selectively labeling probe by conducting the imaging experiments using **PCAF-SP-s** and **PCAFred** (a membrane-permeable PYP-tag labeling probe) in live cells co-expressing PYP^{WT}-NLS and PYP^{WT}-fused epidermal growth factor receptor (EGFR) (expressing a PYP-tag on the cell surface) (Figure 2-20).

In this study, the author demonstrated that **PCAF-SP-is** can visualize the intracellular proteins without undesired accumulations. Encouraged by the observation of fluorogenic responses of SP-based probes upon binding to PYP-tag, the author conducted no-wash imaging to evaluate the fluorogenic responses of these probes in live cells. Considering that SP-based probes with PYP^{WT} exhibited high brightness in vitro, the author selected PYP^{WT} as PYP-tag that was expressed in live cells. To express a PYP-tag in the nucleus, HEK293T cells were transfected with the plasmid (pcDNA3.1(+)–PYP^{WT}-NLS or empty vector) using Lipofectamine 3000 reagent according to the procedures described in the experimental section. As shown in Figure 2-21, fluorescence signals appeared in the nucleus of transfected cells upon the addition of **PCAF-SPis**. In the cells expressing PYP-tag, the staining pattern of PCAF-SPis showed a similar pattern to **PCAF-RBis**. Compared with PYP^{WT}-NLS-expressing cells, fluorescence signals did not appear in mock cells with the addition of **PCAF-SPis** under identical conditions. These images demonstrated that **PCAF-SPis** can be applied for no-wash live-cell imaging of the intracellular proteins without non-specific signals. In contrast, fluorescence signals were observed in the cytoplasm of **PCAF-SP**-treated cells, indicating that **PCAF-SP** exhibited non-specific fluorescence since these signals were not consistent with PYP-tag distribution (Figure 2-21).

The signals of **PCAF-RB** in the cytoplasm were brighter than those in the nucleus, whereas the brightness of **PCAF-SP** was similar in the nucleus and cytoplasm. These results suggest that fluorogenic probes can reduce organelle accumulation, which is caused by the cationic nature of dye scaffolds, compared with always-on probes, although

the fluorogenic response of the probes is not sufficient to completely suppress the organelle accumulation.

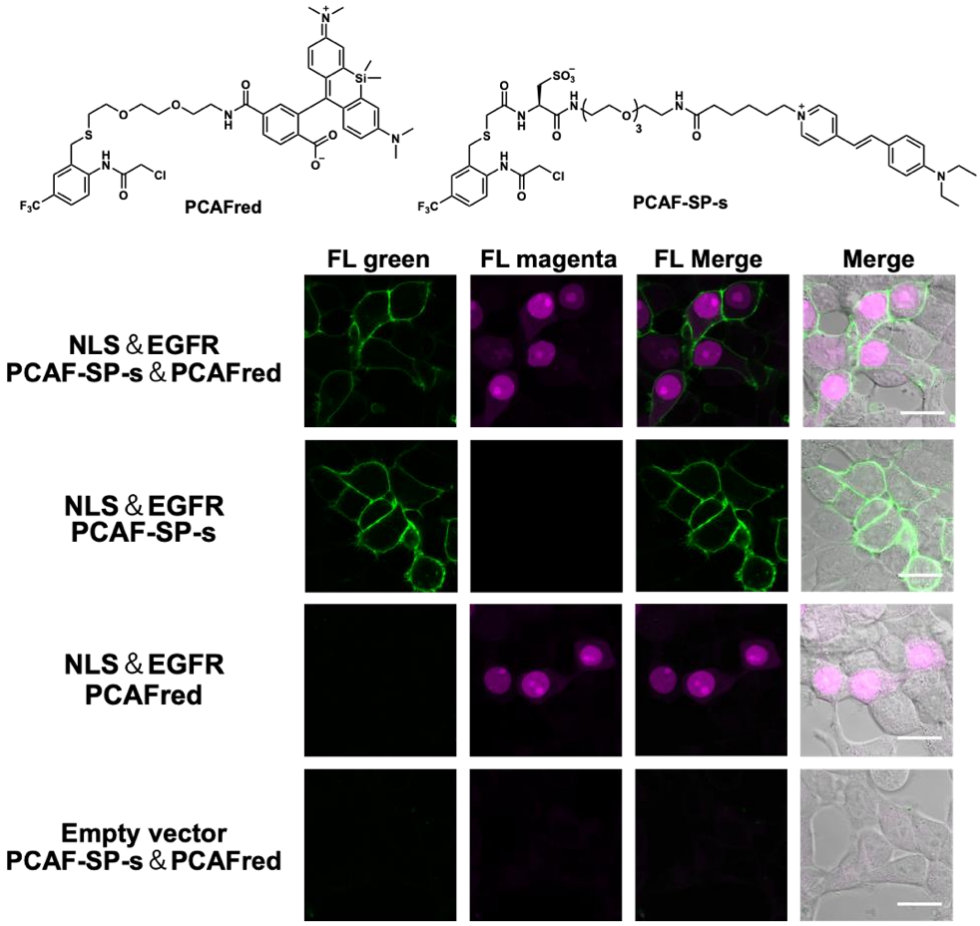

Figure 2-20. Fluorescence images of HEK293T cells co-expressing HA-PYP^{WT}-NLS and HA-PYP^{WT}-EGFR or mock cells (transfected with empty vector) labeled with **PCAF-SP-s** (1.0 μM) and **PCAFred** (1.0 μM). The images were obtained with the excitation at 488 nm and 633 nm by detecting 500–600 (green) and 660–710 (magenta) nm emissions, respectively. Scale bars, 10 μm. FL denotes fluorescence image. FL Merge and Merge denote the magenta fluorescence images merged with that of the green and FL Merge overlayed with phase contrast images, respectively. Experiments were performed twice, giving similar results.

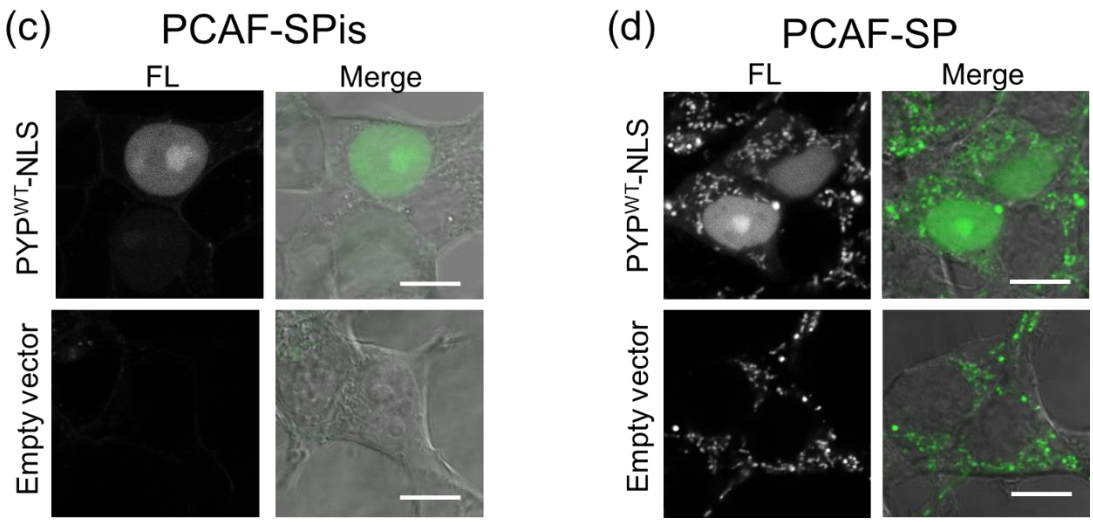

Figure 2-21. Fluorescence and phase contrast-merged images of HEK293T cells expressing HA-PYP^{WT}-NLS or mock cells stained with (a) **PCAF-SPis** (1.25 μM) or (b) **PCAF-SP** (1.25 μM). The images were measured at 550–650 nm emission with the excitation at 488 nm. Experiments were performed twice, giving similar results. Scale bars, 10 μm. FL denotes fluorescence image.

2.2.6 Labeling efficiency of SP-based probes

To evaluate the labeling efficiency, the author modified a method, which was previously reported.[20] In this study, HA-tag-fused PYP-NLS was labeled with SP-based probes (in this work; **PCAF-SP** or **PCAF-SPis**) and purified using anti-HA tag antibody-conjugated beads. The samples were then subjected to SDS-PAGE. Since the band mobility of labeled proteins shifts compared with that of unlabeled proteins, labeling efficiency can be estimated by the degree of band shift. In the absence of the probes, the author observed intense and weak CBB bands, one detected in the lower position and the other in the upper (Figure 2-22a, lane 1). One probable reason for this phenomenon is the presence of posttranslational processing, such as N-terminal deletion, since labeling reactions also gave two fluorescent bands, which indicate that both are derived from PYP-tag proteins. The CBB band was shifted from the lower position to the upper upon labeling reactions and was overlapped with the unlabeled band in the upper position (Figure 2-22a, lanes 3 and 5). The author thus decided to determine the intensity ratio (the upper band to the lower) of both the CBB bands, whose increment is the estimated efficiency of the labeling reactions (Figure 2-22b). The ratio increased by approximately 10% and 20% upon the addition of **PCAF-SPis** and **PCAF-SP**, respectively, compared with the unlabeled control (**PCAF-SPis**: 0.44→0.53, **PCAF-SP**: 0.44→0.62). These results indicate that the labeling efficiency of **PCAF-SP** is higher than that of **PCAF-SPis**, likely due to the higher cell membrane permeability of **PCAF-SP** compared with **PCAF-SPis**.

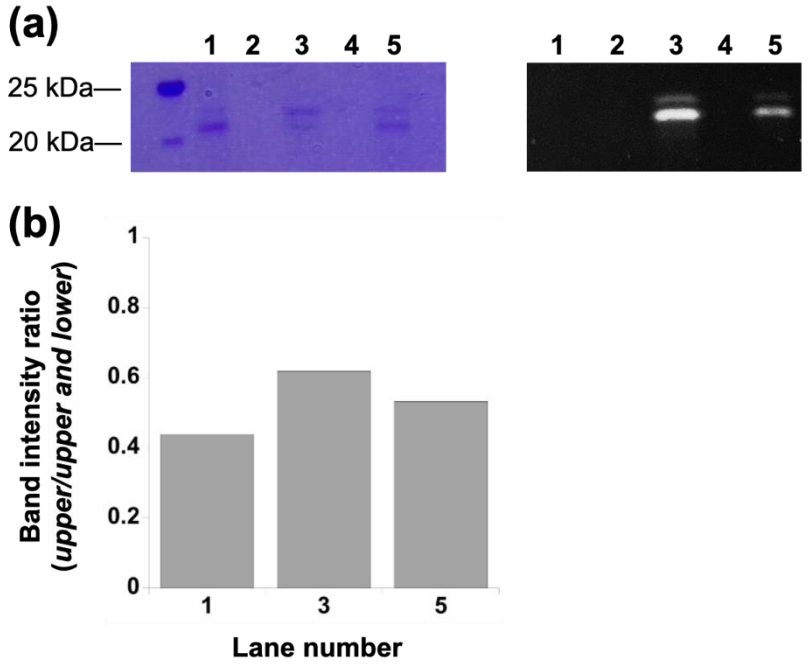

Figure 2-22. SDS-PAGE analysis of the probe labeling efficiency in live cells. (a) The CBB and fluorescence images were shown in the left and the right, respectively. The latter was obtained with the excitation at 470 nm. Lane 1: sample of cells expressing HA-PYP-NLS incubated without the probes, Lane 2: sample of non-transfected cells incubated with 10 μM **PCAF-SP**, Lane 3: sample of cells expressing HA-PYP-NLS incubated with 10 μM **PCAF-SP**, Lane 4: sample of non-transfected cells incubated with 10 μM **PCAF-SPis**, Lane 5: sample of cells expressing HA-PYP-NLS incubated with 10 μM **PCAF-SPis** (b) CBB band intensity ratio (upper band/upper and lower bands) in lanes 1, 3, and 5

2.3 Conclusion

In this chapter, tetrazole-conjugated protein labeling probes containing cationic dye scaffolds, rhodamine B and styryl pyridinium derivatives, were developed. The tetrazole-conjugated probes could be applied for live-cell intracellular protein imaging without undesired accumulation, while cationic probes based on RB and SP show non-specific accumulation in the cytoplasm.

As a result of fluorescence analyses, RB-based probes in both free and bound states was confirmed to show fluorescence under physiological conditions. In contrast, SP-based probes show significant fluorogenicity upon binding to PYP-tag protein. Live-cell intracellular protein imaging experiments were conducted to investigate the intracellular distribution and membrane permeability of RB-based probes (**PCAF-RBis** and **PCAF-RB**). **PCAF-RBis** successfully visualized intracellular proteins without non-specific signals, whereas **PCAF-RB** showed non-specific mitochondrial accumulation. Then, localization analysis with MitoTracker Green FM confirmed **PCAF-RB** mitochondrial accumulation. These results demonstrate that the introduction of tetrazole into probes suppresses undesirable accumulation. Although **PCAF-SP** and **PCAF-SP-s** cause serious problems in intracellular protein imaging, the author demonstrated that a novel SP-based probe, **PCAF-SPis**, which was developed by the author, can be applied for non-wash intracellular protein imaging in live cells.

2.4 Experimental sections

2.4.1 General

General chemicals were supplied by Tokyo Chemical Industries, Wako Pure Chemical Industries, Sigma-Aldrich Chemical Co., and Kishida Chemical Co. and used without further purification. NMR spectra were recorded on a BRUKER AscendTM 500 instrument at 500 MHz for ^{1}H NMR and at 125 MHz for ^{13}C NMR or on a JEOL JNM-ECA 600 spectrometer using TMS as an internal standard. FAB-High-resolution mass spectra (HRMS) were recorded using a JEOL JMS-700 instrument. ESI-HRMS was performed using a MicrOTOF II-BC instrument (Bruker). Silica gel chromatography was performed using BW-300 silica (Fuji Silysia Chemical Ltd.) or a Biotage® IsoleraTM One instrument with a pre-packed Biotage® SNAP HC D column or Sfär C18 column. HPLC purification was performed using an Inertsil ODS-3 column (4.6 or 10.0 mm × 250 mm, GL-Science, Inc.) and a TSKgel ODS-80Ts (4.6 or 20.0 mm × 250 mm, TOSOH Co.). Size exclusion chromatography was performed using a SuperdexTM 75 10/300 GL column (GE Healthcare Life Science) connected to an NGC Chromatography System (Bio-Rad). Fluorescence spectra were measured using an F7000 spectrometer (Hitachi) fitted with a photomultiplier at a voltage of 700 V. UV-vis absorption spectra were obtained using a V-650 spectrometer (Jasco). Live fluorescent cell images were acquired using a confocal laser-scanning microscope (Zeiss, LSM-880) or a fluorescence microscope (Keyence, BZ-X710) with a 63× or 60× lens, respectively.

2.4.2 Synthetic procedures

Synthesis of **1**

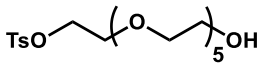

1

Hexaethylene glycol (20.0 g, 70.8 mmol) and TEA (19.8 mL, 142 mmol) were dissolved in DCM (42 mL) and cooled to 0 °C. TsCl (3.38 mg, 17.7 mmol) dissolved in DCM (10 mL) was added dropwise to the reaction mixture, which was then stirred at room temperature for 3 h. The reaction mixture was washed with water and brine. The organic layer was dried over Na_2SO_4, filtered, and evaporated under reduced pressure. The residual material underwent purification through silica gel column chromatography (DCM/MeOH = 95/5 to 90/10 as eluent) to yield compound **1** (4.86 g, 11.2 mmol) with a 63% overall yield.

^{1}H NMR (500 MHz, $CDCl_3$): δ 7.80 (d, *J* = 8.0 Hz, 2H), 7.34 (d, *J* = 8.0 Hz, 2H), 4.16 (t, *J* = 5.0 Hz, 2H), 3.72-3.58 (m, 22H), 2.77 (br, 1H), 2.45 (s, 3H). **^{13}C NMR (125 MHz, $CDCl_3$):** δ 144.8, 133.0, 129.8, 128.0, 72.7, 72.6, 70.7, 70.6, 70.6, 70.5, 70.5, 70.3, 70.2, 69.3, 68.7 61.7, 61.7, 21.6. **HRMS (ESI+)**: Calcd for $[M+Na]^+$ 459.1659, found 459.1670

Synthesis of **2**

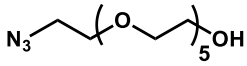

2

NaN_3 (1.95 g, 30.0 mmol), compound **1** (2.65 g, 6.00 mmol), and DMF (6 mL) were stirred at 50 °C overnight. The white precipitate was removed by filtration and the residue was washed with AcOEt. The filtrate was concentrated *in vacuo*, then the resultant was purified by silica gel column chromatography (Hexane/AcOEt = 50/50 to 20/80 as eluent) to yield compound **2** (740 mg, 2.44 mmol) with a 41% overall yield.

^{1}H NMR (500 MHz, $CDCl_3$): δ 3.73-3.60 (m, 22H), 3.39 (t, *J* = 5.0 Hz, 2H), 2.20 (br, 1H), **^{13}C NMR (125 MHz, $CDCl_3$):** δ 72.6, 70.7, 70.6, 70.6, 70.6, 70.5, 70.3, 70.0, 61.7, 50.7, 36.5, 31.4. **HRMS (ESI+):** Calcd for $[M+Na]^+$ 330.1636, found 330.1652

Synthesis of **3**

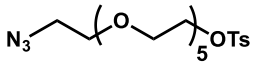

3

TsCl (4.51 g, 23.7 mmol) in DCM (72 mL) was added dropwise to a stirred solution of compound **2** (2.43 g, 7.89 mmol) and TEA (3.30 mL, 23.7 mmol) in DCM (40 mL) at room temperature. Subsequently, the solution was stirred overnight at room temperature. The reaction mixture was washed with water and brine. The solution was dried over Na_2SO_4, filtered, and evaporated. The residue was purified by silica gel column chromatography (DCM/MeOH = 99/1 to 90/10 as eluent) to obtain compound **3** (2.68 g, 5.80 mmol) with a 73% overall yield.

^{1}H NMR (500 MHz, $CDCl_3$): δ 7.80 (d, *J* = 8.0 Hz, 2H), 7.34 (d, *J* = 8.0 Hz, 2H), 4.16 (t, *J* = 5.0 Hz, 2H), 3.70-3.38 (m, 22H), 2.45 (s, 3H). **^{13}C NMR (125 MHz, $CDCl_3$):** δ 114.8, 133.0, 129.8, 128.0, 70.8, 70.7, 70.7, 70.6, 70.6, 70.6, 70.5, 70.0, 69.3, 68.7. 21.5. **HRMS (ESI+):** Calcd for $[M+Na]^+$ 484.1724, found 484.1705

Synthesis of **4**

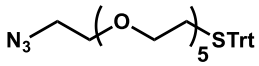

4

NaOH (391 mg, 9.95 mmol) in H_2O (4.4 mL) was added to a solution of triphenylmethanethiol (2.19 g, 7.94 mmol) in ethanol/toluene (1/1) (30 mL). After the addition, compound **3** (3.00 g, 6.50 mmol) in ethanol/toluene (1/1) (30 mL) was added to the solution at room temperature, then the solution was stirred at room temperature for 5 h. The reaction mixture was then washed with sat. $NaHCO_3$ aq. and brine. The solution was dried over Na_2SO_4, filtered, and evaporated. The residue was purified by flash column chromatography on silica gel (Hexane/ethyl acetate = 10/90 to 30/70 as eluent) to obtain compound **4** (3.49 g, 6.16 mmol) with a 95% overall yield.

^{1}H NMR (500 MHz, $CDCl_3$): δ 7.41 (m, 6H), 7.27 (m, 6H), 7.20 (m, 3H), 3.65-3.44 (m, 24H), 3.38 (t, *J* = 5.0 Hz, 2H), 3.30 (t, *J* = 7.0 Hz, 2H). **^{13}C NMR (125 MHz, $CDCl_3$):** δ 44.8, 129.6, 127.9, 126.7, 70.7, 70.7, 70.6, 70.6, 70.6, 70.6, 70.5, 70.2, 70.0, 69.6, 66.6, 50.7, 31.6. **HRMS (ESI+):** Calcd for $[M+Na]^+$ 588.2503, found 588.2489

Synthesis of **5**

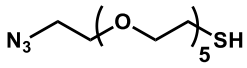

5

TFA (18 mL) was added dropwise to a stirred solution of compound **4** (1.05 g, 1.77 mmol) and triethylsilane (246 mg, 2.21 mmol) in DCM (110 mL) at room temperature and the solution was stirred at room temperature for 2 h. The reaction mixture was concentrated *in vacuo*. The residue was purified by flash column chromatography on silica gel (DCM to DCM/MeOH = 90/10 as eluent) to obtain compound **5** (455 mg, 1.41 mmol) with an 80% overall yield.

^{1}H NMR (500 MHz, DMSO-d_6): δ 3.61-3.49 (m, 20H), 3.40 (t, *J* = 5.0 Hz, 2H), 2.64-2.59 (m, 2H), 2.28 (t, *J* = 8.0 Hz, 1H). **^{13}C NMR (125 MHz, DMSO-d_6):** δ 72.6, 70.3, 70.3, 70.2, 70.2, 69.9, 69.7, 50.5, 23.9. **HRMS (FAB+):** Calcd for $[M]^+$367.2380, found 367.2390.

Synthesis of **6**

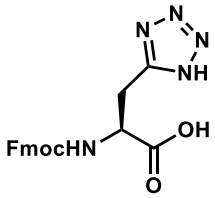

6

A solution of Fmoc-Ala(3-CN)-OH (336 mg, 1.00 mmol), $TMSN_3$ (460 mg, 4.00 mmol) and Bu_2SnO (224 mg, 0.900 mmol) in toluene (5 mL) was stirred at 100 °C for 2 h. The reaction mixture was concentrated *in vacuo*. The residue was purified by silica gel column chromatography (DCM/MeOH = 10/1 to MeOH as eluent) to obtain compound **6** (226 mg, 0.596 mmol) with a 60% overall yield.

^{1}H NMR (500 MHz, DMSO-d_6): δ 7.88 (d, *J* = 7.5 Hz, 2H), 7.83 (d, *J* = 8.5 Hz, 1H), 7.67-7.30 (m, 6H), 4.49 (ddd, *J*= 15.0, 8.5, 7.5 Hz, 1H), 4.27-4.19 (m, 3H), 3.40 (dd, *J* = 15.0, 6.0 Hz, 1H), 3.27 (dd, *J* = 15.0, 6.0 Hz, 1H). **^{13}C NMR (125 MHz, DMSO-d_6)** δ 172.5, 156.3, 154.1, 144.2, 141.2, 128.1, 127.6, 125.7, 125.6, 120.6, 66.2, 52.7, 47.0, 25.9. **HRMS (FAB-):** Calcd for $[M]^-$ 378.1208, found 378.1207.

Synthesis of **7**

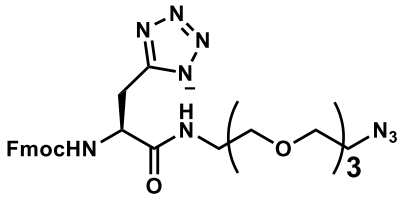

7

DIPEA (306 mg, 2.37 mmol) and compound **6** (300 mg, 0.790 mmol) were dissolved in DMF (7.5 mL). HBTU (299 mg, 0.790 mmol) was added to the resulting solution and was stirred at 0 °C for 45 min. 11-Azido-3, 6, 9-trioxaundecan-1-amine (205 mg, 0.940 mmol) was added to the reaction mixture, warmed to room temperature, and stirred overnight. The reaction solution was concentrated *in vacuo*, then the residue was purified by column chromatography (DCM/MeOH = 99/1 to 1/1 as eluent) to yield the title compound (239 mg, 0.410 mmol) as a colorless oil with a 52% overall yield.
^{1}H NMR (600 MHz, DMSO-*d*$_6$): δ 8.02-7.31 (m, 9H) 4.49-4.46 (m, 1H) 4.29-4.19 (m, 3H), 4.49 (ddd, *J* = 15.0, 8.5, 7.5 Hz, 1H), 4.27-4.19 (m, 3H), 3.58-3.14 (m, 18H).
HRMS (ESI-): Calcd for $[M-H]^-$ 578.2481, found 578.2457.

Synthesis of **8**

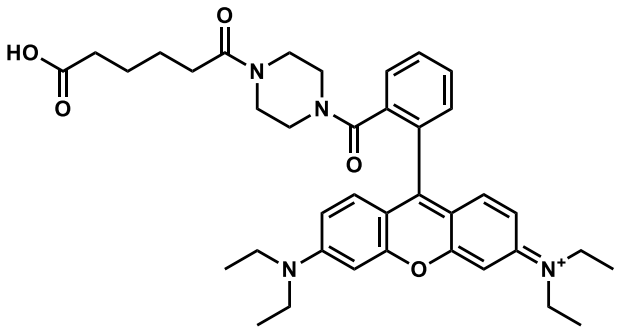

8

Rhodamine B (479 mg, 1.00 mmol), *tert*-butyl 1-piperazinecarboxylate (668 mg, 1.89 mmol), and DIPEA (194 mg, 1.50 mmol) were dissolved in DMF (6.5 mL). COMU (514 mg, 1.20 mmol) was added to the resulting solution at 0 °C and stirred at 0 °C for 45 min. The reaction mixture was heated to room temperature and stirred overnight. The reaction solution was concentrated *in vacuo*, and then 10% TFA in DCM was added to the residue and stirred at room temperature overnight. The reaction solution was concentrated *in vacuo*, and Adipic Anhydride (128 mg, 1.00 mmol) and DIPEA (258 mg, 2.00 mmol) were added to the residue and stirred at 40 °C for 6 h. The reaction solution was

concentrated *in vacuo* and the residue was purified by silica gel column chromatography (DCM/MeOH = 99/1 to 90/10 as eluent) to yield compound **8** (405 mg, 0.63 mmol) with a 63% overall yield.

^{1}H NMR (600 MHz, Acetone-d_6) δ 7.80-7.74 (m, 3H), 7.59-7.57 (m, 1H), 7.34 (d, *J* = 9.6 Hz, 2H), 6.96 (d, *J* = 3.0 Hz, 2H), 3.78 (q, *J* = 3.0 Hz, 8H), 3.60-3.31 (m, 8H), 2.33-2.29 (m, 3H), 1.59-1.57 (m, 4H), 1.33 (t, *J* = 7.2 Hz, 12H). **^{13}C NMR (125 MHz, MeOD-d_4)** δ 177.2, 174.0, 169.7, 159.4, 157.3, 157.1, 136.6, 133.2, 132.3, 131.8, 131.3, 129.0, 114.5, 114.9, 97.4, 46.9, 43.2, 42.8, 34.6, 33.6, 25.8, 25.6, 12.8. **HRMS (FAB+):** Calcd for $[M]^+$ 639.3541, found 639.3545.

Synthesis of **9**

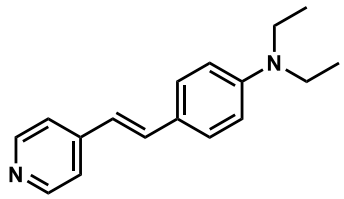

9

A mixture of 4-methylpyridine (14.9 g, 160 mmol), 4-(dimethylamino)benzaldehyde (3.55 g, 20.0 mmol) and potassium hydroxide (1.23 g, 22.0 mmol) was heated to 125°C and stirred for 2h. Then the mixture was cooled to room temperature, the precipitate was poured into ice water, filtered, and the yellow precipitate was washed with cold water. The precipitate was recrystallized from ethanol, to obtain **9** as a bright yellow crystalline solid (557 mg, 2.21 mmol) with a 28% yield.

^{1}H NMR (500 MHz, $CDCl_3$): δ 8.50-8.49 (m, 2H), 7.41 (d, *J* = 9.0 Hz, 2H), 7.30 (d, *J* = 6.0 Hz, 2H), 7.22 (d, *J* = 16.8 Hz, 1H), 6.76 (d, *J* = 16.8 Hz, 1H), 6.66 (d, *J* = 9.0 Hz, 1H), 3.39 (q, *J* = 7.2 Hz, 4H), 1.19 (t, *J* = 7.2 Hz, 6H). **^{13}C NMR (125 MHz, $CDCl_3$):** δ 150.0, 148.2, 145.7, 133.4, 128.6, 123.3, 120.5, 120.3, 111.5, 44.4, 12.6.

Synthesis of **10**

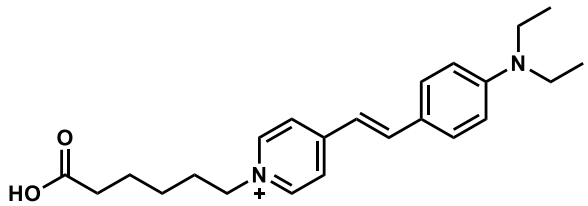

10

A mixture of 6-bromohexanoic acid (780 mg, 4.00 mmol) and compound **9** (253 mg, 1.00) in toluene was heated to 115°C for 16 h; then the mixture was cooled to room temperature. The reaction was filtered, and the precipitate was washed with hexanes and ethyl acetate. The solution of was concentrated *in vacuo*, then the residue was purified by flash column chromatography on silica gel (DCM/MeOH = 90/10 as eluent) to yield compound **10** as a red solid (336 mg, 0.850 mmol) with a 93% overall yield.

^{1}H NMR (500 MHz; MeOD-*d*$_4$): δ 8.56 (d, *J* = 7.0 Hz, 2H), 7.94 (d, *J* = 7.0 Hz, 2H), 7.81 (d, *J* = 16 Hz, 1H), 7.58 (d, *J* = 9.0 Hz, 2H,), 7.05 (d, *J* = 16 Hz, 1H), 6.75 (d, *J* = 9.0 Hz, 2H), 4.41 (t, *J* = 7.0 Hz, 2H), 3.48 (q, *J* = 7.0 Hz, 4H), 2.18 (t, *J* = 7.5 Hz, 2H), 1.97 (tt, *J* = 7.5 Hz, 2H), 1.68-1.65 (m, 2H), 1.39 (tt, *J* = 7.5 Hz, 2H), 1.20 (t, *J* = 7.0 Hz, 6H); **^{13}C NMR (125 MHz, CDCl$_3$):** δ 182.3, 156.4, 151.6, 144.5, 144.3, 132.0, 123.6, 123.5, 117.2, 112.7, 60.9, 45.5, 38.6, 31.9, 26.9, 26.7, 12.9. **HRMS (FAB+):** Calcd for $[M]^+$367.2380, found 367.2390.

Synthesis of *tert*-butyl (2-(bromomethyl)-4-(trifluoromethyl)phenyl)carbamate

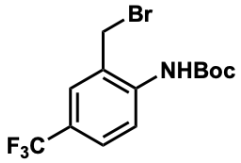

This compound was synthesized following a reported procedure.[20]

Synthesis of **11**

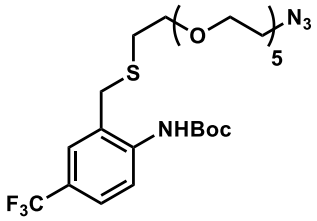

11

tert-Butyl (2-(bromomethyl)-4-(trifluoromethyl)phenyl)carbamate (668 mg, 1.89 mmol), compound **5** (610 mg, 1.89 mmol), and TEA (0.520 mL, 3.77 mmol) were dissolved in THF (60 mL) at room temperature overnight. The reaction solution was concentrated *in vacuo*, then the residue was purified by flash column chromatography on silica gel (Hexane/ethyl acetate = 70/30 to 30/70 as eluent) to yield compound **11** (303 mg, 507 μmol) with a 27% overall yield.

^{1}H NMR (500 MHz, $CDCl_3$): δ 8.07 (d, J = 8.5 Hz, 1H), 7.64 (s, 1H), 7.51 (dd, J = 8.5, 2.0 Hz, 1H), 7.44 (d, J = 2.0 Hz, 1H), 3.89 (s ,2H), 3.71 (t, J = 6.0 Hz, 2H), 3.67-3.62 (m, 18H), 3.38 (t, J = 5.0 Hz, 2H), 2.58 (t, J = 6.0 Hz, 2H), 1.54 (s, 9H). **^{13}C NMR (125 MHz, $CDCl_3$):** δ 152.8, 140.5, 127.6 (q, $^{3}J_{C\text{-}F}$ = 3.8 Hz), 126.3, 125.4 (q, $^{3}J_{C\text{-}F}$ = 3.8 Hz), 124. 8 (q, $^{2}J_{C\text{-}F}$ = 32.5 Hz), 124.1 (q, $^{1}J_{C\text{-}F}$ = 268.8 Hz), 121.3, 81.1, 71.9, 70.7, 70.6, 70.6, 70.6, 70.6, 70.4, 70.0, 50.7, 33.6, 30.4, 28.3. **HRMS (FAB+):** Calcd for $[M+Na]^+$ 619.2384, found 619.2394.

Synthesis of **12**

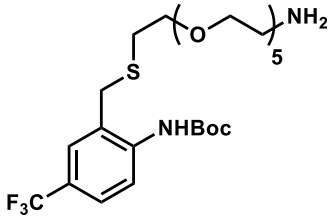

12

Triphenylphosphine (52.8 mg, 201 μmol) and compound **11** (99.4 mg, 168 μmol) were dissolved in THF (5 mL) and the mixture was then heated up to 60 °C for 2 h. After stirring, the solution was cooled at room temperature and water was added to it (500 μL). The resulting solution was stirred at room temperature for 5 h. The reaction solution was concentrated *in vacuo*, then the residue was purified by silica gel column chromatography (DCM/MeOH = 10/1 to MeOH as eluent) to yield compound **12** (73.3 mg, 128 μmol) with a 77% overall yield.

^{1}H NMR (500 MHz; $CDCl_3$): δ 8.07 (d, *J* = 8.5 Hz, 1H), 7.63 (br, 1H), 7.51 (dd, *J* = 8.5, 2.0 Hz, 1H, d), 7.44 (d, *J* = 2.0 Hz, 1H), 3.90 (s, 2H), 3.71 (t, *J* = 6.0 Hz, 2H), 3.67-3.61 (m, 16H), 3.50 (t, *J* = 5.0 Hz, 2H) , 2.85 (t, *J* = 5.0 Hz, 2H), 2.58 (t, *J* = 6.0 Hz, 2H), 1.54 (s, 9H). **^{13}C NMR (125 MHz, $CDCl_3$):** δ 152.8, 140.5, 127.6 (q, $^3J_{C\text{-}F}$ = 3.8 Hz), 126.4, 125.3 (q, $^3J_{C\text{-}F}$ = 3.8 Hz), 124.5 (q, $^2J_{C\text{-}F}$ = 32.5 Hz), 124.1 (q, $^3J_{C\text{-}F}$ = 270.0 Hz), 121.4, 81.1, 72.7, 71.7, 70.6, 70.5, 70.5, 70.3, 70.3, 41.6, 33.6, 30.4, 28.3. **HRMS (ESI+):** Calcd for $[M+H]^+$ 571.2659, found 571.2652.

Synthesis of **PCAF-RB**

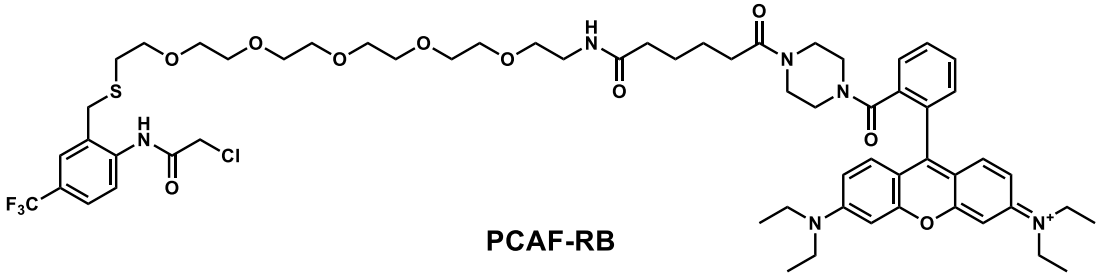

PCAF-RB

DIPEA (6.0 mg, 46 μmol) and compound **8** (10 mg, 16 μmol) were dissolved in DMF (2 mL). HBTU (9.0 mg, 23 μmol) was added to the resulting solution at 0 °C and stirred at 0 °C for 45 min. Compound **12** was added to the reaction mixture (15 mg, 23 μmol) that was warmed to room temperature and stirred overnight. The reaction solution was concentrated *in vacuo*, then 10% TFA in DCM was added to the residue at 0 °C and stirred for 2 h at 0 °C. The reaction solution was concentrated *in vacuo*, and the residue was dissolved in DMF. Chloroacetyl chloride (23 mg, 200 μmol) was added to the reaction

solution at 0 °C and stirred for 1 h at 0 °C. The reaction solution was concentrated *in vacuo*, then the residue was purified by reversed-phase HPLC using ODS-3 column and eluted with H_2O/CH_3CN containing 0.1% TFA to yield the title compound (3.1 mg, 2.7 μmol) with a 12% overall yield.

^{1}H NMR (600 MHz; MeOD-*d*$_4$): δ 7.89 (d, *J* = 7.8 Hz, 1H), 7.78-7.71 (m, 4H), 7.06 (d, *J* = 7.8 Hz, 1H), 7.52 (br, 1H), 7.28 (d, *J* = 9.0 Hz, 2H), 7.07 (dd, *J* = 9.0, 1.8 Hz, 1H), 6.96 (d, *J* = 1.8 Hz, 2H), 4.34 (s, 2H), 3.97 (s, 2H), 3.68 (q, *J* = 7.2 Hz, 8H), 3.66-3.38 (m, 22H), 3.21 (q, *J* = 7.2 Hz, 2H), 2.56 (t, *J* = 6.0 Hz, 2H), 2.35 (t, *J* = 7.2 Hz, 2H), 2.19 (br, 1H), 1.59-1.27 (m, 4H), 1.32-1.29 (m, 12H). **^{13}C NMR (125 MHz, MeOD-*d*$_4$):** δ 175.9, 167.8, 159.3, 157.3, 157.1, 140.3, 136.6, 133.6, 133.3, 131.8, 131.4, 128.9 (q, $^2J_{C\text{-}F}$ = 31.0 Hz), 128.8 (q, $^3J_{C\text{-}F}$ = 3.5 Hz), 126.4, 126.4, 125.9 (q, $^3J_{C\text{-}F}$ = 3.5 Hz), 126.4, 124.4, 123.5 (q, $^1J_{C\text{-}F}$ = 270 Hz), 115.5, 107.5, 97.4, 72.7, 71.6, 71.3, 71.3, 70.6, 48.0, 47.0, 40.4, 36.6, 33.5, 31.8, 25.8, 12.9, 9.3. **HRMS (ESI+):** Calcd for $[M+H]^+$ 1167.5214, found 1167.5267.

Synthesis of **compound <u>13</u>**

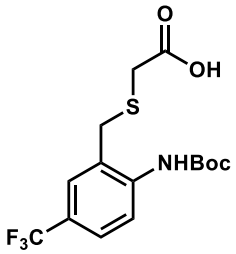

<u>13</u>

tert-Butyl (2-(bromomethyl)-4-(trifluoromethyl)phenyl)carbamate (708 mg, 2.00 mmol) was dissolved in MeOH (4.0 mL) and added to a solution of mercaptoacetic acid (404 mg, 4.40 mmol) in MeOH (10.0 mL). The reaction mixture was stirred at room temperature. Then, a solution of NaOH (160 mg, 4.00 mmol) in MeOH (3.0 mL) was slowly added, and the resulting mixture was stirred at room temperature until benzyl bromide was absent (checked by TLC). The resulting solution was diluted with 2 M NaOH and extracted with DCM/MeOH. The combined organic fractions were washed with brine, dried over Na_2SO_4, and concentrated *in vacuo*. The residue was purified using column chromatography (DCM/MeOH = 95/5 to 50/50 as eluent) to yield the title compound (518 mg, 1.42 mmol) as a colorless oil with a 71% overall yield.

^{1}H NMR (600 MHz, CDCl$_3$): δ 7.90 (s, 1H), 7.51 (d, *J* = 9.0 Hz, 1H), 7.44 (s, 1H), 3.88 (br, 2H), 3.17 (s, 2H), 1.53 (s, 9H) **^{13}C NMR (150 MHz, CDCl$_3$)**: δ 175.7, 153.8, 140.1, 127.5, 125.6, 125.3, 123.9 (q, $^1J_{C\text{-}F}$ = 270 Hz), 122.1, 82.3, 33.2, 32.1, 28.2. **HRMS (ESI-):** Calcd for $[M-H]^-$ 364.0836, found 364.0836.

Synthesis of **PCAF-RBis**

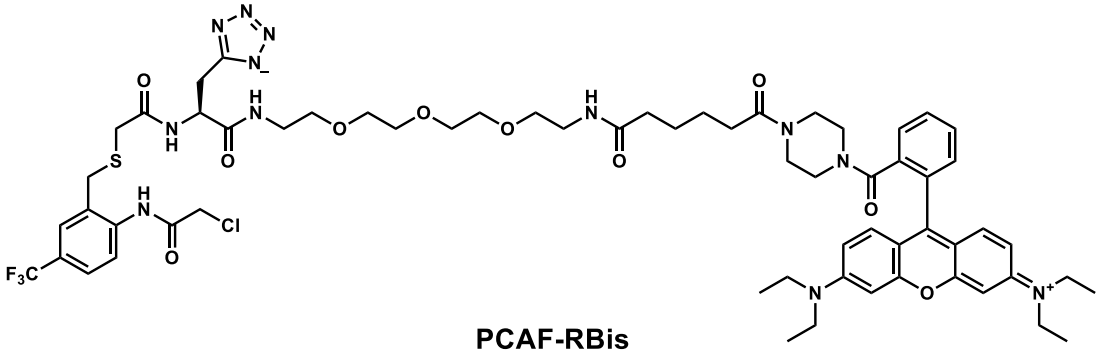

PCAF-RBis

10% Diethyl amine in DMF (5 mL) was added to compound **7** (321 mg, 0.550 mmol) and the mixture was stirred at room temperature overnight. The reaction solution was concentrated *in vacuo*, and the crude product was used for the next step. To a solution of compound **13** (303 mg, 0.830 mmol) we added DIPEA (214 mg, 1.66 mmol) and HBTU (472 mg, 1.24 mmol) in DMF (5 mL) at 0 °C and stirred at 0 °C for 45 min. The crude product was heated to room temperature, added to the reaction mixture, and stirred overnight. The reaction solution was concentrated *in vacuo*, then the residue was purified by column chromatography (H_2O/MeCN containing 0.1% formic acid) to yield the crude product of compound **14** (118 mg) as a colorless oil. A part of the crude product (43 mg) was dissolved in THF/water (2:1, v/v). 1M trimethylphosphine in THF (240 μL, 240 μmol) and KOH (13 mg, 240 μmol) were added to the mixture at 0 °C. The reaction solution was stirred at 0 °C overnight. The reaction solution was concentrated *in vacuo*, and the crude product was separated by silica gel column chromatography (DCM/MeOH = 50/50 to 10/90 as eluent)) for the next coupling reaction. Compound **8** (10 mg, 16 μmol) and DIPEA (6 mg, 46 μmol) were dissolved in DMF (2 mL). HBTU (9 mg, 23 μmol) was added at 0 °C and stirred at 0 °C for 45 min. The reaction mixture was added to a crude Staudinger reaction mixture (crude amino derivative), warmed to room temperature, and stirred overnight. The reaction solution was concentrated *in vacuo*, and the crude product was prepared by reverse phase silica gel column chromatography (H_2O/MeCN containing 0.1% formic acid) for the next step. We added 10% TFA in DCM to the residue at 0 °C and stirred the mixture at 0 °C for 3 h. The reaction solution was concentrated *in vacuo*, and the residue was dissolved in DMF. Chloroacetyl chloride (23 mg, 200 μmol) was added at 0 °C and stirred at 0 °C for 1 h. The reaction solution was concentrated *in vacuo*, and the residue was purified by reverse-phase HPLC using an ODS-3 column and eluted with H_2O/CH_3CN containing 0.1% TFA to yield the title compound (3.8 mg, 2.9 μmol) in 3% yield.

^{1}H NMR (600 MHz; MeOD-*d*$_4$): δ 8.18 (br, 1H), 7.97 (d, *J* = 8.4 Hz, 1H), 7.77-7.69 (m, 4H), 7.58 (d, *J* = 9.0 Hz, 1H), 7.52 (br, 1H), 7.28 (d, *J* = 9.0 Hz, 2H), 7.07 (dd, *J* = 9.0, 1.8 Hz, 1H), 6.96 (d, *J* = 1.8 Hz, 2H), 4.38 (s, 2H), 3.91-3.85 (m, 2H), 3.68 (q, *J* = 7.2 Hz, 8H), 3.66-3.38 (m, 22H), 3.21 (q, *J* = 7.2 Hz, 2H), 3.12 (s, 2H), 2.35 (br, 2H), 2.19 (br, 2H), 1.59-1.57 (m, 4H), 1.32-1.28 (m, 15H). **^{13}C NMR (150 MHz, MeOD-*d*$_4$)**: δ 176.5, 172.5, 172.3, 167.0, 159.4, 157.6, 157.1, 157.0, 136.6, 133.5, 133.2, 132.8, 131.1, 128.9 (q, $^2J_{C\text{-}F}$ = 31.5 Hz), 128.0 (q, $^3J_{C\text{-}F}$ = 3.0 Hz), 126.1, 126.0 (q, $^3J_{C\text{-}F}$ = 3.0 Hz), 124.9, 123.7 (q, $^1J_{C\text{-}F}$ = 280 Hz), 101.4, 71.6, 71.2, 71.2, 71.2, 70.6, 70.4, 61.0, 53.2, 47.0, 44.2, 40.5, 35.0, 33.3, 25.8, 12.9, 9.25. **HRMS (ESI+):** Calcd for $[M+H]^+$ 1275.5398, found 1275.5382.

Synthesis of **PCAF-SPis**

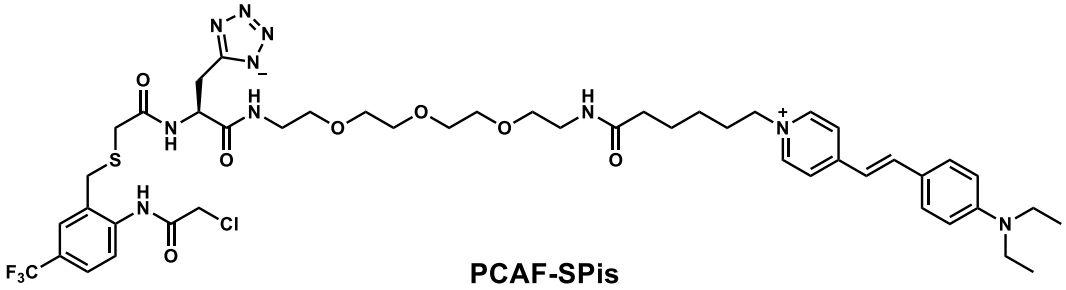

PCAF-SPis

DIPEA (26 mg, 200 μmol) and compound **10** (30 mg, 84 μmol) were dissolved in DMF (5 mL). HBTU (48 mg, 126 μmol) was added to the resulting solution and stirred at 0 °C for 45 min. The crude product **15** was added to the reaction mixture, warmed to room temperature, and stirred overnight. The reaction solution was concentrated *in vacuo*. Then, we added 10% TFA in DCM to the residue and stirred it for 2 h at room temperature. The reaction solution was concentrated *in vacuo*, then the residue was dried for several hours, and dissolved in DMF. Chloroacetyl chloride (23 mg, 200 μmol) was added to the solution that was stirred for 1 h at 0 °C. The reaction solution was concentrated *in vacuo*, then the residue was purified by reverse-phase HPLC using ODS-3 column and eluted with H_2O/CH_3CN containing 0.1% TFA to yield the title compound (3.1 mg, 2.7 μmol) with a 12% overall yield.

^{1}H NMR (600 MHz, DMSO-*d*$_6$): δ 9.95 (br, 1H), 8.73 (d, *J*= 6.6 Hz, 2H), 8.53 (d, *J*= 7.2 Hz, 1H), 8.16 (t, *J*= 5.4 Hz, 1H), 8.04 (d, *J*= 7.2 Hz, 2H), 7.95 (d, *J*= 9.0 Hz, 1H), 7.90 (d, *J*= 16.8 Hz, 1H), 7.84 (t, *J*= 5.4 Hz, 1H), 7.71 (d, *J*= 1.8 Hz, 1H), 7.65 (dd, *J*= 9.0, 1.8 Hz, 1H), 7.56 (d, *J*= 9.0 Hz, 2H), 7.12 (d, *J*= 16.8 Hz, 1H), 6.75 (d, *J*= 9.0 Hz, 2H), 4.76-4.72 (m, 1H), 4.41 (s, 2H), 4.39 (t, *J*= 7.2 Hz, 2H), 3.90 (d, *J*= 14.4 Hz, 1H), 3.84 (d, 14.4 Hz, 1H), 3.49-3.15 (m, 22H), 3.11 (s, 2H), 2.07 (t, *J*= 6.6 Hz, 2H), 1.91-

1.84 (m, 2H), 1.55-1.50 (m, 2H), 1.26-1.20 (m, 2H), 1.13 (t, *J*= 7.2 Hz, 1H). **^{13}C NMR (150 MHz, MeOD-*d*$_4$)**: δ 175.8, 172.2, 171.1, 170.9, 168.2, 156.3, 144.4, 140.6, 132.1, 132.0, 128.8 (q, $^3J_{C\text{-}F}$ = 3.0 Hz), 128.5 (q, $^2J_{C\text{-}F}$ = 30.0 Hz), 126.1, 126.0, 124.8 (q, $^1J_{C\text{-}F}$ = 277 Hz), 101.39, 71.6, 71.2, 70.6, 70.4, 61.0, 53.2, 44.2, 41.8, 40.6, 40.3, 36.5, 35.0, 33.2, 31.8, 27.3, 26.6, 26.1, 12.7. **HRMS (ESI+):** Calcd for $[M]^+$ 1003.4237, found 1003.4215.

Reaction condition screening of **PCAF-Me**

Entry 1,2

After the completely proceeding of Boc deprotection was confirmed by TLC monitoring, the acylating reaction of the aniline derivative was tried to conducted in corresponding conditions. As a result of the 1H-NMR spectra in the crudes, ^{1}H-NMR peaks of the objecting compound were not observed.

Entry 3

The solution of tert-butyl (2-methyl-4-(trifluoromethyl)phenyl)carbamate (100 mg, 0.364 mmol) in DCM (10 mL) was added to TFA (0.6 mL) and stirred at room temperature until the aniline disappeared. After the mixture was concentrated under reduced pressure, then the result was resolved in DMF (2 mL) to prepare as a reaction solution for next acylation. Chloroacetic acid (69 mg, 0.73 mmol) was added to 1.7M T3P in ethyl acetate (1.45 mmol), HOBt (196 mg, 1.45 mmol), DIPEA (0.316 mL, 1.82 mmol) and DMF (1 mL), and then stirred at 0 °C for 1 h; the reaction mixture was added to the reaction solution with aniline derivative, then warmed to room temperature and stirred at room temperature overnight. The solution was concentrated in vacuo, then the resultant was purified by silica gel column chromatography (Hexane/AcOEt = 10/1 to 1/1 as eluent) to **PCAF-Me** (26 mg, 0.105 mmol) with a 29% yield.

Entry 4

The solution of tert-butyl (2-methyl-4-(trifluoromethyl)phenyl)carbamate (20 mg, 0.073 mmol) in DCM (1.8 mL) was added to TFA (0.2 mL) and stirred at room temperature until the aniline disappeared. After the mixture was concentrated under reduced pressure, the result was resolved in DMF (1mL), then added to 1M DIPEA in DMF (0.11 mL, 0.11

mmol) and Chloroacetyl chloride (12 mg, 0.11 mmol) at 0 °C and stirred at 0 °C for 2 h. The solution was concentrated in vacuo, then the resultant was purified by silica gel column chromatography (Hexane/AcOEt = 10/1 to 1/1 as eluent) to PCAF-Me (16 mg, 0.064 mmol) with an 88% yield.

^{1}H NMR (600 MHz, MeOD-*d*$_4$): δ 7.70 (d, J = 8.4 Hz, 1H), 7.55 (s, 1H), 7.50 (d, J = 8.4 Hz, 1H), 4.28 (s, 2H), 2.35 (s, 3H). **^{13}C NMR (150 MHz, MeOD-*d*$_4$)**: δ 168.0, 140.1, 134.4, 129.1 (q, $^{2}J_{C\text{-}F}$ = 31.5 Hz), 128.5 (q, $^{3}J_{C\text{-}F}$ = 3.0 Hz), 126.3, 126.0 (q, $^{1}J_{C\text{-}F}$ = 270 Hz), 124.4 (q, $^{3}J_{C\text{-}F}$ = 3.0 Hz), 43.7, 17.9.

2.4.3 Biological experiment procedures

2.4.3.1 Plasmid construction

pcDNA3.1(+)-MBP-PYP^{WT}

Plasmid construction was performed as previously described.[44]

pcDNA3.1(+)-PYP^{WT}-EGFR

Plasmid construction was performed as previously described.[45]

pcDNA3.1(+)-HA-PYP^{WT}-NLS

Plasmid construction was performed as previously described.[30]

pcDNA3.1(+)-HA-PYP^{NQN}-NLS

Plasmid construction was performed as previously described.[28]

pcDNA3.1(+)-HA-Halo-NLS

Plasmid construction was performed as previously described.[28]

2.4.3.2 Preparation of recombinant proteins (PYP-tag)

Escherichia coli cells [BL21 (DE3) (Novagen)] transformed with plasmids encoding PYP-tag (PYP^{WT}, PYP^{NQN}) were cultivated in Luria-Bertani medium containing 100 μg/mL of ampicillin at 37 °C until the OD_{600} value of the culture medium reached 0.6–0.8. At this point, the temperature was lowered to 20 °C with the addition of IPTG (Isopropyl β-D-1-thiogalactopyranoside). Then, overnight protein expression was induced overnight to afford a final protein concentration of 100 μM. The cells were harvested by centrifugation at 5,000 rpm for 15 min, resuspended in binding buffer (50 mM sodium phosphate, 300 mM NaCl, 1 mM DTT, pH 8.0), and lysed by sonication. The cell lysate supernatant was obtained by centrifugation at 15,000 rpm for 20 min and passed through a Ni column (Roche). The resin was washed with a wash buffer (50 mM sodium phosphate, 300 mM NaCl, 5 mM imidazole, and 1 mM DTT; pH 8.0) and eluted with a second buffer (50 mM sodium phosphate, 300 mM NaCl, 250 mM imidazole, and 1 mM DTT; pH 8.0) in accordance with the manufacturer's protocol. The eluted fraction was further purified through size exclusion chromatography (SuperdexTM 75 10/300 GL, GE Healthcare) using a running buffer (20 mM HEPES and 150 mM NaCl; pH 7.4) and the purity and molecular weight of proteins were assessed by SDS-PAGE. The purified protein was dissolved in the assay buffer (20 mM HEPES and 150 mM NaCl; pH 7.4)

and then flash-frozen with liquid nitrogen for storage at –80 °C.

2.4.3.3 Protein labeling reactions for SDS-PAGE analysis

PYP-tag (1.0 μM) and the probes (2.0 μM) were incubated in the assay buffer (20 mM HEPES, pH 7.4, containing 150 mM NaCl) at 37 °C for 30 min. The reaction was then quenched with *N*-ethylmaleimide (f.c. 25 mM) at room temperature for 5 min. The reaction solutions were heated at 103 °C for 5 min and subsequently analyzed by sodium dodecyl sulfate-polyacrylamide gel electrophoresis. Fluorescence images were obtained using Gel mie-ru mini470 (Wako Pure Chemical Industries). The gel was stained with Coomassie Brilliant Blue. The excitation wavelength used for fluorescence imaging was 470 nm.

2.4.3.4 Absorption spectroscopy

Absorption spectra were measured after the probe (5.0 μM) was incubated with or without PYP-tag (10 μM) in the assay buffer (20 mM HEPES, pH 7.4, containing 150 mM NaCl) at 37 °C for 30 min.

2.4.3.5 Fluorescence spectroscopy

Fluorescence spectra were measured after the probe (5.0 μM) was incubated with or without PYP-tag (10 μM) in the assay buffer at 37 °C for 30 min. The fluorescence spectra of the mixtures were recorded at an excitation wavelength of 484 nm (**PCAF-SP**, **PCAF-SPis**, and **PCAF-SP-s**) or 535 nm (**PCAF-RB** and **PCAF-RBis**), with a slit width of 5.0 nm for both excitation and emission. Relative fluorescence quantum yields were determined using fluorescein in 0.1 M NaOH aq. (Ex: 470 nm, Φ_{fl} = 91%)[46] and Rhodamine B in water (Ex: 535 nm, Φ_{fl} = 36%)[47] as a reference.

2.4.3.6 Kinetic analyses of protein labeling reactions

The fluorescence half-life $t_{1/2}$ and second-order rate constant k_2 of the labeling reaction of each probe were obtained from time-course experiments. Each probe (1.0 μM) was reacted with PYP-tag (2.0 μM) in the assay buffer (20 mM HEPES, pH 7.4, containing 150 mM NaCl) at 37 °C and the fluorescence intensity was monitored with the slit width of 5.0 nm. The fluorescence half-lives and second-order rate constants were calculated using the following equations:

$$F_t = ((\exp(k_2\, t_{1/2}([A]_0 - [B]_0)) - 1) / (\exp(k_2\, t_{1/2}([A]_0 - [B]_0)) - [B]_0 / [A]_0))\,(F_{max} - F_0) + F_0$$

Equation 1

$[A]_0$ and $[B]_0$ represent the initial concentrations of [PYP-tag] and [Probe], respectively. F_t and F_0 represent the observed fluorescence intensity at time t and at the initial point, respectively. F_{max} was determined using the Equation 1.

2.4.3.7 Cell cultures

HEK293T cells were purchased from RIKEN BRC. HEK293T cells were cultured in DMEM containing 10% fetal bovine serum and PS as antibiotics (100 U/mL penicillin and 0.1 mg/mL streptomycin). Transfected cells were maintained in a 5% CO_2 atmosphere at 37 °C throughout the experiments.

2.4.3.8 Fluorescence imaging of proteins in live cells using PCAF-RB and PCAF-RBis

HEK293T cells were transfected with pcDNA3.1(+)-PYP^{NQN}-NLS using Lipofectamine 3000 (Invitrogen), according to the manufacturer's protocol. After incubating the transfected cells in 5% CO_2 at 37 °C for 24 h, the cells were washed with HBSS buffer three times. Then, the cells were incubated with 5.0 μM probe in DMEM for 30 min. The cells were incubated for an additional 10 min after replacing the medium with DMEM. Cell images were acquired with a cell washing step (three times with HBSS buffer) using a confocal laser scanning microscope. All images were captured at an excitation frequency of 561 nm with an emission range of 566–685 nm using a 63× lens (Zeiss LSM 880).

2.4.3.9 Localization analysis of PCAF-RB in live cells using MitoTracker Green FM

HEK293T cells were washed thrice with HBSS buffer. The cells were incubated with 100 nM **PCAF-RB** and 100 nM MitoTracker Green FM in DMEM for 60 min. Cell images were acquired using a washing step (three times with HBSS buffer). All images were captured at excitation frequencies of 470/40 nm and 560/40 nm with emission ranges of 525/50 and 560/40 nm, respectively, using a 60× lens (Keyence BZ-X710).

2.4.3.10 Fluorescence imaging of proteins in live cells using PCAF-SP and PCAF-SPis

HEK293T cells were transfected with pcDNA3.1(+)-PYP^{WT}-NLS using Lipofectamine 3000 (Invitrogen), according to the manufacturer's protocol. After incubation of the transfected cells in 5% CO_2 at 37 °C for 24 h, the cells were washed with HBSS buffer three times. Then, the cells were incubated with 1.25 μM probe in DMEM for 60 min. Cell images were acquired without the cell washing step using a confocal laser scanning microscope. All images were captured at an excitation frequency of 488 nm and an emission range of 550–650 nm using a 63× lens (Zeiss LSM 880).

2.4.3.11 Fluorescence imaging of proteins in live cells using PCAF-SP-s and PCAFred

HEK293T cells were transfected with pcDNA3.1(+)-PYP^{WT}-NLS and PYP^{WT}-EGFR or empty vector using Lipofectamine 3000 (Invitrogen), according to the manufacturer's protocol. After incubation of the transfected cells in 5% CO_2 at 37 °C for 24 h, the cells were washed with HBSS buffer three times. Then, the cells were incubated with 1.0 μM **PCAF-SP-s** and 1.0 μM **PCAFred** in DMEM for 30 min. Cell images were acquired without the cell washing step using a confocal laser scanning microscope. All images were obtained with excitation at 488 nm and 633 nm by detecting 500-600 (green) and 660–710 (magenta) nm emissions, respectively, using a 63× lens (Zeiss LSM 880).

2.4.3.12 Comparative labeling efficiency of PYP-tag with PCAF-SP and PCAF-SPis

HEK293T cells were transfected with pcDNA3.1(+)-PYP^{WT}-NLS using Lipofectamine 3000 (Invitrogen) according to the manufacturer's protocol. After incubation of the cells at 37 °C for 24 h, the cells were washed with HBSS three times. The cells were incubated with 10 mM probes in DMEM for 4 h, respectively. After the incubation, the cells were centrifuged at 500 g for 5 min at 4 °C and removed the supernatant. The resultant cells were lysed in the lysis buffer (20 mM Tris-HCl pH 7.5, 150 mM NaCl, 5 mM EDTA, 1% (v/v) Triton X-100) on ice for 15 min. The cell lysate was centrifuged at 15000 g for 15 min at 4 °C. The HA-PYP fusion protein was isolated from the supernatant using the HA-tagged Protein Purification Kit (Medical & Biological Laboratories Co., Ltd.) according to the manufacturer's protocol. The sample was heated at 95 °C for 5 min and subsequently analyzed by SDS–PAGE. Fluorescence images were obtained using Gel mie-ru mini470 (Wako Pure Chemical Industries). The gel was stained with Coomassie Brilliant Blue. The excitation wavelength used for fluorescence imaging was 470 nm.

2.5 Reference

1. Lavis, L. D.; Raines, R. T. Bright Ideas for Chemical Biology. *ACS Chem. Biol.* **2008**, *3* (3), 142–155.
2. Dempsey, G. T.; Vaughan, J. C.; Chen, K. H.; Bates, M.; Zhuang, X. Evaluation of Fluorophores for Optimal Performance in Localization-Based Super-Resolution Imaging. *Nat. Methods* **2011**, *8* (12), 1027–1036.
3. Heilemann, M.; van de Linde, S.; Mukherjee, A.; Sauer, M. Super-Resolution Imaging with Small Organic Fluorophores. *Angew. Chem. Int. Ed.* **2009**, *48* (37), 6903–6908.
4. Wang, L.; Du, W.; Hu, Z.; Uvdal, K.; Li, L.; Huang, W. Hybrid Rhodamine Fluorophores in the Visible/NIR Region for Biological Imaging. *Angew. Chem. Int. Ed.* **2019**, *58* (40), 14026–14043.
5. Clark, S. A.; Singh, V.; Vega Mendoza, D.; Margolin, W.; Kool, E. T. Light-Up "Channel Dyes" for Haloalkane-Based Protein Labeling in Vitro and in Bacterial Cells. *Bioconjugate Chem.* **2016**, *27* (12), 2839–2843.
6. Miró-Vinyals, C.; Stein, A.; Fischer, S.; Ward, T. R.; Deliz Liang, A. HaloTag Engineering for Enhanced Fluorogenicity and Kinetics with a Styrylpyridium Dye. *ChemBioChem* **2021**, *22* (24), 3398–3401.
7. Yang, Q.; Wang, S.; Li, D.; Yuan, J.; Xu, J.; Shao, S. A Mitochondria-Targeting Nitroreductase Fluorescent Probe with Large Stokes Shift and Long-Wavelength Emission for Imaging Hypoxic Status in Tumor Cells. *Analytica Chimica Acta* **2020**, *1103*, 202–211.
8. Xu, W.; Zeng, Z.; Jiang, J.-H.; Chang, Y.-T.; Yuan, L. Discerning the Chemistry in Individual Organelles with Small-Molecule Fluorescent Probes. *Angew. Chem. Int. Ed.* **2016**, *55* (44), 13658–13699.
9. Nguyen, T.; Francis, M. B. Practical Synthetic Route to Functionalized Rhodamine Dyes. *Org. Lett.* **2003**, *5* (18), 3245–3248.
10. Su, D.; Teoh, C. L.; Park, S.-J.; Kim, J.-J.; Samanta, A.; Bi, R.; Dinish, U. S.; Olivo, M.; Piantino, M.; Louis, F.; Matsusaki, M.; Kim, S. S.; Bae, M. A.; Chang, Y.-T. Seeing Elastin: A Near-Infrared Zwitterionic Fluorescent Probe for *In Vivo* Elastin Imaging. *Chem* **2018**, *4* (5), 1128–1138.
11. Su, D.; Teoh, C. L.; Samanta, A.; Kang, N.-Y.; Park, S.-J.; Chang, Y.-T. The Development of a Highly Photostable and Chemically Stable Zwitterionic Near-Infrared Dye for Imaging Applications. *Chem. Commun.* **2015**, *51* (19), 3989–3992.

12. Wang, L.; Du, W.; Hu, Z.; Uvdal, K.; Li, L.; Huang, W. Hybrid Rhodamine Fluorophores in the Visible/NIR Region for Biological Imaging. *Angew. Chem. Int. Ed.* **2019**, *58* (40), 14026–14043.
13. Collot, M.; Boutant, E.; Fam, K. T.; Danglot, L.; Klymchenko, A. S. Molecular Tuning of Styryl Dyes Leads to Versatile and Efficient Plasma Membrane Probes for Cell and Tissue Imaging. *Bioconjugate Chem.* **2020**, *31* (3), 875–883.
14. Birke, R.; Ast, J.; A. Roosen, D.; Lee, J.; Roßmann, K.; Huhn, C.; Mathes, B.; Lisurek, M.; Bushiri, D.; Sun, H.; Jones, B.; Lehmann, M.; Levitz, J.; Haucke, V.; J. Hodson, D.; Broichhagen, J. Sulfonated Red and Far-Red Rhodamines to Visualize SNAP- and Halo-Tagged Cell Surface Proteins. *Org. Biomol. Chem.* **2022**, *20* (30), 5967–5980.
15. Hanaoka, K.; Iwaki, S.; Yagi, K.; Myochin, T.; Ikeno, T.; Ohno, H.; Sasaki, E.; Komatsu, T.; Ueno, T.; Uchigashima, M.; Mikuni, T.; Tainaka, K.; Tahara, S.; Takeuchi, S.; Tahara, T.; Uchiyama, M.; Nagano, T.; Urano, Y. General Design Strategy to Precisely Control the Emission of Fluorophores via a Twisted Intramolecular Charge Transfer (TICT) Process. *J. Am. Chem. Soc.* **2022**, *144* (43), 19778–19790.
16. Ast, J.; Nasteska, D.; Fine, N. H. F.; Nieves, D. J.; Koszegi, Z.; Lanoiselée, Y.; Cuozzo, F.; Viloria, K.; Bacon, A.; Luu, N. T.; Newsome, P. N.; Calebiro, D.; Owen, D. M.; Broichhagen, J.; Hodson, D. J. Revealing the Tissue-Level Complexity of Endogenous Glucagon-like Peptide-1 Receptor Expression and Signaling. *Nat. Commun* **2023**, *14* (1), 301.
17. Komatsu, T.; Johnsson, K.; Okuno, H.; Bito, H.; Inoue, T.; Nagano, T.; Urano, Y. Real-Time Measurements of Protein Dynamics Using Fluorescence Activation-Coupled Protein Labeling Method. *J. Am. Chem. Soc.* **2011**, *133* (17), 6745–6751.
18. Hori, Y.; Hirayama, S.; Kikuchi, K. Development of Cyanine Probes with Dinitrobenzene Quencher for Rapid Fluorogenic Protein Labelling. *Philos. Transact. A Math. Phys. Eng. Sci.* **2017**, *375* (2107), 20170018.
19. Hirayama, S.; Hori, Y.; Benedek, Z.; Suzuki, T.; Kikuchi, K. Fluorogenic Probes Reveal a Role of GLUT4 N-Glycosylation in Intracellular Trafficking. *Nat. Chem. Biol.*, **2016**, ***12***, 853–859.
20. Nishiura, M.; Hori, Y.; Umeno, M.; Kikuchi, K. Visualization of Multiple Localizations of GLUT4 by Fluorescent Probes of PYP-Tag with Designed Unnatural Warhead. *Chem. Sci.* **2023**, *14* (22), 5925–5935.
21. Turnbull, J. L.; Benlian, B. R.; Golden, R. P.; Miller, E. W. Phosphonofluoresceins: Synthesis, Spectroscopy, and Applications. *J. Am. Chem. Soc.* **2021**, *143* (16), 6194–

6201.

22. Turnbull, J. L.; Golden, R. P.; Benlian, B. R.; Henn, K. M.; Lipman, S. M.; Miller, E. W. Mild and Scalable Synthesis of Phosphonorhodamines. *Chem. Sci.* **2023**, *14* (41), 11365–11373.
23. Sensi, S. L.; Ton-That, D.; Weiss, J. H.; Rothe, A.; Gee, K. R. A New Mitochondrial Fluorescent Zinc Sensor. *Cell Calcium* **2003**, *34* (3), 281–284.
24. Sensi, S. L.; Ton-That, D.; Sullivan, P. G.; Jonas, E. A.; Gee, K. R.; Kaczmarek, L. K.; Weiss, J. H. Modulation of Mitochondrial Function by Endogenous Zn^{2+} Pools. *Proc. Natl. Acad. Sci.* **2003**, *100* (10), 6157–6162.
25. Egawa, T.; Hirabayashi, K.; Koide, Y.; Kobayashi, C.; Takahashi, N.; Mineno, T.; Terai, T.; Ueno, T.; Komatsu, T.; Ikegaya, Y.; Matsuki, N.; Nagano, T.; Hanaoka, K. Red Fluorescent Probe for Monitoring the Dynamics of Cytoplasmic Calcium Ions. *Angew. Chem. Int. Ed.* **2013**, *52* (14), 3874–3877.
26. Kamikawa, Y.; Hori, Y.; Yamashita, K.; Jin, L.; Hirayama, S.; Standley, D. M.; Kikuchi, K. Design of a Protein Tag and Fluorogenic Probe with Modular Structure for Live-Cell Imaging of Intracellular Proteins. *Chem. Sci.* **2015**, *7* (1), 308–314.
27. Minta, A.; Kao, J. P. Y.; Tsien, R. Y. Fluorescent Indicators for Cytosolic Calcium Based on Rhodamine and Fluorescein Chromophores. *J. Biol. Chem.* **1989**, *264* (14), 8171–8178.
28. Reja, S. I.; Hori, Y.; Kamikawa, T.; Yamasaki, K.; Nishiura, M.; Bull, S. D.; Kikuchi, K. An "OFF–ON–OFF" Fluorescence Protein-Labeling Probe for Real-Time Visualization of the Degradation of Short-Lived Proteins in Cellular Systems. *Chem. Sci.* **2022**, *13* (5), 1419–1427.
29. Wang, L. G.; Montaño, A. R.; Combs, J. R.; McMahon, N. P.; Solanki, A.; Gomes, M. M.; Tao, K.; Bisson, W. H.; Szafran, D. A.; Samkoe, K. S.; Tichauer, K. M.; Gibbs, S. L. OregonFluor Enables Quantitative Intracellular Paired Agent Imaging to Assess Drug Target Availability in Live Cells and Tissues. *Nat. Chem.* **2023**, *15* (5), 729–739.
30. Hori, Y.; Norinobu, T.; Sato, M.; Arita, K.; Shirakawa, M.; Kikuchi, K. Development of Fluorogenic Probes for Quick No-Wash Live-Cell Imaging of Intracellular Proteins. *J. Am. Chem. Soc.* **2013**, *135* (33), 12360–12365.
31. Hori, Y.; Otomura, N.; Nishida, A.; Nishiura, M.; Umeno, M.; Suetake, I.; Kikuchi, K. Synthetic-Molecule/Protein Hybrid Probe with Fluorogenic Switch for Live-Cell Imaging of DNA Methylation. *J. Am. Chem. Soc.* **2018**, *140* (5), 1686–1690.
32. Liu, T.-K.; Hsieh, P.-Y.; Zhuang, Y.-D.; Hsia, C.-Y.; Huang, C.-L.; Lai, H.-P.; Lin, H.-S.; Chen, I.-C.; Hsu, H.-Y.; Tan, K.-T. A Rapid SNAP-Tag Fluorogenic Probe

Based on an Environment-Sensitive Fluorophore for No-Wash Live Cell Imaging. *ACS Chem. Biol.* **2014**, *9* (10), 2359–2365.

33. Nadler, A.; Schultz, C. The Power of Fluorogenic Probes. *Angew. Chem. Int. Ed.* **2013**, *52* (9), 2408–2410.
34. Wang, L.; Tran, M.; D'Este, E.; Roberti, J.; Koch, B.; Xue, L.; Johnsson, K. A General Strategy to Develop Cell Permeable and Fluorogenic Probes for Multicolour Nanoscopy. *Nat. Chem.* **2020**, *12* (2), 165–172.
35. Lukinavičius, G.; Umezawa, K.; Olivier, N.; Honigmann, A.; Yang, G.; Plass, T.; Mueller, V.; Reymond, L.; Corrêa Jr, I. R.; Luo, Z.-G.; Schultz, C.; Lemke, E. A.; Heppenstall, P.; Eggeling, C.; Manley, S.; Johnsson, K. A Near-Infrared Fluorophore for Live-Cell Super-Resolution Microscopy of Cellular Proteins. *Nat. Chem.* **2013**, *5* (2), 132–139.
36. Thornber, C. W. Isosterism and Molecular Modification in Drug Design. *Chem. Soc. Rev.* **1979**, *8* (4), 563.
37. Patani, G. A.; LaVoie, E. J. Bioisosterism: A Rational Approach in Drug Design. *Chem. Rev.* **1996**, *96* (8), 3147–3176.
38. Meanwell, N. A. Synopsis of Some Recent Tactical Application of Bioisosteres in Drug Design. *J. Med. Chem.* **2011**, *54* (8), 2529–2591.
39. Lassalas, P.; Gay, B.; Lasfargeas, C.; James, M. J.; Tran, V.; Vijayendran, K. G.; Brunden, K. R.; Kozlowski, M. C.; Thomas, C. J.; Smith, A. B. I.; Huryn, D. M.; Ballatore, C. Structure Property Relationships of Carboxylic Acid Isosteres. *J. Med. Chem.* **2016**, *59* (7), 3183–3203.
40. Strehmel, B.; Seifert, H.; Rettig, W. Photophysical Properties of Fluorescence Probes. 2. A Model of Multiple Fluorescence for Stilbazolium Dyes Studied by Global Analysis and Quantum Chemical Calculations. *J. Phys. Chem. B* **1997**, *101* (12), 2232–2243.
41. Huang, Y.; Cheng, T.; Li, F.; Luo, C.; Huang, C.-H.; Cai, Z.; Zeng, X.; Zhou, J. Photophysical Studies on the Mono- and Dichromophoric Hemicyanine Dyes II. Solvent Effects and Dynamic Fluorescence Spectra Study in Chloroform and in LB Films. *J. Phys. Chem. B* **2002**, *106* (39), 10031–10040.
42. Sasaki, S.; Drummen, G. P. C.; Konishi, G. Recent Advances in Twisted Intramolecular Charge Transfer (TICT) Fluorescence and Related Phenomena in Materials Chemistry. *J. Mater. Chem. C* **2016**, *4* (14), 2731–2743.
43. Cao, X.; Tolbert, R. W.; McHale, J. L.; Edwards, W. D. Theoretical Study of Solvent Effects on the Intramolecular Charge Transfer of a Hemicyanine Dye. *J. Phys. Chem. A* **1998**, *102* (17), 2739–2748.

44. Hori, Y.; Ueno, H.; Mizukami, S.; Kikuchi, K. Photoactive Yellow Protein-Based Protein Labeling System with Turn-On Fluorescence Intensity. *J. Am. Chem. Soc.* **2009**, *131* (46), 16610–16611.
45. Hori, Y.; Nakaki, K.; Sato, M.; Mizukami, S.; Kikuchi, K. Development of Protein-Labeling Probes with a Redesigned Fluorogenic Switch Based on Intramolecular Association for No-Wash Live-Cell Imaging. *Angew. Chem. Int. Ed.* **2012**, *51* (23), 5611–5614.
46. Brouwer, A. M. Standards for Photoluminescence Quantum Yield Measurements in Solution (IUPAC Technical Report). *Pure Appl. Chem.* **2011**, *83* (12), 2213–2228.
47. Zhang, X.-F.; Zhang, Y.; Liu, L. Fluorescence Lifetimes and Quantum Yields of Ten Rhodamine Derivatives: Structural Effect on Emission Mechanism in Different Solvents. *Journal of Luminescence* **2014**, *145*, 448–453.

Chapter 3. Multicolor imaging for visualized multiple localizations of GLUT4 using PYP-tag labeling probes

3.1. Introduction

3.1.1. GLUT4

GLUT4 is a type of glucose transporter and a 12-transmembrane protein expressed mainly in the muscle and adipose tissues.[1-3] In addition, GLUT4 plays a role in adjusting blood glucose concentration, by mediating the cellular uptake of glucose in response to insulin stimulation.[1-3] Dysfunction in this regulatory mechanism is a key factor in type 2 diabetes.[2-4] Consequently, elucidating the regulatory mechanism, which is involved in GLUT4 dynamics, is important in biological and medical studies.

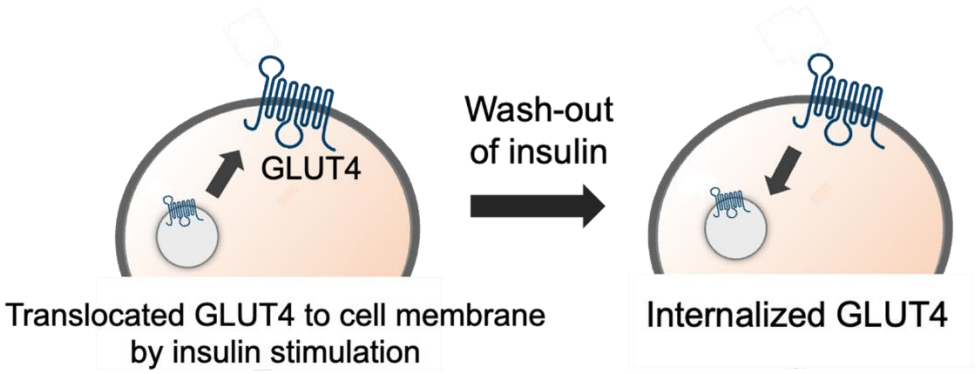

Figure 3-1. GLUT4 dynamics with insulin stimulation.

3.1.2. GLUT4 multiple localizations

Multiple localizations are observed in several proteins, including p53, EGFR, vascular endothelial growth factor receptor, nuclear factor-κB, the heat shock protein (HSP)70 family (excluding HSP70-5 and HSP70-9), mucin 1 C-terminal, β-catenin, E-cadherin, mineralocorticoid receptor, and glucocorticoid receptor. In oncoproteins, multiple localizations can also be caused by DNA mutations, transport processes promoted by protein–protein interactions, oxidative stress, and the loss or recovery of NLS function.[5,6] In addition, some proteins classified as transmembrane proteins and receptors show multiple localizations in various biological events. For example, the localization of glycoproteins is affected by quality control in the ER through *N*-glycosylation and glycan degradation.[7] In glycoprotein quality control in the ER, concerted actions of ER-localized chaperones, enzymes, and lectins play critical roles in distinguishing misfolded or unfolded forms of these proteins and transporting misfolded proteins outside the ER.[7] After misfolded glycoproteins are transported, the proteins are degraded through pathways such as ER-associated degradation[7,8] and ER-to-lysosome-associated degradation.[9,10]

GLUT4 dynamically translocates to the cell membrane upon insulin stimulation[7,11] and exhibits multiple localizations in cytoplasmic regions (*e.g.*, lysosomes, ER and Golgi apparatus),[12] which are caused by localization changes associated with various biological events. In previous studies, dual-color imaging of GLUT4 was achieved by the labeling of membrane-permeable and impermeable probes.[11,12] The membrane-permeable probe can selectively label intracellular GLUT4, while the membrane-impermeable probe can selectively label GLUT4 that is localized on the cell membrane.[11,12] Based on these backgrounds, the probes developed in the chapter 2 were applied for imaging of GLUT4 multiple localization to demonstrate the versatility of tetrazole-conjugated and sulfonate-conjugated probes, since the labeling specificity of these probes can be confirmed with the imaging study of membrane-localized and intracellular-localized GLUT4.

In this chapter, the author demonstrated that **PCAF-RBis** and **PCAF-SP-s** can be applied to visualize multiple localizations of GLUT4 without off-target labeling.

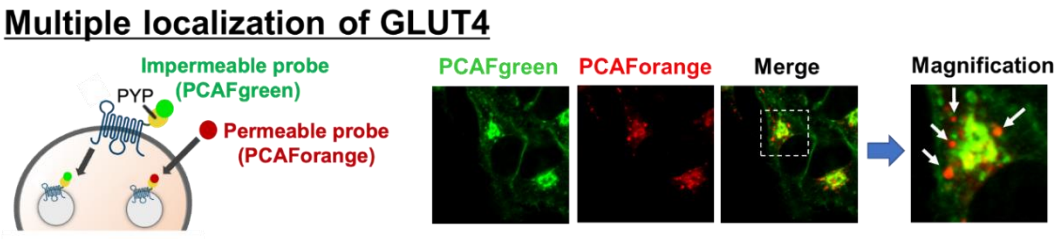

Figure 3-2. GLUT4 multiple localization.

3.2. Results and discussion

3.2.1. Intracellular GLUT4 imaging

PCAF-RBis was employed for the visualization of intracellular GLUT4. According to the protocol described in previous reports[11,12] for intracellular GLUT4 imaging, HeLa cells stably expressing PYP^{WT}-GLUT4 were incubated with the starvation medium. Then, the cells were incubated with **PCAF-RBis** for 30 min without insulin. As a result, fluorescent signals were observed in the cytoplasm, indicating that **PCAF-RBis** could label intracellular GLUT4 (Figure 3-3). Additionally, a control experiment in HeLa cells that do not express PYP-tag was performed under the same conditions. As a result of a control experiment, fluorescence signals were not observed, indicating that **PCAF-RBis** could label intracellular GLUT4 without undesired signals.

Moreover, dual-color imaging was conducted using both **PCAF-RBis** labeling and immunostaining in HeLa cells expressing PYP^{WT}-GLUT4 (Figure 3-4). According to a

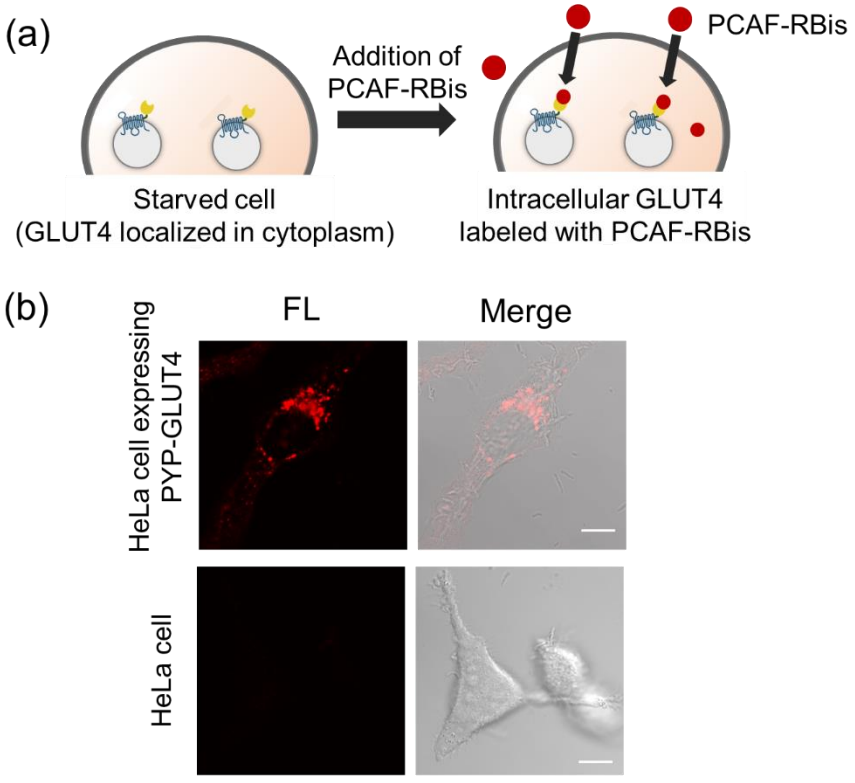

Figure 3-3. (a) Schematic view intracellular GLUT4 imaging with **PCAF-RBis**. (b) Fluorescence images and merged images with a phase contrast image of HeLa cells stably expressing PYP^{WT}-GLUT4 or HeLa cells (non-expressed PYP-tag) stained stained with **PCAF-RB** (1.25 μM) in the absence of insulin. The image obtained with the excitation at 561 nm by detecting 635–705 (red) nm emission. Scale bars, 10 μm. The experiment was performed twice with similar results.

previous report, PYP^{WT}-GLUT4 in stably expressing cells can be visualized by immunostaining using an anti-FLAG antibody, since the protein is fused with a FLAG-tag. Consequently, localization analysis of GLUT4 was conducted using both **PCAF-RBis** labeling and immunostaining with antibodies. In this study, an anti-FLAG mouse antibody as the primary antibody and an Alexa Fluor 647-conjugated anti-mouse antibody as the secondary antibody were employed. As a result of the dual-color imaging, fluorescence signals were observed in the emission channels corresponding to **PCAF-RBis** (orange) and immunostaining (magenta). Additionally, the signals of GLUT4 labeled with **PCAF-RBis** overlapped with those of Alexa Fluor 647. In contrast, fluorescence signals were not observed in control experiments using HeLa cells. This result is consistent with the results of live-cell GLUT4 imaging. These results demonstrate that **PCAF-RBis** can specifically label intracellular GLUT4 without off-target labeling.

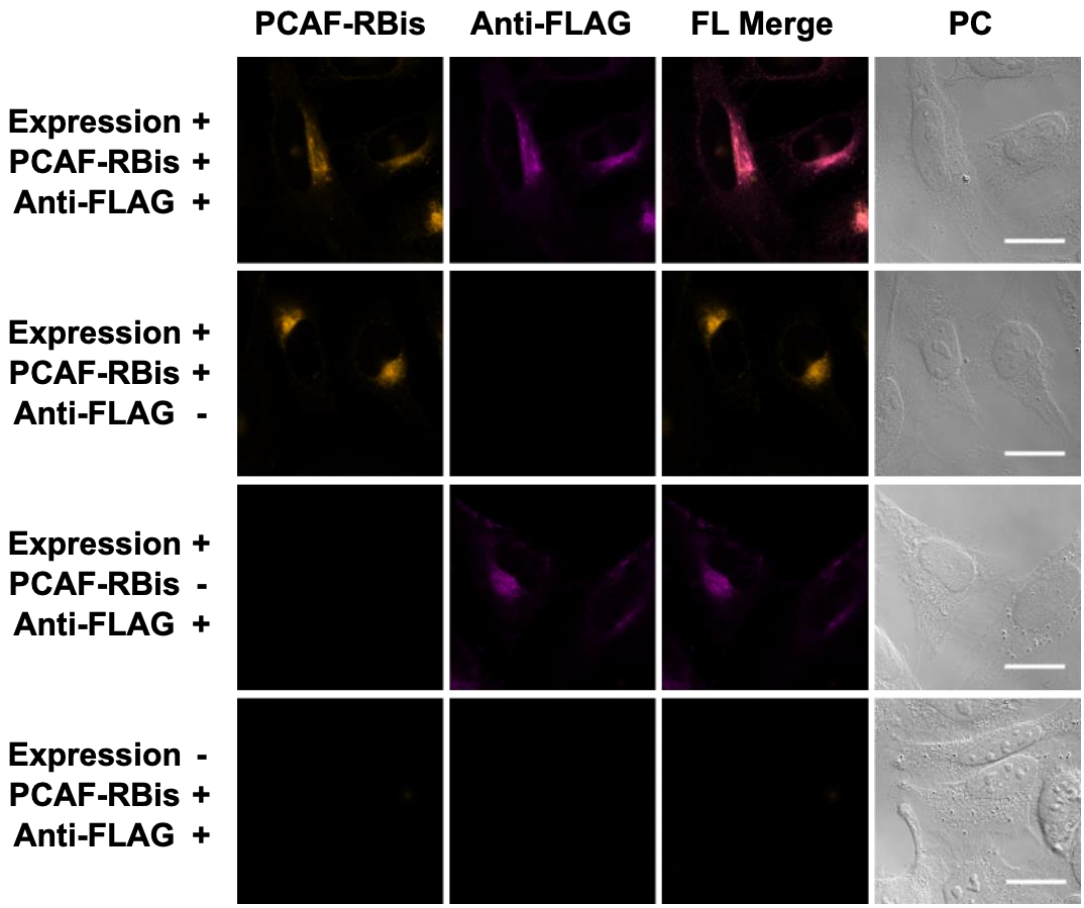

Figure 3-4. Multicolor imaging of HeLa cells stably expressing PYP^{WT}-GLUT4 or HeLa cells stained with **PCAF-RBis** (1.25 μM) and Alexa Fluor 647 conjugated antibody for visualization of GLUT4. All images were obtained with the excitation at 561 and 633 nm and detection at 570–620 (orange) and 640–700 (magenta) nm emission, respectively. Scale bars, 20 μm. FL and PC denote fluorescence image and phase contrast image, respectively. FL Merge denotes FL orange image merged with FL magenta image. Experiments were performed twice, giving similar results.

3.2.2. Membrane-localized GLUT4 imaging

Next, based on the successful selective labeling of membrane proteins using **PCAF-SP-s** (described in Chapter 2), the author considered that **PCAF-SP-s** can be applied to the visualization of the cell membrane-localized GLUT4 in live cells. Imaging experiments using **PCAF-SP-s** were conducted for the labeling of GLUT4 with insulin stimulation. According to the protocol described in previous reports[11,12] for membrane-localized GLUT4 imaging, HeLa cells stably expressing PYP^{WT}-GLUT4 were stimulated with insulin after incubation with the starvation medium for three hours. Upon the addition of **PCAF-SP-s**, fluorescence signals were observed in the cell membrane region of GLUT4-expressing HeLa cells, while fluorescence signals were not observed in HeLa cells, which do not express PYP-tag protein. These images indicated that sulfonate-conjugated **PCAF-SP-s** could selectively label membrane-localized GLUT4 in live cells (Figure 3-5).

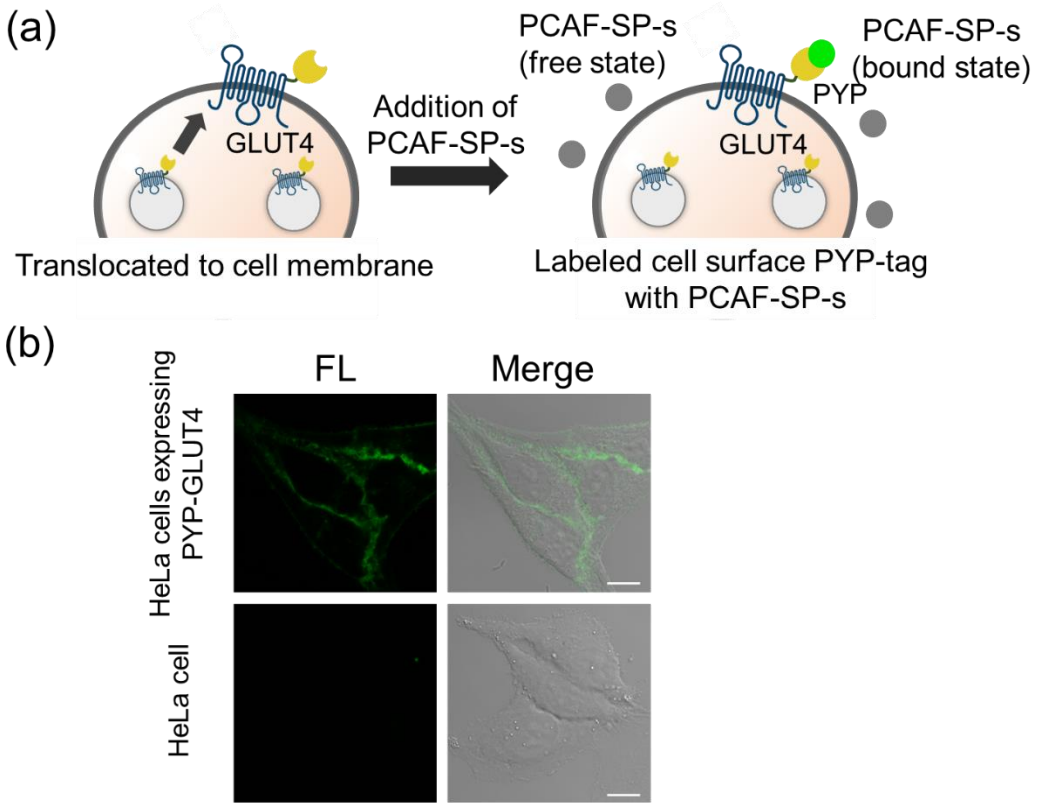

Figure 3-5. (a) Schematic view of insulin-stimulated GLUT4 imaging with **PCAF-SP-s**. (b) Fluorescence images and merged images with a phase contrast image of HeLa cells stably expressing PYP^{WT}-GLUT4 or HeLa cells (non-expressed PYP-tag) stained with **PCAF-SP-s** (1.5 μM). All images were obtained with the excitation at 488 nm by detecting 500–630 (green) emission. Scale bars, 10 μm. Experiment was performed twice with similar results.

To further confirm the specificity of **PCAF-SP-s** labeling, dual-color imaging was conducted using immunostaining and **PCAF-SP-s** labeling. Live-cell imaging in Figure 3-5. enables real-time imaging of the GLUT4 localization, while insulin wash-out, fixation, and immunostaining were required to afford objective images in the experimental protocol for immunostaining of membrane-localized GLUT4. Namely, a lag time occurs before microscopic observation in GLUT4 immunostaining. As shown in Figure 3-6, the fluorescence signals derived from **PCAF-SP-s** labeling on the cell membrane overlaps with the location of signals derived from immunostaining. However, the signals from **PCAF-SP-s** were observed not only in the cell membrane region but also in the cytoplasmic region of a few cells. This result implies that GLUT4 was internalized between the process of insulin wash-out and fixation, following the GLUT4 labeling with **PCAF-SP-s**. In contrast, immunostaining in GLUT4-expressing cells with insulin stimulation could not result in fluorescence signals in the cytoplasmic region. These observations suggest that insulin stimulation might inhibit the antibody recognition of the FLAG-tag, because the interactions between biomolecules and GLUT4 may occur near the epitope sequence following GLUT4 internalization. Additional studies would be necessary to completely understand these observations, but these studies are outside the scope of this work.

To confirm no bleed-through in each channel, control experiments involving either single labeling with **PCAF-SP-s** (green) or immunostaining (magenta) with antibody experiments (the 2nd and the 3rd row in Figure 3-6) were performed, indicating no bleed-through between channels. In HeLa cells, which do not express PYP-tag proteins, the fluorescence signals were not observed in the image (the 4th row in Figure 3-6). These results indicated that **PCAF-SP-s** does not show off-target labeling.

Overall, the author demonstrated that **PCAF-SP-s** can specifically label membrane-localized GLUT4 without off-target labeling by live-cell imaging and dual-color imaging with immunostaining.

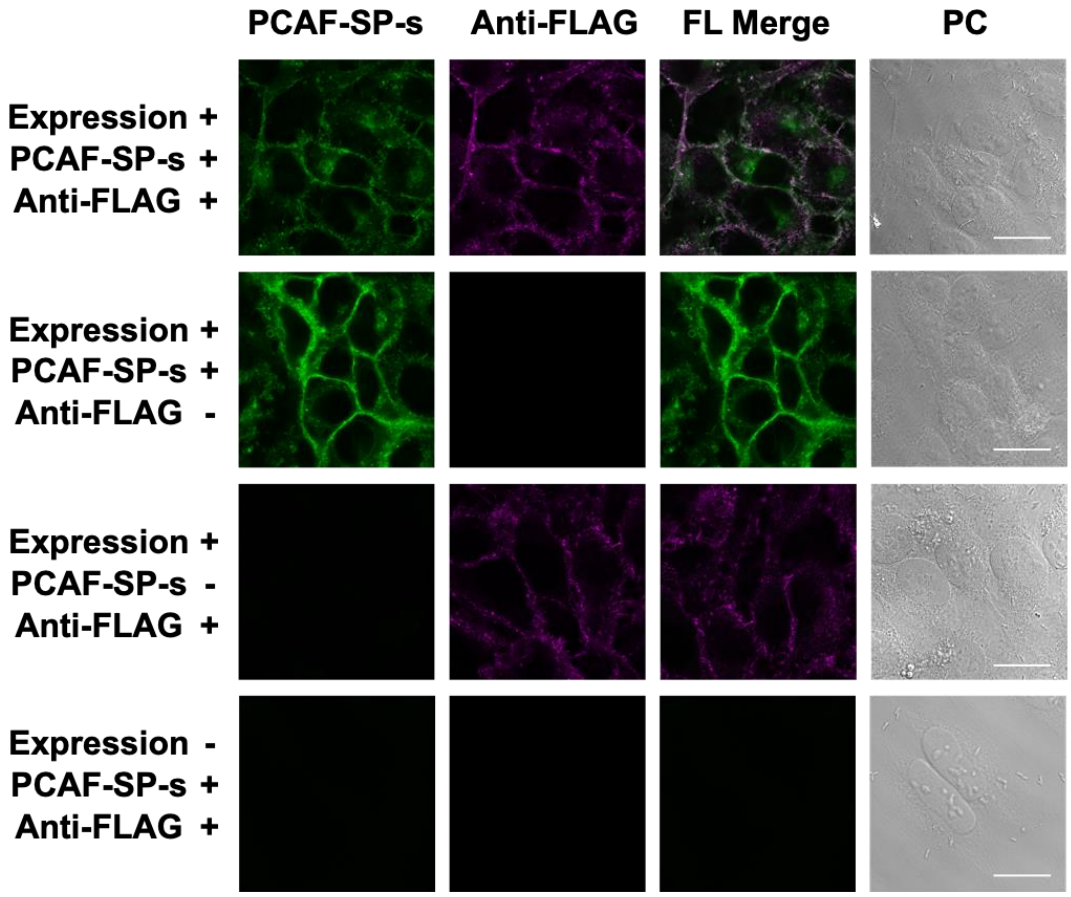

Figure 3-6. Multicolor imaging of HeLa cells stably expressing PYP^{WT}-GLUT4 or HeLa cells stained with **PCAF-SP-s** (2.5 μM) and Alexa Fluor 647 conjugated antibody for visualization of GLUT4. All images were obtained with the excitation at 488 and 633 nm and detection at 500–620 (green) and 640–700 (magenta) nm emission, respectively. Scale bars, 20μm. FL and PC denote fluorescence image and phase contrast images, respectively. FL Merge denotes FL green image merged with FL magenta image. Experiments were performed twice, giving similar results.

3.2.3. Visualized GLUT4 multiple localizations using PCAF-RBis and PCAF-SP-s

Encouraged by the success of specifically labeling intracellular and membrane-localized GLUT4, the author employed **PCAF-RBis** and **PCAF-SP-s** to visualize GLUT4 multiple localizations. According to the protocol for imaging membrane-localized GLUT4 in this work, GLUT4 that was stimulated with insulin to translocate to the cell membrane was first labeled with **PCAF-SP-s**. The culture medium (low-glucose

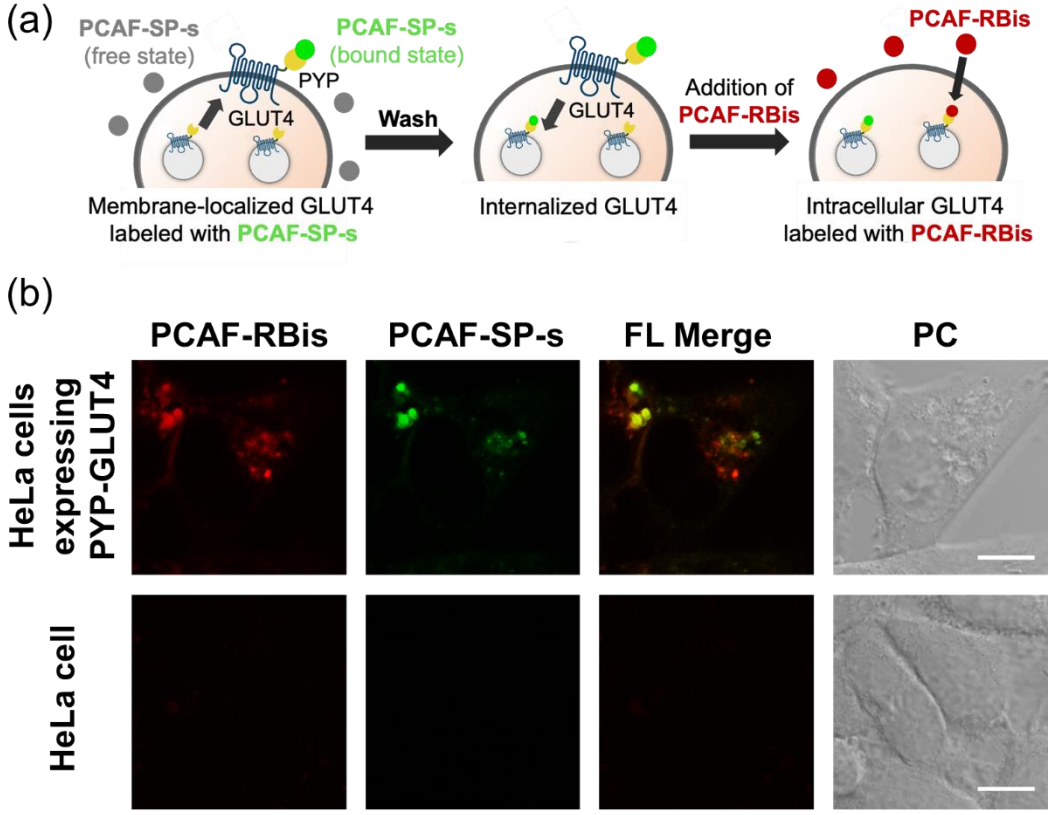

Figure 3-7. (a) Schematic view of GLUT4 multiple localization imaging with **PCAF-SP-s** and **PCAF-RBis.** (b) Multicolor imaging of HeLa cells stably expressing PYP^{WT}-GLUT4 or HeLa cells (non-expressed PYP-tag) stained with **PCAF-RBis** (1.25 μM) and **PCAF-SP-s** (1.5 μM) for visualization of multiple localizations of GLUT4. All images were obtained with the excitation at 488 and 561 nm and detection at 500–630 (green) and 635–705 (red) nm emission, respectively. Scale bars, 10 μm. FL and PC denote fluorescence image and phase contrast image, respectively. FL Merge denotes FL Red image merged with FL green image. Experiments were performed twice with similar results.

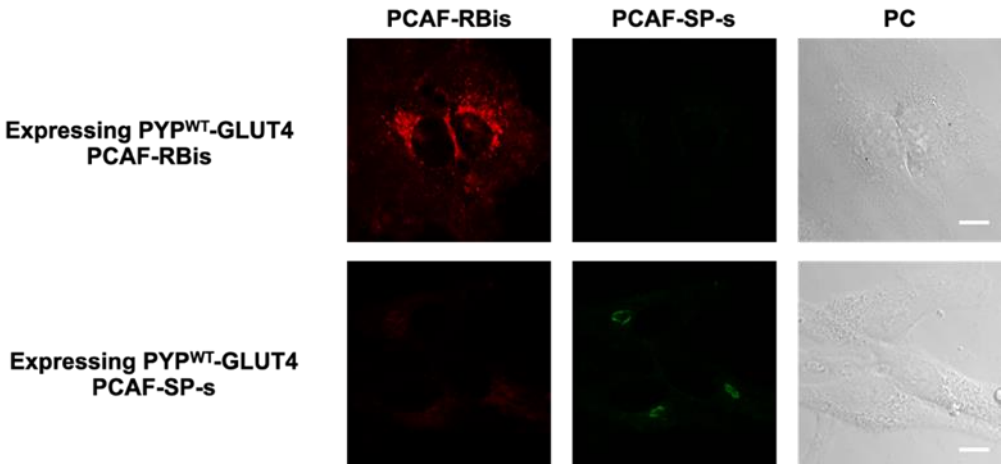

Figure 3-8. Multicolor imaging of HeLa cells stably expressing PYP^{WT}-GLUT4 stained with **PCAF-RBis** (1.25 μM) and **PCAF-SP-s** (1.5 μM) for visualization of GLUT4. All images were obtained with the excitation at 488 and 561 nm and detection at 500–630 (green) and 635–705 (red) nm emission, respectively. Scale bars, 10 μm. FL and PC denote fluorescence image and phase contrast image, respectively. FL Merge denotes FL orange image merged with FL magenta image. Experiments were performed twice, giving similar results.

KRB) with insulin and **PCAF-SP-s** was replaced with fresh low-glucose KRB for the GLUT4 internalization; then, intracellular GLUT4 was labeled with **PCAF-RBis**. As shown in Figure 3-7, the localizations of signals derived from **PCAF-RBis** did not partially overlap with those derived from **PCAF-SP-s**. In addition, control experiments were performed to confirm the level of bleed-through between channels, indicating that this level is negligible (Figure 3-8.). According to a previous report, insulin-responsive and insulin-unresponsive GLUT4 show differences in the localization. These results, which do not completely match the distribution of **PCAF-RBis** and **PCAF-SP-s**, demonstrate the successful visualization of GLUT4 at multiple locations.

Overall, the usefulness of a novel probe design was demonstrated by the fact that tetrazole-conjugated **PCAF-RBis** enables the visualization of multiple localizations of POIs in live cells.

3.3 Conclusion

In this chapter, the visualization of GLUT4 multiple localizations as a live-cell protein imaging application of **PCAF-RBis** and **PCAF-SP-s** was described. **PCAF-RBis** was employed for the visualization of intracellular GLUT4. As a result of intracellular GLUT4 imaging, fluorescent signals were observed in the cytoplasmic region of live cells expressing PYP-GLUT4, indicating that **PCAF-RBis** could label intracellular GLUT4. In control experiments, fluorescence signals were not observed, indicating that **PCAF-RBis** could label intracellular GLUT4 without undesired signals. Furthermore, dual-color imaging using both **PCAF-RBis** labeling and immunostaining was conducted in HeLa cells expressing PYP-GLUT4, resulting in overlapping signals derived from **PCAF-RBis** and immunostaining. These results demonstrated that **PCAF-RBis** can specifically label intracellular GLUT4 without off-target labeling.

Next, imaging experiments using **PCAF-SP-s** were conducted for the labeling of GLUT4 with insulin stimulation. Upon the addition of **PCAF-SP-s**, fluorescence signals were observed in the cell membrane region of live cells expressing PYP-GLUT4, while fluorescence signals were not observed in a control experiment. These images indicated that sulfonate-conjugated **PCAF-SP-s** could selectively label membrane-localized GLUT4 in live cells.

PCAF-RBis and **PCAF-SP-s** were employed to visualize GLUT4 multiple localizations. As a result, the localizations of signals derived from **PCAF-RBis** did not partially overlap those derived from **PCAF-SP-s**. This result demonstrated the successful visualization of GLUT4 at multiple locations.

3.4 Experimental Sections

3.4.1 General

General chemicals were supplied by Tokyo Chemical Industries, Wako Pure Chemical Industries, Sigma-Aldrich Chemical Co., and Kishida Chemical Co., and used without further purification. Live fluorescent cell images were acquired using a confocal laser-scanning microscope (Zeiss, LSM-880) with a 63× lens, respectively.

3.4.2 Cell culture

HeLa cells were purchased from RIKEN BRC. HeLa cells and stable HeLa cells expressing PYP-GLUT4^{WT} were cultured in Dulbecco's Modified Eagle Medium (DMEM) containing 10% fetal bovine serum (FBS) and antibiotics (100 U ml^{-1} penicillin and 0.1 mg ml^{-1} streptomycin) and a 5% CO_2 atmosphere at 37 °C.

3.4.3 Live-cell imaging of intracellular GLUT4 using PCAF-RBis

Stable HeLa cell lines expressing PYP-GLUT4^{WT} were cultured in DMEM supplemented with 10% FBS. The medium was replaced with Krebs-Ringer bicarbonate (KRB) buffer, then the cells were incubated for 3 h. Following the incubation of KRB buffer, **PCAF-RBis** (1.25 μM) was added to the cells and incubated for 20 min. After washing the cells three times with KRB buffer, the medium was replaced with FluoroBrite DMEM, and all images were captured at an excitation frequency of 561 nm with an emission range of 635–705 (red), using a 63× lens (Zeiss LSM 880).

3.4.4 Immunostaining of intracellular PYP-GLUT4^{WT} using anti-FLAG and labeling with PCAF-RBis

Stable HeLa cell lines expressing PYP-GLUT4^{WT} were incubated in KRB buffer for three hours, and then incubated with **PCAF-RBis** (1.25 μM) for 20 min. After washing the cells three times with PBS, and then incubated with formaldehyde solution on ice for 15 min. The cells were washed three times with PBS, incubated with 0.1% Triton for 5 minutes at room temperature, and then washed with PBS. The cells were treated with 5% BSA for 30 minutes, and then incubated with anti-FLAG antibody as primary antibody in PBS with 3% BSA for an hour at room temperature. After washing with PBS for 5 min (3x), the cells were incubated with secondary antibody (anti-mouse conjugated Alexa647) in PBS with 3% BSA for an hour at room temperature. All images were captured using excitation frequencies of 561 nm and 633 nm with emission ranges of 570-620 nm (orange) and 640-700 nm (magenta), respectively, using 63x lens (Zeiss LSM 880).

3.4.5 Live-cell imaging of GLUT4 with insulin stimulation using PCAF-SP-s

Stable HeLa cell lines expressing PYP-GLUT4^{WT} were cultured in DMEM supplemented with 10% FBS. The medium was replaced with Krebs-Ringer bicarbonate (KRB) buffer, and the cells were incubated for 3 h. Following incubation with KRB buffer, insulin (100 nM) was added to the cells and incubated for 20 min. After insulin stimulation, **PCAF-SP-s** (1.5 µM) was added to the cells and incubated for 10 minutes. After washing the cells with KRB buffer three times, the medium was replaced with FluoroBrite DMEM and all images were captured at an excitation frequency of 488 nm with an emission range of 500–630 nm using a 63× lens (Zeiss LSM 880).

3.4.6 Immunostaining of PYP-GLUT4^{WT} using anti-FLAG and labeling with PCAF-SP-s

Stable HeLa cell lines expressing PYP-GLUT4^{WT} were cultured in DMEM supplemented with 10% FBS. The medium was replaced with Krebs-Ringer bicarbonate (KRB) buffer, and the cells were incubated for 3 h. Following incubation with KRB buffer, insulin (100 nM) was added to the cells and incubated for 20 min. After insulin stimulation, **PCAF-SP-s** (2.5 µM) was added to the cells and incubated for 10 minutes. After washing the cells three times with PBS, and then incubated with formaldehyde solution on ice for 15 min. The cells were washed three times with PBS, incubated with 0.1% Triton for 5 minutes at room temperature, and then washed with PBS. The cells were treated with 5% BSA for 30 minutes, and then incubated with anti-FLAG antibody as primary antibody in PBS with 3% BSA for an hour at room temperature. After washing with PBS for 5 min (3x), the cells were incubated with secondary antibody (anti-mouse conjugated Alexa647) in PBS with 3% BSA for an hour at room temperature. All images were captured using excitation frequencies of 561 nm and 633 nm with emission ranges of 500-620 nm (green) and 640-700 nm (magenta), respectively, using 63x lens (Zeiss LSM 880).

3.4.7 Multicolor imaging for visualization of multiple localization of GLUT4 labeled with PCAF-SP-s and PCAF-RBis

Stable HeLa cell lines expressing PYP-GLUT4^{WT} were cultured in DMEM supplemented with 10% FBS. The medium was replaced with Krebs-Ringer bicarbonate (KRB) buffer, and the cells were incubated for 3 h. Following incubation with KRB buffer, insulin (100 nM) was added to the cells and incubated for 20 min. After insulin stimulation, **PCAF-SP-s** (1.5 µM) was added to the cells and incubated for 10 min. The medium was replaced with KRB buffer without insulin and the cells were incubated for 20 min. **PCAF-RBis** (1.25 µM) was added to the cells and incubated for 20 min. After washing the cells with

KRB buffer three times, the medium was replaced with FluoroBrite DMEM, and all images were captured using excitation frequencies of 488 nm and 561 nm with emission ranges of 500–630 (green) and 635–705 (red) nm, respectively, using a 63× lens (Zeiss LSM 880).

3.5 Reference

1. Augustin, R. The Protein Family of Glucose Transport Facilitators: It's Not Only about Glucose after All. *IUBMB Life* **2010**, *62* (5), 315–333.
2. Haga, Y.; Ishii, K.; Suzuki, T. N-Glycosylation Is Critical for the Stability and Intracellular Trafficking of Glucose Transporter GLUT4. *J. Biol. Chem.* **2011**, *286* (36), 31320–31327.
3. Mueckler, M. Facilitative Glucose Transporters. *European Journal of Biochemistry* **1994**, *219* (3), 713–725.
4. Garvey, W. T.; Maianu, L.; Zhu, J. H.; Brechtel-Hook, G.; Wallace, P.; Baron, A. D. Evidence for Defects in the Trafficking and Translocation of GLUT4 Glucose Transporters in Skeletal Muscle as a Cause of Human Insulin Resistance. *J. Clin. Invest.* **1998**, *101* (11), 2377–2386.
5. Tanaka, M.; Nishi, M.; Morimoto, M.; Sugimoto, T.; Kawata, M. Yellow Fluorescent Protein-Tagged and Cyan Fluorescent Protein-Tagged Imaging Analysis of Glucocorticoid Receptor and Importins in Single Living Cells.
6. Wang, X.; Li, S. Protein Mislocalization: Mechanisms, Functions and Clinical Applications in Cancer. *Biochimica et Biophysica Acta* **2014**, *1998* (1), 13–25.
7. Harada, Y.; Hirayama, H.; Suzuki T. Generation and degradation of free asparagine-linked glycans *Cell Mol. Life Sci.*, **2015**, 72, 2509–2533.
8. Suzuki, T. Catabolism of N-Glycoproteins in Mammalian Cells: Molecular Mechanisms and Genetic Disorders Related to the Processes. *Mol. Aspects Med.*, **2016**, *51*, 89–103.
9. Fregno, I.; Fasana, E.; Soldà, T.; Galli, C.; Molinari, M. *N*-glycan Processing Selects ERAD-resistant Misfolded Proteins for ER-to-lysosome-associated Degradation. *The EMBO Journal* **2021**, *40* (15), e107240.
10. Shi, J.; Kandror, K. V. Sortilin Is Essential and Sufficient for the Formation of Glut4 Storage Vesicles in 3T3-L1 Adipocytes. *Dev. Cell* **2005**, *9*, 99–108.
11. Hirayama, S.; Hori, Y.; Benedek, Z.; Suzuki, T.; Kikuchi, K. Fluorogenic Probes Reveal a Role of GLUT4 N-Glycosylation in Intracellular Trafficking. *Nat. Chem. Biol.*, **2016**, ***12***, 853–859.
12. Nishiura, M.; Hori, Y.; Umeno, M.; Kikuchi, K. Visualization of Multiple Localizations of GLUT4 by Fluorescent Probes of PYP-Tag with Designed Unnatural Warhead. *Chem. Sci.* **2023**, *14* (22), 5925–5935.

Chapter 4. Bioisostere-conjugated probe for live-cell protein imaging based on HaloTag system

4.1 Introduction

As described in the Section **1.1.4** and Chapter 2, a protein labeling method using synthetic fluorescent probes and HaloTag is a useful approach for live-cell protein imaging.[1-9] The combination of HaloTag with synthetic fluorescent probes is attractive for bioimaging. HaloTag is a modified bacterial haloalkane dehalogenase derived from *Rhodococcus* sp., and its molecular size is 33 kDa. Asp106 of HaloTag binds to chloroalkane as a HaloTag ligand (HTL) through a nucleophilic substitution reaction to form a covalent bond, resulting in an ester structure. Furthermore, HaloTag protein mutants, such as HaloTag7 (HT7), were created to increase the reaction rate with probes composed of chloroalkane and functional groups, and their complexes show higher stability compared to the unmutated HaloTag.[9] Several semisynthetic probes based on HaloTag and synthetic probes can be applied for the real-time monitoring of biomolecules in live cells. Various non-fluorescent molecules, composed of HaloTag ligand (chloroalkane, CA) and reactive moieties such as azido and electrophile groups, have also been developed for biological studies.[9-11]

Encouraged by the success of tetrazole-conjugated PYP-tag labeling probes (**PCAF-RBis** and **PCAF-SPis**) that enable the visualization of intracellular proteins without undesired accumulation, new HaloTag labeling probes were developed to enhance the versatility of the probe design using tetrazole.[12] In this chapter, the author demonstrated that the novel design using a bioisostere can be applied to the HaloTag system.

4.2 Results and discussion

4.2.1 Molecular design, synthesis, and photoproperties of membrane-permeable HaloTag labeling probes

To design novel HaloTag labeling probes, the author considered that the always-on probe is desirable to confirm the cellular behavior of the probes in both free and bound states. Encouraged by the success of developing the always-on PYP-tag labeling probe (**PCAF-RBis**), the author selected RB as a cationic dye scaffold. Based on the above, the author designed bioisostere-conjugated RB-based probes, **HTL-RBis**, for live-cell imaging of intracellular proteins using the HaloTag system (Figure 4-1). **HTL-RBis** has a tetrazole group and a chloroalkane as a HTL. The net charge of **HTL-RBis** is zero under physiological conditions. In addition, to confirm the effect of introducing a tetrazole, the author also designed a cationic probe, **HTL-RB**, that does not contain a tetrazole (Figure 4-1).

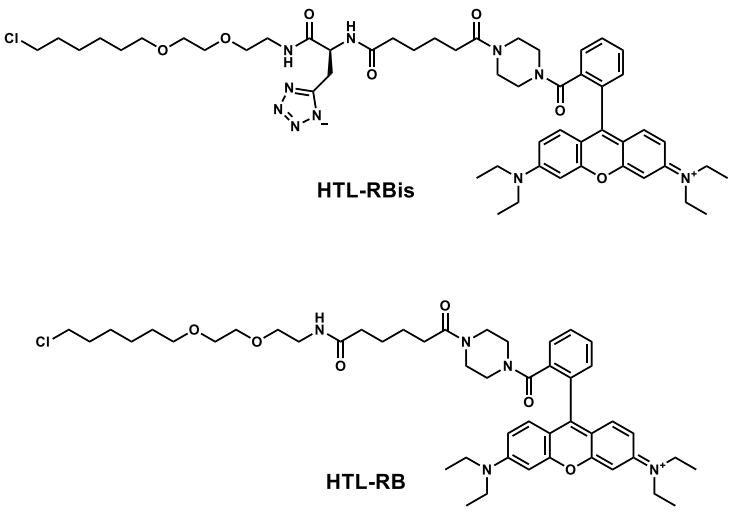

Figure 4-1. HTL-RBis and **HTL-RB**.

The synthesis of **HTL-RBis** and **HTL-RB** is shown in Scheme 4-1. Following the general synthetic route of HTL moiety,[11,13,14] **18** was prepared from 2-(2-aminoethoxy)ethanol as a starting material through Boc protection, Williamson ether synthesis, and Boc deprotection. In the **HTL-RBis** synthesis, a tetrazole-conjugated HTL derivative was prepared from **18** and **6**, then **HTL-RBis** was successfully synthesized by the conjugation of **8** and a tetrazole-conjugated HTL derivative through Fmoc deprotection and the conjugation reaction using HBTU. **HTL-RB** was also successfully synthesized through the direct conjugation of **8** and **6**.

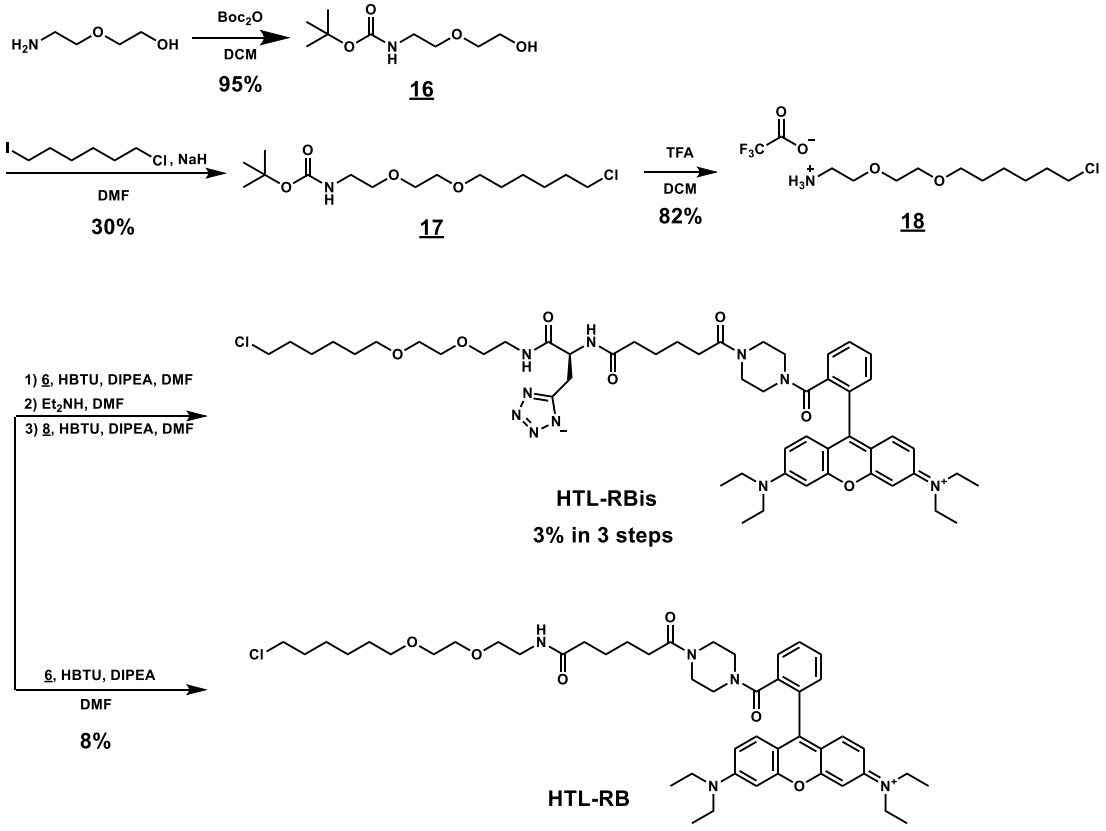

Scheme 4-1. Synthesis of **HTL-RBis** and **HTL-RB**.

The author conducted fluorescence analysis of the photophysical properties of **HTL-RBis** and **HTL-RB**, indicating that the probes emitted fluorescence under physiological conditions (Figure 4-2 and Table 4-1).

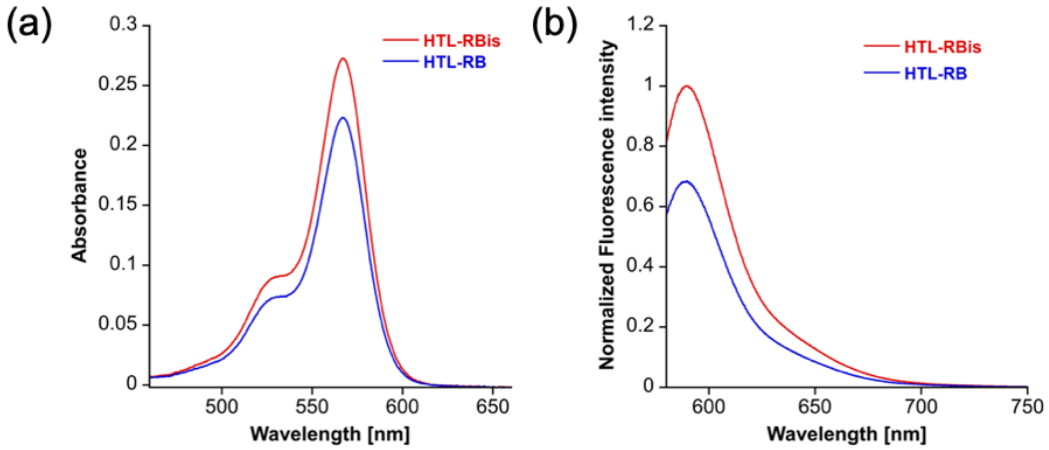

Figure 4-2. (a) Absorption spectra of 5.0 μM **HTL-RBis** and **HTL-RBis**. (b) Fluorescence spectra of 5.0 μM **HTL-RBis** and **HTL-RBis**. These spectra were measured in aqueous solution (20 mM HEPES, 150 mM NaCl, and 0.1% DMSO) buffered to pH 7.4 at 37 °C. The spectra were obtained with the excitation at 567 nm.

Table 4-1. Photophysical properties of Halo tag labeling probes

Probe	λ_{abs} [nm]	$\varepsilon^{[a]}$ [M^{-1} cm^{-1}]	λ_{em} [nm]	Φ_{fl}
HTL-RBis	567	50000	590	0.24
HTL-RB	567	45000	590	0.20

[a] ε is extinction coefficient at λ_{abs}.

4.2.2 Live-cell imaging using novel HaloTag labeling probes

Then, live-cell imaging experiments were performed to confirm the labeling ability and intracellular behavior of **HTL-RBis** and **HTL-RB**, respectively. HEK293T cells were transfected with a plasmid (pcDNA3.1(+)–Halo-NLS or empty vector) using Lipofectamine 3000 reagent according to the procedures described in the experimental section. **HTL-RBis** successfully visualized NLS-fused HaloTag protein (Halo-NLS) in expressing cells, and non-specific illuminations were significantly decreased. In contrast, **HTL-RB** showed undesired fluorescence signals in the cytoplasmic region of HaloTag-expressed cells and mock cells (transfected with empty vector). These results indicated that the tetrazole-conjugated HaloTag labeling probe (**HTL-RBis**) enables the visualization of the intracellular proteins by significantly decreasing undesired accumulation (Figure 4-2).

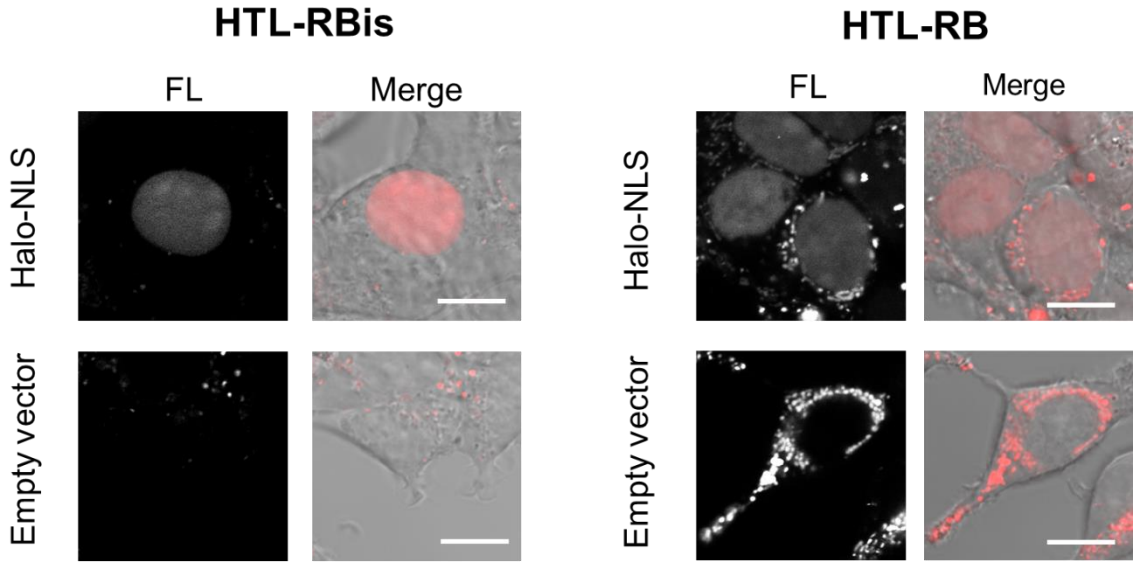

Figure 4-2. Fluorescence images and merged images with phase contrast image of HEK293T cells expressing HA-Halo-NLS or mock cells (transfected empty vector) stained with 2.5 μM (a) **HTL-RBis** and (b) **HTL-RB**. The images were measured 566–685 nm emission with the excitation at 561 nm. Scale bars, 10 μm. FL denotes Fluorescence image. This experiment was performed twice with similar results.

4.3 Conclusion

In this chapter, the development of the tetrazole-conjugated HaloTag labeling probe was described. The novel probe design based on the tetrazole conjugation was extended to the HaloTag system to enhance the versatility of a new probe design using a hydrophobic bioisostere. To confirm the cellular behavior of the probes in both free and bound states, always-on HaloTag labeling probes were developed. Encouraged by the success of the development of always-on PYP-tag labeling probe (**PCAF-RBis**), RB as a cationic dye scaffold was employed for the development of HaloTag labeling probes. The author successfully synthesized the bioisostere-conjugated HaloTag labeling probe, **HTL-RBis**, and revealed that **HTL-RBis** showed fluorescence under physiological conditions. As a result of live-cell imaging using **HTL-RBis** and **HTL-RB**, **HTL-RBis** could be applied to visualize intracellular proteins with significantly reduced non-specific accumulation, compared with the staining pattern of **HTL-RB**. These results indicated that the novel design can be applied to develop the HaloTag labeling probe for the visualization of intracellular proteins in live cells.

4.4 Experimental sections

4.4.1 Synthetic procedures

Synthesis of **16**

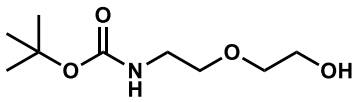

16

A solution of Boc_2O (6.35 g, 30.0 mmol) in DCM (35 mL) was slowly added to a solution of 2-(2-aminoethoxy)-ethanol (3.18 g, 30.0 mmol) in DCM (20 mL) at 0 °C. The reaction solution was stirred at 0 °C for 30 min and warmed to room temperature overnight. The reaction mixture was washed with water and the aqueous layer was extracted with DCM (3× 50 mL). The combined extracts were washed with brine, dried over Na_2SO_4, filtered, and concentrated *in vacuo* to obtain the title compound as a colorless oil (5.86 g, 28.6 mmol) in 95% yield. The product was sufficiently pure and used without further purification.

^{1}H NMR (600 MHz, $CDCl_3$): δ 5.08 (br, 1H, H), 3.76-3.73 (m, 2H), 3.58 (t, *J*= 4.2 Hz, 2H), 3.56 (t, *J*= 4.2 Hz, 2H), 3.34-3.33 (m, 2H), 2.59 (s, 1H), 1.45 (s, 9H).**^{13}C NMR (150 MHz, $CDCl_3$)**: δ 156.2, 79.5, 72.3, 70.4, 61.8, 40.4, 28.5. **HRMS (ESI+):** Calcd for $[M+Na]^+$ 228.1206, found 228.1209

Synthesis of **17**

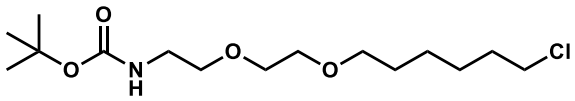

17

A suspension of NaH (60% in oil, 267 mg, 6.5 mmol) in dry hexane was washed with dry hexane three times and then the excess hexane was removed. A solution of compound **16** (1.03 g, 5.0 mmol) in dry THF was slowly added to the suspension at 0 °C and stirred for 30 min under N_2. The reaction mixture was warmed to room temperature and stirred overnight. We added 10 mL of aqueous 10% NH_4Cl and EtOAc, and the aqueous layer was extracted three times with 100 mL EtOAc. The organic layers were combined, washed with brine, dried over Na_2SO_4, filtered, and concentrated *in vacuo*. The residue was purified using silica gel column chromatography (hexane/ EtOAc = 55/45 to 30/70

as eluent) to yield compound **17** as a colorless oil (491 mg, 1.52 mmol) with a 30% overall yield.

^{1}H NMR (600 MHz, $CDCl_3$): δ 5.02 (br, 1H), 3.62-3.53 (m, 8H), 3.47 (t, *J*= 6.0 Hz, 2H), 3.33-3.32 (m, 2H), 1.81-1.76 (m, 2H), 1.64-1.59 (m, 2H), 1.49-1.46 (m, 2H), 1.40-1.35 (m, 2H), 1.44 (s, 9H).**^{13}C NMR (150 MHz, $CDCl_3$)**: δ 156.1, 79.2, 71.3, 70.3, 70.1, 45.1, 40.4, 32.6, 29.5, 28.5, 26.8, 25.5. **HRMS (ESI+):** Calcd for $[M+Na]^+$ 346.1756, found 346.1749.

Synthesis of **18**

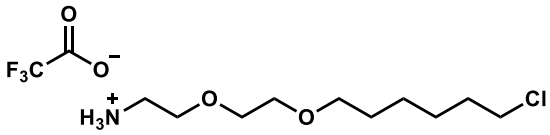

18

TFA (1 mL) was added to a solution of compound **17** in DCM (4 mL) and stirred at room temperature for 4 h. The reaction mixture was concentrated *in vacuo* and the resultant solution was purified by silica gel column chromatography (DCM/MeOH = 99/1 to 20/80 as eluent) to yield compound **18** (239 mg, 0.709 mmol) with an 82% overall yield.

^{1}H NMR (600 MHz, $CDCl_3$): δ 5.73 (br, 3H), 3.68-3.57 (m, 6H), 3.53 (t, *J*= 7.2 Hz, 2H), 3.45 (t, *J*= 7.2 Hz, 2H), 3.15 (m, 2H), 1.78-1.74 (m, 2H), 1.60-1.55 (m, 2H), 1.46-1.41 (m, 2H), 1.36-1.30 (m, 2H).**^{13}C NMR (150 MHz, $CDCl_3$)**: δ 162.5 (q, *J*= 149.4 Hz ^{13}C-F coupling), 116.4 (q, *J*= 1160 Hz ^{13}C-F coupling), 71.3, 70.1, 69.7, 66.5, 53.8, 45.2, 39.8, 32.5, 29.1, 26.6, 25.2. **HRMS (ESI+):** Calcd for $[M+H]^+$ 224.1412, found 224.1417.

Synthesis of **HTL-RB**

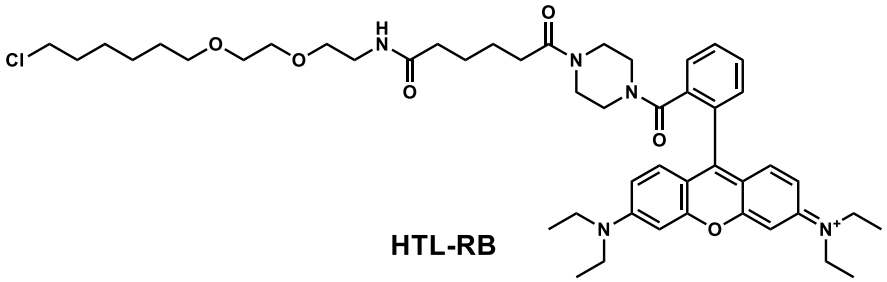

HTL-RB

DIPEA (129 mg, 1.00 mmol) and compound **8** (32 mg, 0.050 mmol) were dissolved in DMF (8 mL). HBTU (38 mg, 0.10 mmol) was added to the resulting solution, which was stirred at 0 °C for 45 min. We added compound **18** (86 mg, 0.26 mmol) in DMF (2 mL) to the reaction mixture. The solution was warmed to room temperature and stirred overnight. After removing the solvent, the residue was purified by reverse-phase HPLC using an ODS-3 column and eluted with H_2O/CH_3CN containing 0.1% TFA to yield the title compound (3.5 mg, 4.2 μmol) with an 8% overall yield.

^{1}H NMR (600 MHz, DMSO-d_6): δ 7.82-7.53 (m, 4H), 7.15 (d, *J* = 9.0 Hz, 2H), 7.11 (dd, *J* = 9.0 Hz, *J* = 1.8 Hz, 2H), 6.95 (d, *J* = 1.8 Hz, 2H), 3.65 (q, *J* = 9.6 Hz, 8H), 3.63-3.16 (m, 21H), 2.25 (t, *J* = 9.6 Hz, 2H), 2.07-2.05 (m, 2H), 1.73-1.67 (m, 2H), 1.51-1.26 (m, 10H), 1.20 (t, *J* = 9.6 Hz, 12H).**^{13}C NMR (150 MHz, DMSO-d_6)**: δ 172.6, 171.2, 157.6, 156.1, 155.6, 135.8, 132.3, 131.3, 131.0, 130.3, 128.0, 114.8, 113.6, 96.4, 70.7, 70.1, 70.0, 69.7, 45.9, 45.9, 39.0, 32.5, 29.6, 26.6, 25.5, 13.0. **HRMS (FAB+):** Calcd for $[M]^+$ 844.4774, found 844.4776.

Synthesis of **HTL-RBis**

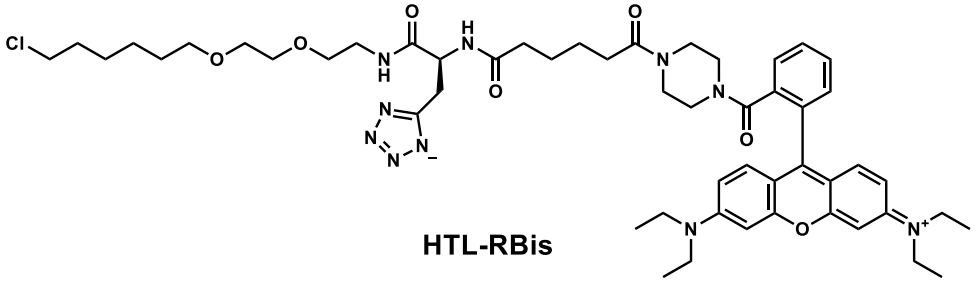

HTL-RBis

DIPEA (129 mg, 1.00 mmol) and compound **6** (126 mg, 0.330 mmol) were dissolved in DMF (8 mL). HBTU (150 mg, 0.396 mmol) was added to the resulting solution at 0 °C and stirred at 0 °C for 45 min. We added compound **18** (134 mg, 0.396 mmol) in DMF (2 mL) to the reaction mixture, which was warmed to room temperature and stirred overnight. The solution was concentrated *in vacuo*. Then we added 10% Diethyl amine in DMF (3 mL) to the residue and stirred the mixture at room temperature for 4 h. After removing the solvent, we added DIPEA (129 mg, 1.00 mmol) and HBTU (75 mg, 0.170

mmol) in DMF (2 mL) to the residue, and stirred the mixture at 0 °C for 45 min. We added compound **8** (86 mg, 0.26 μmol) in DMF (2 mL) to the reaction mixture at 0 °C, warmed the solution to room temperature, and stirred it overnight. The solution was concentrated *in vacuo*, and the residue was purified by reverse-phase HPLC using an ODS-3 column and eluted with H_2O/CH_3CN containing 0.1% TFA to yield the title compound (4.3 mg, 4.4 μmol) with a 3% overall yield.

^{1}H NMR (600 MHz, DMSO-*d*$_6$): δ 8.09 (br, 1H), 7.97 (br, 1H), 7.77-7.71 (m, 3H), 7.53 (br, 1H), 7.15 (d, *J* = 9.6 Hz, 2H), 7.11 (dd, *J* = 9.6 Hz, *J* = 1.8 Hz, 2H), 6.95 (d, *J* = 1.8 Hz, 2H), 4.68-4.67 (m, 2H), 3.65 (q, *J* = 9.6 Hz, 8H), 3.63-3.16 (m, 24H), 2.22 (t, *J* = 9.6 Hz, 2H), 2.08-2.07 (m, 2H), 1.71-1.66 (m, 2H), 1.51-1.26 (m, 10H), 1.20 (t, *J* = 9.6 Hz, 12H).**^{13}C NMR (150 MHz, DMSO-*d*$_6$)**: δ 172.6, 171.2, 170.4, 157.6, 156.1, 155.6, 135.8, 132.3, 131.3, 131.0, 130.3, 128.0, 114.8, 113.6, 96.4, 70.7, 70.1, 69.9, 69.3, 51.5, 45.9, 45.9, 39.0, 32.5, 29.6, 26.6, 25.5, 13.0. **HRMS (ESI+):** Calcd for $[M]^+$ 983.5268, found 983.5289.

4.4.2 Biological experiment procedures

4.4.2.1 Plasmid construction

pcDNA3.1(+)-HA-Halo-NLS was performed as previously described.[15]

4.4.2.2 Absorption spectroscopy

Absorption spectra were measured after the probe (5.0 μM) was incubated with or without PYP-tag (10 μM) in the assay buffer (20 mM HEPES, pH 7.4, containing 150 mM NaCl) at 37 °C for 30 min.

4.4.2.3 Fluorescence spectroscopy

Fluorescence spectra were measured after the probe (5.0 μM) was incubated with or without PYP-tag (10 μM) in the assay buffer at 37 °C for 30 min. The fluorescence spectra of the mixtures were recorded at an excitation wavelength of 535 nm (**HTL-RB** and **HTL-RBis**), with a slit width of 5.0 nm for both excitation and emission. Relative fluorescence quantum yields were determined using Rhodamine B in water (Ex: 535 nm, Φ_{fl} = 36%)[41] as a reference.

4.4.2.4 Cell culture

HEK293T cells were purchased from RIKEN BRC. HEK293T cells were cultured in DMEM containing 10% fetal bovine serum and PS as antibiotics (100 U/mL penicillin and 0.1 mg/mL streptomycin). Transfected cells were maintained in a 5% CO_2 atmosphere at 37 °C throughout the experiments.

4.4.2.5 Fluorescence imaging of proteins in living cells using HTL-RB and HTL-RBis

HEK293T cells were transfected with pcDNA3.1(+)-PYP^{NQN}-NLS using Lipofectamine 3000 (Invitrogen), according to the manufacturer's protocol. After incubation of the transfected cells in 5% CO_2 at 37 °C for 24 h, the cells were washed with HBSS buffer three times. Then, the cells were incubated with 2.5 μM probe in DMEM for 60 min. After replacing the medium with DMEM, the cells were incubated for an additional 30 min and then rinsed 3 × 5 min in DMEM before image acquisition. All images were captured at an excitation frequency of 561 nm with an emission range of 566–685 nm using a 63× lens (Zeiss LSM 880).

4.5 Reference

1. Los, G. V.; Encell, L. P.; McDougall, M. G.; Hartzell, D. D.; Karassina, N.; Zimprich, C.; Wood, M. G.; Learish, R.; Ohana, R. F.; Urh, M.; Simpson, D.; Mendez, J.; Zimmerman, K.; Otto, P.; Vidugiris, G.; Zhu, J.; Darzins, A.; Klaubert, D. H.; Bulleit, R. F.; Wood, K. V. HaloTag: A Novel Protein Labeling Technology for Cell Imaging and Protein Analysis. *ACS Chem. Biol.* **2008**, *3* (6), 373–382.
2. Berki, T.; Bakunts, A.; Duret, D.; Fabre, L.; Ladavière, C.; Orsi, A.; Charreyre, M.-T.; Raimondi, A.; van Anken, E.; Favier, A. Advanced Fluorescent Polymer Probes for the Site-Specific Labeling of Proteins in Live Cells Using the HaloTag Technology. *ACS Omega* **2019**, *4* (7), 12841–12847.
3. Kompa, J.; Bruins, J.; Glogger, M.; Wilhelm, J.; Frei, M. S.; Tarnawski, M.; D'Este, E.; Heilemann, M.; Hiblot, J.; Johnsson, K. Exchangeable HaloTag Ligands for Super-Resolution Fluorescence Microscopy. *J. Am. Chem. Soc.* **2023**, *145* (5), 3075–3083.
4. Jiang, X.; Chen, J.; Wang, M. C.; Wang, J. Glutathione Quantification in Live Cells with Real-Time Imaging and Flow Cytometry. *STAR Protocols* **2020**, *1* (3), 100170.
5. Cook, A.; Walterspiel, F.; Deo, C. HaloTag-Based Reporters for Fluorescence Imaging and Biosensing. *ChemBioChem* **2023**, *24* (12), e202300022.
6. Wilhelm, J.; Kühn, S.; Tarnawski, M.; Gotthard, G.; Tünnermann, J.; Tänzer, T.; Karpenko, J.; Mertes, N.; Xue, L.; Uhrig, U.; Reinstein, J.; Hiblot, J.; Johnsson, K. Kinetic and Structural Characterization of the Self-Labeling Protein Tags HaloTag7, SNAP-Tag, and CLIP-Tag. *Biochemistry* **2021**, *60* (33), 2560–2575.
7. Kumar, P.; Vevea, J. D.; Chapman, E. R.; Lavis, L. D. Multifunctional Fluorophores for Live-Cell Imaging and Affinity Capture of Proteins. bioRxiv **2022**, preprint. DOI: https://doi.org/10.1101/2022.07.02.498544
8. Deo, C.; Abdelfattah, A. S.; Bhargava, H. K.; Berro, A. J.; Falco, N.; Farrants, H.; Moeyaert, B.; Chupanova, M.; Lavis, L. D.; Schreiter, E. R. The HaloTag as a General Scaffold for Far-Red Tunable Chemigenetic Indicators. *Nat. Chem. Biol.* **2021**, *17* (6), 718–723.
9. Wilhelm, J.; Kühn, S.; Tarnawski, M.; Gotthard, G.; Tünnermann, J.; Tänzer, T.; Karpenko, J.; Mertes, N.; Xue, L.; Uhrig, U.; Reinstein, J.; Hiblot, J.; Johnsson, K. Kinetic and Structural Characterization of the Self-Labeling Protein Tags HaloTag7, SNAP-Tag, and CLIP-Tag. *Biochemistry* **2021**, *60* (33), 2560–2575.
10. Kii, I.; Shiraishi, A.; Hiramatsu, T.; Matsushita, T.; Uekusa, H.; Yoshida, S.; Yamamoto, M.; Kudo, A.; Hagiwara, M.; Hosoya, T. Strain-Promoted Double-Click

Reaction for Chemical Modification of Azido-Biomolecules. *Org. Biomol. Chem.* **2010**, *8* (18), 4051–4055.

11. Zhang, Y.; So, M.; Loening, A. M.; Yao, H.; Gambhir, S. S.; Rao, J. HaloTag Protein-Mediated Site-Specific Conjugation of Bioluminescent Proteins to Quantum Dots. *Angew. Chem. Int. Ed.* **2006**, *45* (30), 4936–4940.
12. Kamikawa, T.; Hashimoto, A.; Yamazaki, N.; Adachi, J.; Matsushima, A.; Kikuchi, K.; Hori, Y. Bioisostere-Conjugated Fluorescent Probes for Live-Cell Protein Imaging without Non-Specific Organelle Accumulation. *Chem. Sci.* **2024**, *15* (21), 8097–8105.
13. Yoo, D. Y.; Barros, S. A.; Brown, G. C.; Rabot, C.; Bar-Sagi, D.; Arora, P. S. Macropinocytosis as a Key Determinant of Peptidomimetic Uptake in Cancer Cells. *J. Am. Chem. Soc.* **2020**, *142* (34), 14461–14471.
14. Gustafson, J. L.; Neklesa, T. K.; Cox, C. S.; Roth, A. G.; Buckley, D. L.; Tae, H. S.; Sundberg, T. B.; Stagg, D. B.; Hines, J.; McDonnell, D. P.; Norris, J. D.; Crews, C. M. Small-Molecule-Mediated Degradation of the Androgen Receptor through Hydrophobic Tagging. *Angew. Chem. Int. Ed.* **2015**, *54* (33), 9659–9662.
15. Reja, S. I.; Hori, Y.; Kamikawa, T.; Yamasaki, K.; Nishiura, M.; Bull, S. D.; Kikuchi, K. An "OFF–ON–OFF" Fluorescence Protein-Labeling Probe for Real-Time Visualization of the Degradation of Short-Lived Proteins in Cellular Systems. *Chem. Sci.* **2022**, *13* (5), 1419–1427.

Chapter 5. Conclusion and perspectives

5.1 Conclusion and perspectives

In this thesis, the author demonstrated that tetrazole-conjugated protein-labeling probes containing the cationic dye scaffolds rhodamine B and styryl pyridinium derivatives can be applied for live-cell intracellular protein imaging without undesired mitochondrial accumulation.

In Chapter 1, the general background of this thesis was explained, namely the background of fluorescence protein imaging, limitation of cationic probes in live-cell protein imaging, and outline of this research were described.

In Chapter 2, the development of tetrazole-conjugated PYP-tag labeling probes was achieved for intracellular protein imaging in live cells. As a result of fluorescence analyses, RB-based probes in both free and bound states were confirmed to show fluorescence under physiological conditions. In addition, SP-based probes show significant fluorogenicity upon binding to PYP-tag protein. Live-cell intracellular protein imaging experiments were conducted to investigate the intracellular distribution and membrane permeability of RB-based probes (**PCAF-RBis** and **PCAF-RB**). **PCAF-RBis** successfully visualized intracellular proteins without non-specific signals, whereas **PCAF-RB** showed non-specific mitochondrial accumulation. Then, localization analysis with MitoTracker Green FM confirmed **PCAF-RB** mitochondrial accumulation. These results demonstrated that the introduction of tetrazole into probes suppresses undesirable accumulation. Although **PCAF-SP** and **PCAF-SP-s** have serious problems in intracellular protein imaging, respectively, novel SP-based probe **PCAF-SPis**, which is developed by the author, can be applied for non-wash intracellular protein imaging in live cells.

In Chapter 3, the visualization of GLUT4 multiple localizations as a live-cell protein imaging application of **PCAF-RBis** and **PCAF-SP-s** was described. **PCAF-RBis** was employed for the visualization of intracellular GLUT4. As a result of intracellular GLUT4 imaging, fluorescent signals were observed in the cytoplasmic region of live cells expressing PYP-GLUT4, indicating that **PCAF-RBis** could label intracellular GLUT4. As a result of control experiments, fluorescence signals were not observed, indicating **PCAF-RBis** could label intracellular GLUT4 without undesired signals. Furthermore, dual-color imaging using both **PCAF-RBis** labeling and immunostaining in HeLa cells expressing PYP-GLUT4 was conducted, resulting in overlapping signals derived from **PCAF-RBis** and immunostaining. These results demonstrated that **PCAF-RBis** can

specifically label intracellular GLUT4 without off-target labeling. Membrane-localized GLUT4 can be specifically imaged by live-cell imaging using **PCAF-SP-s**. Then, **PCAF-RBis** and **PCAF-SP-s** were applied to visualize multiple localizations of GLUT4.

In Chapter 4, HaloTag labeling probes (**HTL-RBis** and **HTL-RB**) were successfully developed. **HTL-RBis** effectively visualized intracellular proteins and significantly reduced non-specific accumulation.

In summary, the author demonstrated that a novel strategy could provide membrane-permeable probes through concise conjugation steps using tetrazole-bearing amino acid derivatives and cationic fluorescent scaffolds.[1] The author hopes that the probe design approach of tetrazole-conjugated probes can not only be applied to the development of protein labeling probes but also to various functional molecules with cationic scaffolds in cellular applications.

Cationic functional molecules such as synthetic probes,[2-10] pharmaceutical molecules,[11,12] and catalysts were already reported to work as desired functional molecules in mitochondria of live cells. In synthetic fluorescent probes,[2-7] Aggregation-induced emission (AIE) probes,[8,9] Raman probes,[10] as described in Chapter 2, and synthetic probes based on cationic dyes (rhodamine, cyanine, pyridinium, and pyrylium derivatives), which exhibit excellent optical properties, have been developed for the visualization of various biomolecules in mitochondria of live cells. In the case of pharmaceutical molecules, the photosensitizers[11] based on cyanine dyes for photodynamic therapy and mitochondrial G-quadruplex structures targeting molecules[12] for human colorectal cancer therapy have been reported. Among the cationic catalysts, ruthenium catalysts can be applied for the alloc deprotection in mitochondria of live cells.[13] Iridium photocatalysts for proteomics studies enable the biorthogonal proximity labeling of mitochondria-localized proteins owing to the mitochondrial-accumulating properties of photocatalysts.[14] In addition, cationic dye-based catalysts have been employed for profiling protein–protein interactions by intracellular photocatalytic proximity labeling.[15,16] These cationic molecules exhibit mitochondrial-accumulating properties, making them suitable for mitochondrial applications, while their expansion to non-mitochondrial targets in the cell is challenging.

Based on this background, a novel design strategy opens up new possibilities for the development of zwitterionic membrane-permeable molecules, namely novel probes with bioisosteres and cationic molecules, which could be provided by the conjugation of arbitrary pairs. The author believes that our strategy will find widespread application in the design of various functional molecules using cationic scaffolds.

5.2 Reference

1. Kamikawa, T.; Hashimoto, A.; Yamazaki, N.; Adachi, J.; Matsushima, A.; Kikuchi, K.; Hori, Y. Bioisostere-Conjugated Fluorescent Probes for Live-Cell Protein Imaging without Non-Specific Organelle Accumulation. *Chem. Sci.* **2024**, *15* (21), 8097–8105.
2. Koide, Y.; Urano, Y.; Hanaoka, K.; Terai, T.; Nagano, T. Evolution of Group 14 Rhodamines as Platforms for Near-Infrared Fluorescence Probes Utilizing Photoinduced Electron Transfer. *ACS Chem. Biol.* **2011**, *6* (6), 600–608.
3. Resta, I. M.; Lucantoni, F.; Apostolova, N.; Galindo, F. Fluorescent Styrylpyrylium Probes for the Imaging of Mitochondria in Live Cells. *Org. Biomol. Chem.* **2021**, *19* (41), 9043–9057.
4. Guo, D.; Sun, J.; Tian, M.; Lin, W. Fabrication of a Fluorescent Probe for Reversibly Monitoring Mitochondrial Membrane Potential in Living Cells. *Anal. Methods* **2021**, *13* (14), 1715–1719.
5. Takakura, H.; Zhang, Y.; Erdmann, R. S.; Thompson, A. D.; Lin, Y.; McNellis, B.; Rivera-Molina, F.; Uno, S.; Kamiya, M.; Urano, Y.; Rothman, J. E.; Bewersdorf, J.; Schepartz, A.; Toomre, D. Long Time-Lapse Nanoscopy with Spontaneously Blinking Membrane Probes. *Nat. Biotechnol* **2017**, *35* (8), 773–780.
6. Zheng, S.; Dadina, N.; Mozumdar, D.; Lesiak, L.; Martinez, K. N.; Miller, E. W.; Schepartz, A. Long-Term Super-Resolution Inner Mitochondrial Membrane Imaging with a Lipid Probe. *Nat. Chem. Biol.* **2024**, *20* (1), 83–92.
7. Grzelakowska, A.; Modrzejewska, J.; Kolińska, J.; Szala, M.; Zielonka, M.; Dębowska, K.; Zakłos-Szyda, M.; Sikora, A.; Zielonka, J.; Podsiadły, R. Water-Soluble Cationic Boronate Probe Based on Coumarin Imidazolium Scaffold: Synthesis, Characterization, and Application to Cellular Peroxynitrite Detection. *Free Radic. Biol. Med.* **2022**, *179*, 34–46.
8. Chen, Y.; Xu, Q.; Zhao, W.; Wang, C. A Mitochondria-Targeting "off–on" AIE Probe with Large Stokes Shift for High-Contrast H2S Imaging in Living Cells. *New J. Chem.* **2023**, *47* (28), 13456–13461.
9. Zhao, N.; Chen, S.; Hong, Y.; Tang, B. Z. A Red Emitting Mitochondria-Targeted AIE Probe as an Indicator for Membrane Potential and Mouse Sperm Activity. *Chem. Commun.* **2015**, *51* (71), 13599–13602.
10. Fujioka, H.; Shou, J.; Kojima, R.; Urano, Y.; Ozeki, Y.; Kamiya, M. Multicolor Activatable Raman Probes for Simultaneous Detection of Plural Enzyme Activities. *J. Am. Chem. Soc.* **2020**, *142* (49), 20701–20707.

11. Broadwater, D.; Bates, M.; Jayaram, M.; Young, M.; He, J.; Raithel, A. L.; Hamann, T. W.; Zhang, W.; Borhan, B.; Lunt, R. R.; Lunt, S. Y. Modulating Cellular Cytotoxicity and Phototoxicity of Fluorescent Organic Salts through Counterion Pairing. *Sci. Rep.* **2019**, *9* (1), 15288.
12. Zheng, B.-X.; Long, W.; Zheng, W.; Zeng, Y.; Guo, X.-C.; Chan, K.-H.; She, M.-T.; Leung, A. S.-L.; Lu, Y.-J.; Wong, W.-L. Mitochondria-Selective Dicationic Small-Molecule Ligand Targeting G-Quadruplex Structures for Human Colorectal Cancer Therapy. *J. Med. Chem.* **2024**, *67* (8), 6292–6312.
13. Tomás-Gamasa, M.; Martínez-Calvo, M.; Couceiro, J. R.; Mascareñas, J. L. Transition Metal Catalysis in the Mitochondria of Living Cells. *Nat. Commun.* **2016**, *7* (1), 12538.
14. Liu, Z.; Guo, F.; Zhu, Y.; Qin, S.; Hou, Y.; Guo, H.; Lin, F.; Chen, P. R.; Fan, X. Bioorthogonal Photocatalytic Proximity Labeling in Primary Living Samples. *Nat. Commun.* **2024**, *15* (1), 2712.
15. Tsushima, M.; Sato, S.; Miura, K.; Niwa, T.; Taguchi, H.; Nakamura, H. Intracellular Photocatalytic-Proximity Labeling for Profiling Protein–Protein Interactions in Microenvironments. *Chem. Commun.* **2022**, *58* (12), 1926–1929.
16. Nakane, K.; Nagasawa, H.; Fujimura, C.; Koyanagi, E.; Tomoshige, S.; Ishikawa, M.; Sato, S. Switching of Photocatalytic Tyrosine/Histidine Labeling and Application to Photocatalytic Proximity Labeling. *Int. J. Mol. Sci.* **2022**, *23* (19), 11622.

List of Publication

Original Paper

1. **Takuya Kamikawa**, Akari Hashimoto, Nozomi Yamazaki, Junya Adachi, Kazuya Kikuchi, Yuichiro Hori. “Bioisostere-Conjugated Fluorescent Probes for Live-Cell Protein Imaging without Non-Specific Organelle Accumulation." *Chem. Sci.* **2024**, *15* (21), 8097–8105.

Related Papers

1. Shahi Imam Reja, Yuichiro Hori, **Takuya Kamikawa**, Kohei Yamasaki, Miyako Nishiura, Steven D. Bull, Kikuchi Kazuya. “An “OFF-ON-OFF” fluorescence protein-labeling probe for real-time visualization of the degradation of short-lived proteins in cellular systems.” *Chem. Sci.* **2022**, *13* (5), 1419–1427. (Selected in 2022 most popular analytical chemistry articles collection of Chemical Science)
2. **上川　拓也**，堀　雄一郎 「タンパク質標識技術によるイメージング法の進展」 高分子，**2023**, *72*, 379-381.

Acknowledgements

This doctoral thesis is the summary of the author's studies conducted under the super vision of Professor Yuichiro Hori at the Department of Chemistry, Graduate School of Science, Kyushu University.

The author would like to be most grateful to Professor Yuichiro Hori for his continuous guidance, support, and encouragement throughout this study. He provides me the precious research opportunity, considerable advices and sophisticated knowledges.

The author expresses his sincere thanks to Professor Kazuya Kikuchi at Osaka University for his valuable guidance and discussion.

The author would like to show his gratitude to all of Hori laboratory staffs, Associate professor Kanae Yumimoto, Assistant professor Junya Adachi and many friendly students for kind help and useful suggestion.

The author also expresses his cordial thanks to all of Kikuchi laboratory staffs, Associate professor Masafumi Minoshima, Dr. Shahi Imam Reja, Ms. Miyako Nishiura and many friendly students, for kind instruction and helpful discussion.

The author is grateful to Professor Tohru Oishi and Assistant professor Yoko Yasuno for their support on the measurement of ESI-MS.

The author appreciates Associate professor Ayami Matsushima for her support on the use of lyophilizer.

The author would like to thank Professor Hiroyuki Kagechika at Tokyo Medical and Dental University for his kind advices and helpful suggestions.

The author acknowledges financial support from the establishment of university fellowships towards the creation of science technology innovation (Grant Number: JPMJFS2132).

Finally, the author appreciates the continuous support and encouragement from his family.

Takuya Kamikawa

June 2024